Nonlinear optics in monolithic cavities close to the absorption band

Genehmigte Dissertation

zur Erlangung des Doktorgrades

an der Fakultät für Mathematik, Informatik und Naturwissenschaften
Fachbereich Physik
Universität Hamburg

vorgelegt von

Torben Sobottke

Hamburg
2025

Gutachter der Dissertation:	Prof. Dr. Roman Schnabel Dr. Mikhail Korobko
Zusammensetzung der Prüfungskommission:	Prof. Dr. Roman Schnabel Dr. Mikhail Korobko Prof. Dr. Daniela Pfannkuche Dr. Christoph Becker Prof. Dr. Peter Schauss (als Ersatz für Prof. Dr. Arwen Pearson)
Vorsitzende der Prüfungskommission:	Prof. Dr. Daniela Pfannkuche
Datum der Disputation:	3. Dezember 2025
Vorsitzender des Fach-Promotionsausschusses:	Prof. Dr. Johannes Haller
Leitung des Fachbereichs Physik:	Prof. Dr. Markus Drescher
Dekan der Fakultät MIN:	Prof. Dr.-Ing. Norbert Ritter

Kurzfassung

In einer Vielzahl wissenschaftlicher Experimente werden bereits gequetschte Lichtzustände eingesetzt, um das Signal-Rausch-Verhältnis zu erhöhen – von Spektroskopie über biologische Messungen bis zur flächendeckenden Anwendung in Gravitationswellendetektoren. Aufgrund ihrer quantenkorrelierten Natur sind gequetschte Lichtzustände außerdem ein wertvolles Konzept für Quanteninformationsprotokolle und ein vielversprechender Kandidat für optische Quantencomputer. In diesem Zusammenhang ist die Wechselwirkung zwischen gequetschten Lichtzuständen und Atomen von besonderem Interesse.

In dieser Arbeit wird eine Quetschlichtquelle für 800 nm – also in der Nähe der Rb D_1-Linie (795 nm) – vorgestellt und charakterisiert. Der Aufbau besteht aus zwei monolithischen optischen Resonatoren, deren Endspiegel direkt auf periodisch gepolte $KTiOPO_4$-Kristalle (PPKTP) gedampft wurden. Im ersten Resonator wird die Frequenz verdoppelt (SHG nach 400 nm), während im zweiten die gequetschten Lichtzustände mittels parametrischer Abkonversion (PDC) erzeugt werden. Die SHG erreichte eine Konversionseffizienz von bis zu 58.6 % bei einer Eingangsleistung von 120 mW. Mit dem Quetschlichtresonator wurde ein maximaler Quetschwert von 4.02 dB unterhalb des Vakuumrauschens bei einem Antiquetschpegel von etwa 23 dB erreicht. Die optischen Verluste von insgesamt etwa 35 % waren vor allem durch die Absorption des 800 nm-Lichts im Resonator selbst bedingt, welche durch die Bestrahlung mit dem 400 nm-Pumplicht signifikant zunahm.

Der monolithische Aufbau ist hochstabil und robust gegen mechanische Schwingungen; er bringt jedoch in diesem Experiment zwei Herausforderungen mit sich. Erstens werden sowohl die Resonanzfrequenz des Resonators als auch die Phasenanpassung für den parametrischen Prozess über die Kristalltemperatur eingestellt und können daher nicht unabhängig voneinander geregelt werden. Zweitens wird das erzeugte 400 nm-Licht am Rand des Transparenzbereichs von PPKTP teilweise absorbiert, was den Kristall erwärmt. Bei Eingangsleistungen über 10 mW führen diese gekoppelten Freiheitsgrade zu einem nichtlinearem Antwortverhalten des Systems, welches umfassend charakterisiert wurde. Mit einer neu entwickelten Methode konnten das SHG-Verstärkungsprofil und seine Verschiebung im Frequenzraum vermessen werden, obwohl diese Informationen im monolithischen Design nicht direkt zugänglich sind.

Durch eine Langzeitmessung an der SHG über 67 h mit einer Eingangsleistung von 170 mW nahm ihre Konversionseffizienz von 32 % auf 13 % ab. Nach dieser Exposition war im Kristall eine Trübung entlang des Strahlwegs deutlich sichtbar. Durch Ausheizen des Kristalls auf 135 °C für 97 h ging die Beschädigung des Kristalls zwar zurück; dies reichte jedoch nicht für eine vollständige Heilung. Zusammenfassend scheint das monolithische Design nicht für Anwendungen in Quantenoptik-Experimenten geeignet, sofern diese einen stabilen Langzeitbetrieb und eine durch das Experiment definierte Laserfrequenz erfordern. Alternative Ansätze werden diskutiert.

Abstract

To date, squeezed states of light are already applied in a broad range of scientific experiments to increase the signal-to-noise ratio – from spectroscopy, magnetometry and biological measurements to large-scale gravitational-wave detection. Due to the quantum-correlated nature of squeezed states of light, they are also a powerful resource in quantum information and a promising candidate for optical quantum computing. In view of this, the interaction between squeezed states of light and atoms has become of particular interest.

This thesis presents and characterizes a squeezed light source operating at 800 nm, in proximity to the Rb D_1 line (795 nm). The setup consists of two monolithic optical cavities, whose end mirrors are directly coated onto a periodically-poled $KTiOPO_4$ (PPKTP) crystal: one acting as second harmonic generation (SHG) for frequency doubling to 400 nm and the other for parametric down-conversion (PDC), generating the squeezed states of light. The SHG yielded a conversion efficiency of up to 58.6 % at 120 mW input power. With the squeezing cavity, a maximum squeezing level of 4.02 dB below the vacuum level was achieved at an antisqueezing level of around 23 dB. The overall optical losses of around 35 % were dominated by the intracavity losses inside the squeezing cavity at 800 nm, which increased significantly due to illumination with the 400 nm pump light.

While bringing the advantage of being highly stable and robust against mechanical oscillations, the monolithic design imposes two main challenges in this experiment: First, the cavity's resonance frequency and the phase matching for the parametric gain are both tuned via the crystal temperature and therefore cannot be accessed independently. Second, the generated 400 nm light is on the edge of the transparency window of PPKTP and is thus subject to absorption that heats the crystal. At input powers above 10 mW, the coupled degrees of freedom lead to nonlinear responses of the system, which were thoroughly characterized. A method was developed to probe the SHG gain profile and its shift in frequency space, even though this information cannot be accessed directly in the monolithic design.

To quantify the longterm performance of the system, a high-power measurement with 170 mW input power was performed on the SHG over 67 h, which decreased the conversion efficiency from 32 % to 13 %. Gray tracking of the beam path was clearly visible after this prolonged exposure. Heating the crystal to 135 °C for 97 h reduced the crystal's damage; however, it did not heal the crystal sufficiently for reuse. In conclusion, the monolithic design does not seem suitable for application in quantum optics experiments that require stable, longterm operation at a laser frequency that is defined by the experiment. Alternative approaches are discussed.

Contents

1. Introduction

For centuries, scientists have been fascinated by the nature of light, and with each step towards a better understanding of its properties, new tools and techniques have been developed – tools that, in turn, have opened up completely new ways to explore, understand, and control the universe. While in early years only broadband thermal light sources were available, the invention of spectral lamps with narrow linewidths of a few MHz to GHz allowed a completely new class of experiments using the coherence properties of light. Spectroscopic measurements allowed to determine the composition of materials and the spectra of atomic gases, laying the foundation for Bohr's atomic model and paving the way for the age of quantum physics. The profound understanding of quantum mechanical processes led to Einstein's theoretical prediction of light amplification by stimulated emission of radiation (laser) [Ein17], which was first realized experimentally by Maiman in 1960 [Mai60]. In the following years, this novel light source found application in a variety of different settings, ranging from LIDAR and novel manufacturing methods to optical communication and biomedical applications – techniques that were completely unimaginable before the advent of the laser. But also for scientific purposes, the laser turned out to be perhaps the most valuable tool of the 20th century: with its narrow bandwidth on the order of atomic linewidths and kilometer-scale coherence lengths, it enabled the enhancement of spectroscopic and interferometric measurements, as well as the selective addressing of specific atomic transitions, and thereby the manipulation of the interaction between light field and matter in a previously unprecedented way. The field of quantum optics emerged, studying the quantum properties of light and the interaction between light and matter at the single photon and single atom level.

Soon after the first experimental realization of the laser, Glauber found a fully quantum mechanical description of the light field that described the then-available laser light as coherent states [Gla63], characterized by a symmetric uncertainty of the electric field in both quadratures of the field. This concept was generalized to minimum uncertainty states with unequal uncertainty in both quadratures by Stoler [Sto70; Sto71] and Lu [Lu71; Lu72], who suggested that these two-photon states could be generated by parametric amplification. Further important properties of these two-photon coherent states were derived in a systematic study by Yuen in 1976 [Yue76]. Only five years later, Caves found that the reduced quantum noise of these "squeezed states" of light could be used to enhance the sensitivity of interferometric gravitational wave detectors beyond the quantum noise limit of the light field [Cav81]. From then, it took only another five years until the first squeezed states of light were realized experimentally. In 1985, Slusher *et al.* measured the first squeezing generated via four-wave mixing in sodium atoms [Slu+85]. One year later, Wu *et al.* inferred a 50 % reduction of the noise level relative to the vacuum noise through parametric down-conversion in an optical parametric oscillator (OPO) operated below threshold [Wu+86]. Up until today, the highest squeezing levels of up to 15 dB at 1064 nm have been realized and detected with similar, yet improved techniques [Vah+16]. Currently, the Advanced LIGO detectors [Aas+13; Tse+19] and GEO 600 [The+11; Gro+13] benefit from a sensitivity-enhancement through the injection of squeezed states of light during their observation runs; for Advanced LIGO, a squeezing level of 2.7 dB increases the event detection rate by around 50 % [Tse+19]. But also other shot noise limited measurements have been improved through by the use of squeezed light – from squeezing-enhanced spectroscopy [PCK92b; PCK92c; And+20; Li+22; Xu+22a], magnetometry [Wol+10; Li+18], or rotational sensing [Liu+18] to different squeezing-enhanced microscopy techniques, where nonclassical light allows to optimize the signal-to-noise ratio for a given threshold laser power to avoid damaging of biological samples [Tay+13; Tri+20; Cas+21; Xu+22b].

As for the laser, apart from the improvement of existing measurement techniques, even more interesting questions arise: Are there fundamental differences in the interaction between squeezed states of light and matter (compared to the interaction with laser light)? What fundamentally new techniques and methods can arise from the availability of squeezed states of light that explicitly require nonclassical states of light? One promising answer to these questions is continuous-variable optical quantum computing, where modified squeezed states of light (so-called GKP states [GKP01]) may be used as flying qubits, and their interaction and entanglement can be realized by overlapping two qubits on different ports of a beam splitter. To ensure that the involved qubits arrive at the beam splitter at well-defined times, some form of quantum storage is required. For squeezed states of light, a promising scheme has been proposed by Fleischhauer and Lukin [FL02; LYF00; FL00] and Dantan and Pinard [DP04], in which the quantum state of the light field can be stored by imprinting it onto an atomic ensemble using electromagnetically induced transparency (EIT): When the EIT is switched off while the qubit propagates through the ensemble and this light is resonant with the atomic transition, its quantum state can be transferred to the atomic ensemble (and retrieved from there once the EIT is established again). To realize protocols that use this technique, squeezed light sources operating at the resonance frequency of broad atomic transitions that can be switched by EIT are required.

An inviting wavelength for this purpose is the rubidium D_1 line at 795 nm, since Rb, as an alkaline metal, has a relatively simple level structure for which the required EIT can be realized. Rb is used in many quantum gas experiments across the globe, including at the Institute for Quantum Physics in Hamburg. Here, the interaction of squeezed light with atoms could perspectively be studied in a cavity QED experiment, where an atomic ensemble is placed inside a high-finesse optical resonator [Kli+16]. Most interestingly, this experiment uses a far-detuned pump beam at 803 nm resonant to a high-finesse cavity, such that photons can be scattered off the Rb atoms into the cavity mode. It seems worth studying how the injection of squeezed states of light along different axes of the experiment modifies the interaction between light and atoms. To realize this experimentally, a squeezed light source would be desirable, with a frequency that can be easily tuned in the wavelength range around 795 – 803 nm.

1.1. Squeezed light experiments around 800 nm

Quite a number of squeezing experiments have already been performed in this wavelength range, most of them focusing on the resonance with the Rb D_1 line and operating at 795 nm. It was first shown by Akamatsu *et al.* that resonant squeezing is maintained when traversing a Rb vapor cell in which absorption is avoided due to EIT – here, 0.9 dB of continuous-wave (cw) squeezing was generated in a MgO:LiNbO$_3$ waveguide, which reduced to 0.18 dB after passage through the EIT medium [AAK04]. Squeezing at 795 nm has also been reported by the groups of Furusawa (yielding 2.75 dB of squeezing) [Tan+06a], Lvovsky (up to 3 dB) [App+07], and Bachor and Lam, where up to 5.2 dB of squeezing was produced [Hét+07]. All three groups used similar approaches with bow-tie cavity designs and periodically poled KTiPO$_4$ (PPKTP) as a nonlinear medium, although with different cavity parameters. In subsequent studies, these squeezed light sources were used to successfully demonstrate the proposal by Fleischhauer and Lukin, that squeezed states can be slowed down in a laser-cooled ^{87}Rb gas by decreasing the intensity of the EIT control beam [Aka+07], or stored and retrieved completely for up to 3 µs [Hon+08]. Similar results were reported by Appel *et al.* in a Rb vapor cell [App+08]. Hétet *et al.* demonstrated a delay of 2.2 µs and a maintained correlation between two beams of squeezed vacuum, one of which passed through an EIT Rb vapor cell with a buffer gas [Hèt+08]. In all of these experiments, the delay comes at the cost of significantly reduced squeezing levels after being delayed in the Rb gas.

More recently, active research on the generation and application of squeezed states of light at the Rb D_1 line has been conducted in the group of Wang. In 2016, Han *et al.* reported a squeezing level of 5.6 dB below the vacuum noise at 795 nm [Han+16], which was produced by a PPKTP crystal in a single-resonant bow-tie cavity. Intracavity losses at 795 nm were identified as the limiting factor for the performance. In the same experiment, subsequently, 2.8 dB of polarization squeezing was generated from an initial 5.6 dB vacuum squeezing [Wen+17]. After optimization of the sensitivity for audio-band frequencies [Bai+20], the setup was used to demonstrate squeezing-enhanced magnetometry [Bai+21] and squeezing-enhanced spin noise spectroscopy with 5.8 dB of squeezing at 7.3 dB of antisqueezing [Bai+22]. These are, to date, the highest squeezing levels reported at 795 nm.

To overcome the limitations caused by UV-induced optical losses at the squeezing wavelength, alternative approaches have been studied: In Rb vapor cells, polarization self-rotation was used – an effect that rotates the polarization if elliptically polarized light propagates through an optical medium. Although this is a particularly simple way of squeezing, squeezing levels of at most 1.1 dB were obtained [MN08; AMG10; Mik+09]. Kim and Marino returned to four-wave mixing to generate squeezing without the need for an absorptive nonlinear optical crystal [KM19]. In their experiment, two-mode squeezing was generated between entangled twin beams that were generated in the nonlinear process. The correlation in the quantum fluctuations in both beams could then be used to measure the amplitude fluctuations in one of them and, subsequently, apply a feed-forward on the other beam with an electro-optic modulator (EOM); in this way, a single-mode squeezed state is generated from the two-mode squeezed state. In their experiment, 2.9 dB of amplitude squeezing of a bright state was achieved when the beam was 1.9 GHz detuned from the Rb D_1 line; on resonance, this value decreased to 2.0 dB.

With possible scalable and potentially commercial applications in sight, interest also turns toward a small footprint and high stability of the system. For example, Torii *et al.* used PPLN waveguides to produce 1.5 dB of pulsed squeezing at 795 nm [Tor+22]. Zielińska and Mitchell used a design similar to that presented in this thesis, where the mirror surfaces for the second-harmonic generation (SHG) cavity [Zie+17; ZM17] and the optical parametric oscillator (OPO) [ZM18] are coated directly onto the end facets of two periodically poled Rb:KTiPO$_4$ crystals to increase mechanical stability and minimize intracavity losses. In this configuration, a maximum squeezing of 1.6 dB below vacuum noise was measured [ZM18]. Since the author became aware of this work only after completion of the experiments presented in this thesis, it was not possible to perform direct comparative measurements on the SHG or elaborate on the “very strong, previously unreported optical nonlinearity” that they claim to observe in their system [ZM17].

1.2. Aim and structure of this thesis

In this thesis, squeezed states of light in the wavelength region around 800 nm were realized and studied with respect to operability and achievable squeezing level. Two monolithic frequency-converting cavities were used: one for SHG to produce the 400 nm pump light, and an OPO in which the squeezed states of light were generated.

The thesis is structured in four parts. Chapter 2 gives an introduction to the theoretical description of squeezed states of light and the theoretical background for their detection. Chapter 3 presents the pump-light-generating monolithic SHG cavity in detail, characterizes its performance, and discusses thermal feedback effects that arise in a monolithic design. It also discusses degradation effects in the SHG crystal. Chapter 4 presents the monolithic OPO and the squeezing measurements in a setup with two monolithic cavities. Additionally, a thorough loss analysis is performed to identify the current experimental limitations in the achievable squeezing performance. Finally, Chapter 5 provides an outlook and suggests ways in which limitations of the current design could be overcome.

2. Theoretical background

This chapter introduces the theoretical concepts of squeezed states of light and their properties, mainly following the review by Loudon and Knight [LK87] and the textbook by Gerry and Knight [GK05]. Following the textbook by Boyd [Boy08], it further provides the theoretical background to understand optical processes and frequency conversion in nonlinear optical crystals, from which squeezed states can be generated. Finally, homodyne detection, the most common detection technique for squeezed states of light, is presented.

2.1. Hamiltonian of the quantized electromagnetic field

The quantization of the electromagnetic field is derived and discussed in every standard quantum optics textbook (e.g., [GK05], [WM08], [Lou00]) and shall therefore only be sketched here: Assuming a one-dimensional cavity oriented along the z-axis with perfectly conducting walls at $z = 0$ and $z = L$, Maxwell's equations are solved by standing waves, yielding the electric and magnetic field strengths

$$E_x(z,t) = \sqrt{\frac{2\omega^2}{\epsilon_0}}\, q(t) \sin(kz) \tag{2.1}$$

$$B_y(z,t) = \frac{\mu_0 \epsilon_0}{k} \sqrt{\frac{2\omega^2}{\epsilon_0}}\, \dot{q}(t) \cos(kz), \tag{2.2}$$

where ϵ_0 and μ_0 are the electric and magnetic constants, $\omega = c(m\pi/L)$ are the "allowed" angular frequencies for $m \in \mathbb{N}$ that satisfy the boundary condition of a vanishing electric field at $z = 0$ and $z = L$, and $k = \omega/c$ are the corresponding wave numbers. c is the speed of light. $q(t)$ is a time-dependent quantity having units of length, which will be considered as the canonical position, while $p(t) = \dot{q}(t)$ is the canonical momentum in this system. Integrating the squared electric and magnetic field strengths over the mode volume yields a Hamiltonian in the form of a harmonic oscillator, which can be quantized by replacing $q(t)$ and $p(t)$ with the operators $\hat{q}(t)$ and $\hat{p}(t)$ and requiring the commutation relation $[\hat{q}, \hat{p}] = i\hbar\hat{I}$, where $\hat{I}$ is the identity operator and $\hbar$ is the reduced Planck constant. The Hamiltonian of the quantized electromagnetic field then reads

$$\hat{\mathcal{H}} = \frac{1}{2}(\hat{p}^2 + \omega^2 \hat{q}^2). \tag{2.3}$$

One can define the annihilation and creation operators as

$$\hat{a}(t) = \frac{1}{\sqrt{2\hbar\omega}}(\omega\hat{q} + i\hat{p}) \tag{2.4}$$

$$\hat{a}^\dagger(t) = \frac{1}{\sqrt{2\hbar\omega}}(\omega\hat{q} - i\hat{p}) \tag{2.5}$$

Their time evolution can be written as

$$\hat{a}(t) = \hat{a}e^{-i\omega t} \tag{2.6}$$

$$\hat{a}^\dagger(t) = \hat{a}^\dagger e^{i\omega t}, \tag{2.7}$$

with time-independent $\hat{a} \equiv \hat{a}(0)$ and $\hat{a}^\dagger \equiv \hat{a}^\dagger(0)$. Using the fact that $\left[\hat{a}(t), \hat{a}^\dagger(t)\right] = 1$, eq. (2.3) can be written as

$$\hat{\mathcal{H}} = \hbar\omega\left(\hat{a}^\dagger\hat{a} + \frac{1}{2}\right). \tag{2.8}$$

Let $|n\rangle$ denote an eigenstate of eq. (2.8) with energy E_n. Then applying $\hat{a}^\dagger$ on both sides of the equation and using again $\left[\hat{a}, \hat{a}^\dagger\right] = 1$ yields the new eigenvalue equation

$$\hat{\mathcal{H}}(\hat{a}^\dagger|n\rangle) = (E_n + \hbar\omega)(\hat{a}^\dagger|n\rangle) \tag{2.9}$$

and similarly for $\hat{a}$

$$\hat{\mathcal{H}}(\hat{a}|n\rangle) = (E_n - \hbar\omega)(\hat{a}|n\rangle). \tag{2.10}$$

Thus, the operators $\hat{a}^\dagger$ and $\hat{a}$ can be understood to create or annihilate electromagnetic field quanta, the well-known photons, each carrying the energy $\hbar\omega$. Since the harmonic oscillator requires a lowest energy $E_0 \geq 0$, there must be a state $|0\rangle$ of this lowest energy without any additional excitations, for which $\hat{a}|0\rangle = 0$; this state is commonly referred to as the vacuum state. Its energy can be calculated from eq. (2.8) to be

$$E_0 = \langle 0|\hbar\omega\left(\hat{a}^\dagger\hat{a} + \frac{1}{2}\right)|0\rangle = \frac{\hbar\omega}{2}. \tag{2.11}$$

According to eq. (2.9), the n-th state $|n\rangle$ then has the energy

$$E_n = \langle n|\hbar\omega\left(\hat{a}^\dagger\hat{a} + \frac{1}{2}\right)|n\rangle = \hbar\omega\left(n + \frac{1}{2}\right), \tag{2.12}$$

which allows to identify $\hat{n} = \hat{a}^\dagger\hat{a}$ as the number operator, yielding the number of excitations in the state $|n\rangle$:

$$\hat{n}|n\rangle = n|n\rangle \tag{2.13}$$

With this, the Hamiltonian from eq. (2.8) can be written as

$$\hat{\mathcal{H}} = \hbar\omega(\hat{n} + \frac{1}{2}). \tag{2.14}$$

Fock states The states $|n\rangle$ are eigenvalues of the number operator with a well-defined number of excitations and are hence called number states or Fock states. The explicit action of $\hat{a}$ and $\hat{a}^\dagger$ on the number states $|n\rangle$ is given by

$$\begin{aligned} \hat{a}\,|n\rangle &= \sqrt{n}\,|n-1\rangle && (2.15)\\ \hat{a}^\dagger\,|n\rangle &= \sqrt{n+1}\,|n+1\rangle\,. && (2.16) \end{aligned}$$

Consequently, the number states can be generated from the vacuum state $|0\rangle$ by n-fold application of $\hat{a}^\dagger$:

$$|n\rangle = \frac{(\hat{a}^\dagger)^n}{\sqrt{n!}}\,|0\rangle\,, \tag{2.17}$$

where the prefactor $1/\sqrt{n!}$ was chosen such that the family of all number states $\{|n\rangle\}$ forms an orthonormal set.

Vacuum fluctuations From eq. (2.11), it becomes apparent that some energy must be present in the system even in the absence of any excitation of the electromagnetic field. As will be shown in the following, the reason for this are so-called vacuum fluctuations of the electromagnetic field.

Similarly to the Hamiltonian, the electric field operator can be written in terms of $\hat{a}$ and $\hat{a}^\dagger$:

$$\hat{E}_x(z,t) = \sqrt{\frac{\hbar\omega}{\epsilon_0 V}}(\hat{a}(t) + \hat{a}^\dagger(t))\sin(kz), \tag{2.18}$$

where V is the mode volume. While its expectation value vanishes for the state $|n\rangle$:

$$\left\langle \hat{E}_x(z,t) \right\rangle = \sqrt{\frac{\hbar\omega}{\epsilon_0 V}}\sin(kz)\,\langle n|(\hat{a}^\dagger(t) + \hat{a}(t))|n\rangle = 0, \tag{2.19}$$

its variance does not vanish:

$$\begin{aligned} \left\langle (\Delta\hat{E}_x(z,t))^2 \right\rangle &= \left\langle \hat{E}_x^2(z,t) \right\rangle - \underbrace{\left\langle \hat{E}_x(z,t) \right\rangle^2}_{0} \\ &= \frac{\hbar\omega}{\epsilon_0 V}\sin^2(kz)\,\langle n|(\hat{a}^{\dagger 2}(t) + \hat{a}^2(t) + 2\hat{a}^\dagger(t)\hat{a}(t) + 1)|n\rangle \\ &= 2\frac{\hbar\omega}{\epsilon_0 V}\sin^2(kz)\left(n + \frac{1}{2}\right). \end{aligned} \tag{2.20}$$

Hence, even in the absence of any excitations, the state $|0\rangle$ is subject to vacuum fluctuations of the electric field.

Quadrature operators The operators $\hat{a}$ and $\hat{a}^\dagger$ are not Hermitian, and therefore, do not correspond to observable quantities. However, one can define the Hermitian quadrature operators

$$\hat{X} = \frac{1}{2}(\hat{a} + \hat{a}^\dagger) \tag{2.21}$$

$$\hat{Y} = \frac{1}{2i}(\hat{a} - \hat{a}^\dagger) \tag{2.22}$$

that can be understood as the field amplitudes that oscillate with a phase delay of $\pi/2$ towards each other. With their definition, the electric can be written in the form

$$\hat{E}_x(t) = 2\mathcal{E}_0 \sin(kz) \left(\hat{X}\sin(\omega t) + \hat{Y}\cos(\omega t)\right) \tag{2.23}$$

where $\mathcal{E}_0 = \sqrt{\frac{\hbar\omega}{\epsilon_0 V}}$ is the electric field per excitation.

In terms of the quadrature operators, the Hamiltonian from eq. (2.8) reads

$$\hat{\mathcal{H}} = \hbar\omega(\hat{X}^2 + \hat{Y}^2). \tag{2.24}$$

From the commutator of $\hat{a}$ and $\hat{a}^\dagger$ follows that $\hat{X}$ and $\hat{Y}$ are also conjugate variables with $\left[\hat{X}, \hat{Y}\right] = \frac{i}{2}$, whose uncertainties are consequently subject to the Heisenberg relation

$$\left\langle(\Delta\hat{X})^2\right\rangle \cdot \left\langle(\Delta\hat{Y})^2\right\rangle \geq \frac{1}{16}. \tag{2.25}$$

2.2. Minimum uncertainty states

There are several states of the light field that satisfy the equality in eq. (2.25); these are called minimum uncertainty states. One well-known example is the vacuum state $|0\rangle$. Here, the uncertainties

$$\langle 0|(\Delta\hat{X})^2|0\rangle = \langle 0|\hat{X}^2|0\rangle - \langle 0|\hat{X}|0\rangle^2 = \langle 0|\left(\frac{1}{2}(\hat{a} + \hat{a}^\dagger)\right)^2|0\rangle = \frac{1}{4} \tag{2.26}$$

$$\langle 0|(\Delta\hat{Y})^2|0\rangle = \langle 0|\hat{Y}^2|0\rangle - \langle 0|\hat{Y}|0\rangle^2 = \langle 0|\left(\frac{1}{2i}(\hat{a} - \hat{a}^\dagger)\right)^2|0\rangle = \frac{1}{4} \tag{2.27}$$

are equally split in both quadratures. Another important class of minimum uncertainty states are coherent states [Gla63], also named Glauber states. They are eigenstates of the annihilation operator, satisfying

$$\hat{a}\,|\alpha\rangle = \alpha\,|\alpha\rangle\,, \tag{2.28}$$

which can be written in the Fock basis as

$$|\alpha\rangle = e^{-\frac{1}{2}|\alpha|^2} \sum_{n=0}^{\infty} \frac{\alpha^n}{\sqrt{n!}}\,|n\rangle\,. \tag{2.29}$$

Alternatively, by defining the unitary displacement operator

$$\hat{D}(\alpha) = e^{\alpha\hat{a}^\dagger - \alpha^*\hat{a}}, \tag{2.30}$$

coherent states can be generated by displacing the vacuum state:

$$|\alpha\rangle = \hat{D}(\alpha)\,|0\rangle = e^{\alpha\hat{a}^\dagger - \alpha^*\hat{a}}\,|0\rangle \tag{2.31}$$

The displacement leads to a non-zero amplitude and average photon number $\langle\alpha|\hat{n}|\alpha\rangle = |\alpha|^2$ while leaving the uncertainties $\langle\alpha|(\Delta\hat{X})^2|\alpha\rangle = \langle\alpha|(\Delta\hat{Y})^2|\alpha\rangle = \frac{1}{4}$ unchanged.

The left side of figure 2.1 shows a phase-space representation of a vacuum state and a coherent state. The displacement and angle in phase-space are given by the displacement parameter $\alpha = |\alpha|e^{i\phi}$. The circles mark the region of uncertainty for both cases. Mathematically, this quasi-probability distribution can be calculated by the Wigner function; for a more quantitative treatment, see, for example, [GK05]. In this phase-space picture, time evolution can be understood as a rotation of the phase-space axes (and the state therein). The electric field and its uncertainty are then given by the projection of the state onto a non-rotating axis. In both cases, the uncertainty in the electric field stays constant over time.

2.3. Quadrature-squeezed states of light

In general, the uncertainties in the quadrature operators $\hat{X}$ and $\hat{Y}$ do not have to be split equally as is the case for coherent states; the equality in eq. (2.25) can also be satisfied by an asymmetric splitting of the quadrature variances; the uncertainty circle is then squeezed into an ellipse. This class of minimum uncertainty states is therefore called (quadrature) squeezed states of light.

The quadrature operators $\hat{X}$ and $\hat{Y}$ introduced in eq. (2.21) and eq. (2.22) are special cases of a general quadrature operator $\hat{X}_\vartheta$ with arbitrary quadrature angle ϑ. It can be written as the linear combination

$$\hat{X}_\vartheta = \hat{X}\cos\vartheta + \hat{Y}\sin\vartheta, \tag{2.32}$$

such that $\hat{X} = \hat{X}_{\vartheta=0}$ and $\hat{Y} = \hat{X}_{\vartheta=\pi/2}$. From the commutator, it follows that eq. (2.25) holds for any two quadrature operators with orthogonal quadratures, that is

$$\left\langle(\Delta\hat{X}_\vartheta)^2\right\rangle \cdot \left\langle(\Delta\hat{X}_{\vartheta+\frac{\pi}{2}})^2\right\rangle \geq \frac{1}{16} \tag{2.33}$$

for arbitrary quadrature angle ϑ.

This thesis aims at producing squeezed states of light, whose fluctuations are for some quadrature angle ϑ smaller than the fluctuations of the vacuum state, i.e.,

$$\left\langle(\Delta\hat{X}_\vartheta)^2\right\rangle < \frac{1}{4}. \tag{2.34}$$

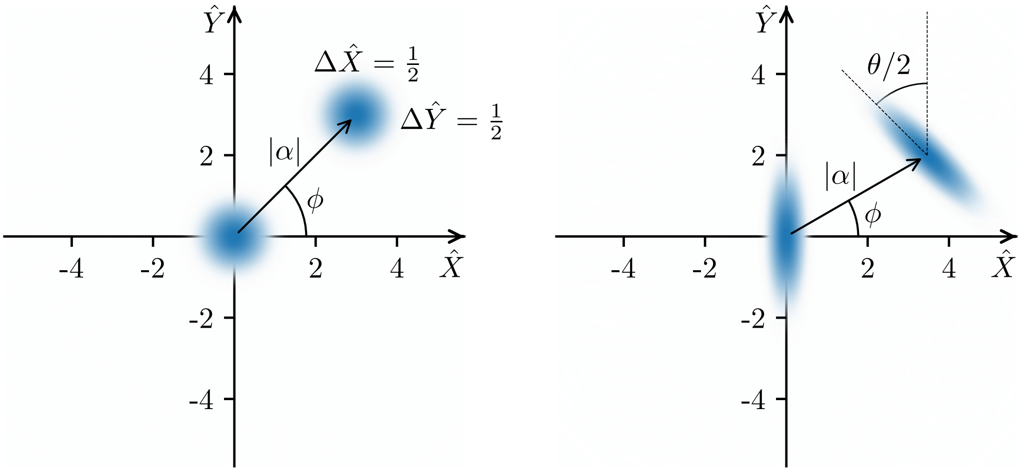

Figure 2.1.: Phase-space representation of coherent and squeezed states of light. Left: The coherent state $|\alpha\rangle$ is generated from the vacuum state $|0\rangle$ by applying $D(\alpha)$ (in this case with $|\alpha| = 3\sqrt{2}$ and $\phi = \frac{\pi}{4}$). Right: Squeezed vacuum state $\left|re^{i\theta}, 0\right\rangle$ with $r = 0.693$ and $\theta = 0$, corresponding to 6 dB squeezing; in this case $\Delta\hat{X} = \frac{1}{8}$ and $\Delta\hat{Y} = 2$. The depicted general displaced squeezed state $|\alpha, \xi\rangle$ has the parameters $|\alpha| = 4$, $\phi = \frac{\pi}{6}$, $r = 0.693$ and $\theta = \frac{\pi}{2}$.

This can be achieved in agreement with eq. (2.33) if the fluctuations in the orthogonal quadrature increase accordingly. In theory, this is performed by applying the squeeze operator $\hat{S}(\xi) = \exp\left(\frac{1}{2}\left(\xi^* \hat{a}^2 - \xi \hat{a}^{\dagger 2}\right)\right)$ to the vacuum state:

$$|\xi\rangle = \hat{S}(\xi)\,|0\rangle = e^{\frac{1}{2}\left(\xi^* \hat{a}^2 - \xi \hat{a}^{\dagger 2}\right)}\,|0\rangle \tag{2.35}$$

Here, $\xi = re^{i\theta}$, with the squeeze parameter $0 \leq r < \infty$ and the phase $0 \leq \theta \leq 2\pi$, which defines the angle $\theta/2$ in phase-space along which the uncertainty is reduced with respect to the $\hat{X}$ quadrature [GK05]. Successive application of $\hat{S}(\xi)$ and the displacement operator $\hat{D}(\alpha)$ from eq. (2.30) allows to create more general (bright) squeezed states [Cav81]

$$|\alpha, \xi\rangle = \hat{D}(\alpha)\hat{S}(\xi)\,|0\rangle\,, \tag{2.36}$$

from which the special cases of squeezed vacuum and non-squeezed coherent state can be obtained by setting $\alpha = 0$ or $\xi = 0$, respectively. The right side of figure 2.1 shows a squeezed vacuum state with $\theta = 0$, and a general displaced squeezed state.

Using the fact that for the general squeezed state $|\xi, \alpha\rangle$ [LK87]

$$\langle\hat{a}\rangle = \alpha, \tag{2.37}$$

$$\left\langle\hat{a}^\dagger\right\rangle = \alpha^*, \tag{2.38}$$

$$\left\langle\hat{a}^\dagger\hat{a}\right\rangle = |\alpha|^2 + \sinh^2 r, \tag{2.39}$$

$$\langle\hat{a}\hat{a}\rangle = \alpha^2 - e^{i\theta}\sinh r\cosh r, \tag{2.40}$$

one finds that the expectation values

$$\left\langle \hat{X} \right\rangle = \langle \alpha, \xi | \hat{X} | \alpha, \xi \rangle = \frac{1}{2}(\alpha + \alpha^*) = \mathrm{Re}(\alpha) \tag{2.41}$$

$$\left\langle \hat{Y} \right\rangle = \langle \alpha, \xi | \hat{Y} | \alpha, \xi \rangle = \frac{1}{2i}(\alpha - \alpha^*) = \mathrm{Im}(\alpha) \tag{2.42}$$

of a general squeezed state do not depend on the squeezing parameter r or its phase θ. Similarly, it can be found that the variances in both quadratures [LK87]

$$\left\langle (\Delta\hat{X})^2 \right\rangle = \frac{1}{4}\left(e^{-2r}\cos^2\frac{\theta}{2} + e^{2r}\sin^2\frac{\theta}{2}\right) \tag{2.43}$$

$$\left\langle (\Delta\hat{Y})^2 \right\rangle = \frac{1}{4}\left(e^{-2r}\sin^2\frac{\theta}{2} + e^{2r}\cos^2\frac{\theta}{2}\right) \tag{2.44}$$

are independent of α and, thus, are the same for squeezed coherent and squeezed vacuum states. $\theta = 0$ minimizes the fluctuation in one quadrature and maximizes the fluctuation in the corresponding orthogonal fluctuation:

$$\left\langle (\Delta\hat{X})^2 \right\rangle = \frac{1}{4}e^{-2r} \tag{2.45}$$

$$\left\langle (\Delta\hat{Y})^2 \right\rangle = \frac{1}{4}e^{2r} \tag{2.46}$$

More generally, for $\theta/2 \neq 0$, the extremal variances occur in the quadratures $\hat{X}_{\vartheta=\frac{\theta}{2}}$ and $\hat{X}_{\vartheta=\frac{\theta}{2}+\pi}$. The quadrature angle ϑ is a well-controllable experimental parameter (see sections 2.10 and 4.4). It can either be set to one specific value (e.g., to measure the fluctuations only in the squeezed / antisqueezed quadrature) or a smooth sweep can be applied to measure the variance $\left\langle (\Delta\hat{X}_\vartheta)^2 \right\rangle$ for varying quadrature angle ϑ; this is plotted in figure 2.2. Where the variance dips below the blue line, the variance is squeezed, since, in these regions, eq. (2.34) is satisfied. It must be noted that the plot just shows sinusoidal functions plotted in logarithmic scale.

The fluctuations of the electric field can be expressed in terms of the field phase angle χ as [LK87]

$$\left\langle (\Delta\hat{E}(\chi))^2 \right\rangle = \frac{1}{4}\left[e^{-2r}\cos^2\left(\chi - \frac{\theta}{2}\right) + e^{2r}\sin^2\left(\chi - \frac{\theta}{2}\right)\right]. \tag{2.47}$$

Each period of the electric field corresponds to an increase of the field phase angle by 2π, during which the noise level envelope from eq. (2.47) reaches two maxima and two minima. With $\chi = \omega t$, eq. (2.47) can be expressed in time domain as

$$\left\langle (\Delta\hat{E}(t))^2 \right\rangle = \frac{1}{4}\left[e^{-2r}\cos^2(\omega t) + e^{2r}\sin^2(\omega t)\right], \tag{2.48}$$

where, without loss of generality, the squeezing angle θ was set to be zero and ω is the angular frequency of the light mode for which the quadrature operators $\hat{X}$ and $\hat{Y}$ were defined. From

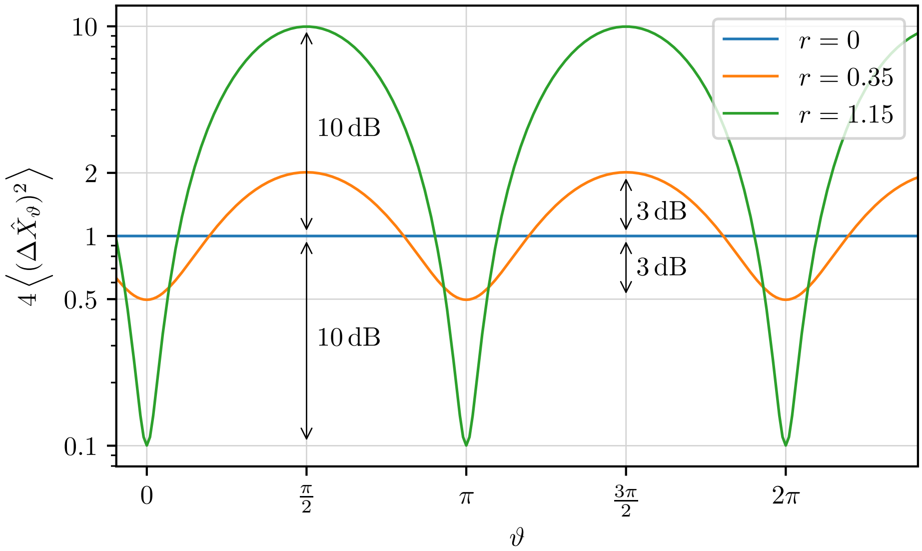

Figure 2.2.: $4\left\langle(\Delta\hat{X}_\vartheta)^2\right\rangle$ for two squeezed states with $r = 0.35$ (orange) and $r = 1.15$ (green) and a non-squeezed coherent state with $r = 0$ (blue) versus the quadrature angle ϑ. The additional prefactor 4 was chosen for the plot such that the variance of the vacuum state is normalized to 1. Squeezed and antisqueezed quadratures are separated by $\Delta\vartheta = \frac{\pi}{2}$ and amplified/attenuated by the same factor. The displayed values belong to squeezed states whose fluctuations are squeezed 3 dB and 10 dB below the vacuum fluctuations in the squeezed quadrature (and antisqueezed in the orthogonal quadrature respectively).

this representation, it becomes apparent that, in time domain, squeezing can be understood as a periodically increasing and decreasing noise level, oscillating at twice the frequency of the corresponding mode of the light field, as depicted in figure 2.3.

For a displaced squeezed state as in eq. (2.36), the squeezing angle θ allows to continuously adjust the phase shift between the time-dependent field fluctuations and the sinusoidal electric field: For $\theta = 0$, the noise is minimal in the amplitude quadrature, i.e., when the electric field reaches its extreme points. In contrast to that, $\theta = \pi$ shifts the phase of minimal field fluctuations to the zero-crossings of the electric field, yielding a phase-squeezed state.

2.4. Nonlinear optics for generation of squeezed states of light

The fact that $\hat{S}(\xi)$ always contains two successive applications of $\hat{a}$ and $\hat{a}^\dagger$ suggest that quadrature squeezing can be generated in processes that create or annihilate two photons at a time. The squeezing operator from eq. (2.35) can be experimentally realized in nonlinear optical systems described by the Hamiltonian

$$\hat{\mathcal{H}} = \hbar\omega\hat{a}^\dagger\hat{a} + \hbar\omega_p\hat{b}^\dagger\hat{b} + i\hbar\chi^{(2)}(\hat{a}^2\hat{b}^\dagger - \hat{a}^{\dagger 2}\hat{b}). \tag{2.49}$$

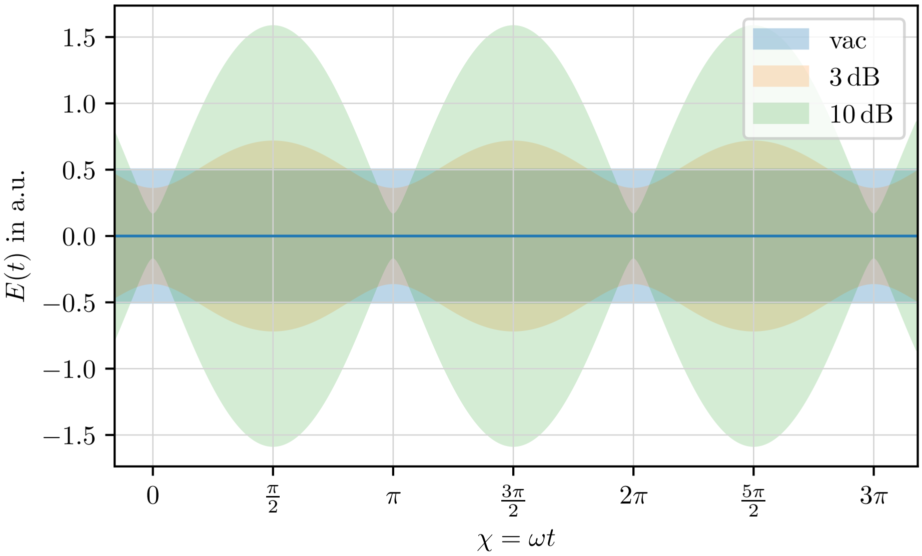

Figure 2.3.: Envelope of the uncertainty of the electric field $E(t)$. In time domain, squeezed vacuum can be understood as periodically increasing and decreasing envelope to the fluctuations of the electric field. While $\langle E(t) \rangle = 0$ throughout, its standard deviation is depicted by the shaded regions for the three squeezing levels from figure 2.2.

This Hamiltonian describes two light fields: one with frequency ω whose mode is generated by $\hat{a}^\dagger$, and a pump mode with $\omega_p = 2\omega$ whose excitations are generated by $\hat{b}^\dagger$. Aside from the energy stored in the fundamental and harmonic mode, it contains an interaction term where two quanta of frequency ω are generated from one annihilated quantum of frequency ω_p or vice versa. Assuming a strong coherent pump field, the parametric approximation holds and the creation and annihilation operators can be replaced by the $\mathbb{C}$-numbers $\beta^* e^{i\omega_p t}$ and $\beta e^{-i\omega_p t}$. The interaction part of the Hamiltonian then reads

$$\hat{\mathcal{H}}_I = i\hbar \left(\eta^* \hat{a}^2 - \eta \hat{a}^{\dagger 2} \right) \tag{2.50}$$

with $\eta = \chi^{(2)} \beta$. After time t, an initial vacuum state becomes a squeezed state through the time evolution

$$\hat{U}_I(t,0) \left|0\right\rangle = e^{-\frac{i\hat{H}_I t}{\hbar}} \left|0\right\rangle = e^{(\eta^* t \hat{a}^2 - \eta t \hat{a}^{\dagger 2})} \left|0\right\rangle , \tag{2.51}$$

which clearly corresponds to eq. (2.35) when $2\eta t = \xi$. Therefore, the following sections will discuss how the interaction between two harmonic modes can be realized experimentally, briefly sketching the in-detail treatment from the book by Boyd [Boy08].

2.5. Frequency conversion in non-centrosymmetric materials

The experimental generation of squeezing requires a material with a nonlinear response of the polarizability $\tilde{P}(t)$ to an incident electric field $\tilde{E}(t)$:

$$\tilde{P}(t) = \epsilon_0 \left[\chi^{(1)} \tilde{E}(t) + \chi^{(2)} \tilde{E}^2(t) + \dots\right], \tag{2.52}$$

where $\chi^{(n)}$ is the n-th order nonlinear susceptibility. While $\chi^{(1)}$ describes the linear response to an incident light field, the higher order terms allow an interaction of electromagnetic waves of different frequencies inside the medium. Typically, the lowest orders $\chi^{(2)}$ or $\chi^{(3)}$ are used for this purpose. $\chi^{(2)} \neq 0$ arises only in non-centrosymmetric media, that is a limited class of crystals that are not symmetric under spatial inversion. In centrosymmetric crystals or unordered materials such as gases and liquids, $\chi^{(3)}$ is the lowest order nonlinear polarizability that allows frequency conversion. Typically, the magnitude of the nonlinear susceptibility decreases with increasing order.

It needs to be noted that, in general, the $\chi^{(i)}$ are tensors, linking incident electric field components to the resulting components of the polarization; for the general case, this relation reads [Boy08]

$$P_i(\omega_n + \omega_m) = \epsilon_0 \sum_{jk} \sum_{(nm)} \chi^{(2)}_{ijk}(\omega_n + \omega_m, \omega_n, \omega_m) E_j(\omega_n) E_k(\omega_m), \tag{2.53}$$

where the indices i, j and k are the different Cartesian components of the electric fields, and the summation over (nm) indicates the summation over all combinations of ω_n and ω_m for which energy is conserved. However, the tensors $\chi^{(2)}_{ijk}(\omega_n + \omega_m, \omega_n, \omega_m)$ are subject to different kinds of symmetries because the boundary conditions of the physical model require invariance under the permutation and interchange of certain indices. This reduces the number of independent tensor elements. Especially for frequencies far below the resonance frequency of the optical material, the nonlinear susceptibility is in good approximation independent of the frequency, and thus all frequency indices can be interchanged. In this so-called Kleinman symmetry, the number of independent tensor elements reduces to 10.

The tensor element $\chi^{(2)}_{ijk}$ allows to calculate the contribution to the i-th component of the polarization by two fields polarized along the directions j and k. Thus, there are only six possible combinations of incoming directions, which can be mapped to another index l for shorthand notation:

(jk)	(11)	(22)	(33)	(23)/(32)	(13)/(31)	(12)/(21)
l	1	2	3	4	5	6

With this, the nonlinear susceptibility can be written in the commonly used form

$$d_{il} = \frac{1}{2}\chi^{(2)}_{il} = \frac{1}{2}\chi^{(2)}_{ijk}. \tag{2.54}$$

Consequently, d_{33} corresponds to $\frac{1}{2}\chi^{(2)}_{333}$ and describes the interaction between three field components, all aligned with the same crystal axis. For a given experimental geometry (e.g., a fixed polarization of the input beam(s) and a fixed interaction length in the nonlinear optical medium) the magnitude of the polarization $P(\omega) = \left|\vec{P}(\omega)\right|$ generated from the incident field can be calculated from the magnitude of the entering light fields $E(\omega) = \left|\vec{E}(\omega)\right|$ via a scalar relation, using an effective nonlinearity d_{eff}:

$$P(\omega_3) = 4\epsilon_0 d_{\text{eff}} E(\omega_1)E(\omega_2) \tag{2.55}$$

For simplicity, the processes described in the following sections will be discussed in this formalism with a scalar $\chi^{(2)}$, bearing in mind that a corresponding equations can be formulated for each combination of field components.

2.5.1. Second-harmonic generation

In the presence of a $\chi^{(2)}$-nonlinearity, an incoming plane electromagnetic wave of the form

$$\tilde{E}(t) = Ee^{-i\omega t} + c.c. \tag{2.56}$$

leads to the appearance of an additional wave of frequency 2ω, since the second term in the polarizability in eq. (2.59) becomes [Boy08]

$$\tilde{P}^{(2)}(t) = \epsilon_0\chi^{(2)}\tilde{E}^2(t) = 2\epsilon_0\chi^{(2)}EE^* + \epsilon_0\chi^{(2)}\left(E^2e^{-i2\omega t} + c.c.\right). \tag{2.57}$$

Here, the first term yields a constant offset of the electric field, while the second term is a field oscillating at frequency 2ω. This process is called second-harmonic generation (SHG); it can be understood as combining two field quanta $\hbar\omega$ at the fundamental frequency ω to one quantum at frequency 2ω, as depicted in figure 2.4.

2.5.2. Optical parametric amplification

More complex frequency conversion can occur when the incident light field consists of two (or even more) different frequencies: An electric field described by

$$\tilde{E}(t) = E_1e^{-i\omega_1 t} + E_2e^{-i\omega_2 t} + c.c. \tag{2.58}$$

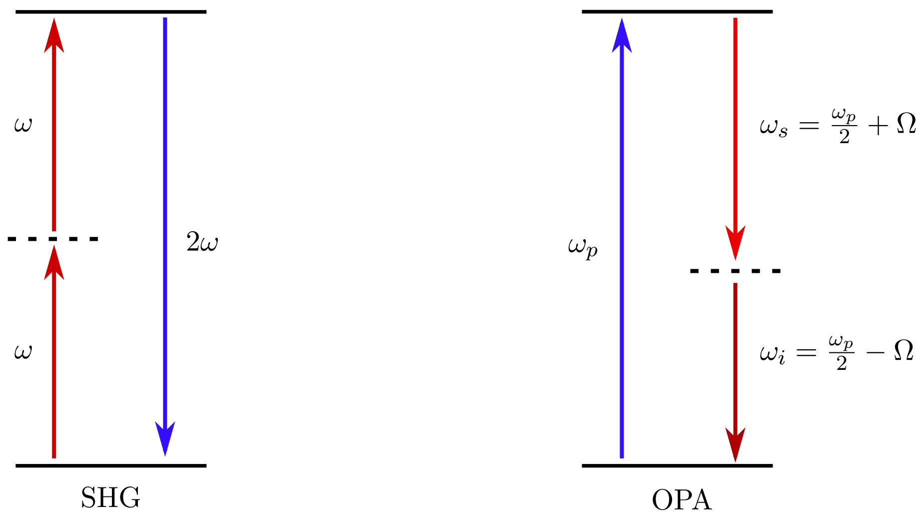

Figure 2.4.: Level schemes for SHG and OPA. In SHG, two photons of energy $\hbar\omega$ are combined to one photon with energy $2\hbar\omega$. For OPA, one photon of energy $\hbar\omega_p$ is split into two photons with frequencies ω_s and ω_i, such that energy is conserved: $\hbar\omega_p = \hbar\omega_s + \hbar\omega_i$.

leads to a polarization that contains contributions from several different frequencies:

$$\begin{aligned}\tilde{P}^{(2)}(t) =&\epsilon_0\chi^{(2)}\left(E_1^2 e^{-2i\omega_1 t} + E_2^2 e^{-2i\omega_2 t} + 2E_1E_2 e^{-i(\omega_1+\omega_2)t} + 2E_1E_2^* e^{-i(\omega_1-\omega_2)t} + c.c.\right)\\ &+ 2\epsilon_0\chi^{(2)}\left(E_1E_1^* + E_2E_2^*\right)\end{aligned} \tag{2.59}$$

Here, the first two terms in the first line are second harmonics of the incident frequencies ω_1 and ω_2, the third term oscillates with the sum of both frequencies $\omega_1 + \omega_2$, and the fourth term oscillates with the difference frequency $\omega_1 - \omega_2$. The latter two effects are therefore called sum frequency generation (SFG) and difference frequency generation (DFG). Given a pump beam with frequency ω_p and a signal beam with frequency $\omega_s < \omega_p$, in DFG, one quantum of the pump light with energy $\hbar\omega_p$ can be split into two photons: one of energy $\hbar\omega_s$ via stimulated emission into the signal beam, and an idler photon with $\hbar\omega_i = \hbar\omega_p - \hbar\omega_s$, satisfying energy conservation.

The signal field ω_s does not have to be a classical field, but can also arise from vacuum fluctuations; this process is called spontaneous parametric down-conversion (SPDC). For long interaction lengths (e.g., in an optical parametric oscillator (OPO), where the nonlinear medium is placed inside a high finesse cavity), this is a self-amplifying effect, since DFG of this newly generated photon may trigger the stimulated emission of other photons at frequency ω_s into the same mode. Similar to a laser, an OPO has a lasing threshold above which the stimulated emission becomes the dominating effect and the photons are amplified to coherent output beams at frequencies ω_s and ω_i. Constructive interference between the generated photons occurs only when the phases of all involved frequencies match; this is discussed in detail in sections 2.7 and 2.8. The phase-matching condition can be modified by external parameters such as crystal angle or crystal temperature. It determines which of the processes in eq. (2.59) are allowed and which are suppressed, and for which specific frequencies ω_s and ω_i a DFG process will be favored.

2.6. Squeezing in OPO below threshold

If operated below threshold, no bright output beams are produced in the OPO; nevertheless, the SPDC creates pairwise virtual photons in corresponding signal and idler modes. Due to their entanglement, the quantum fluctuations of these modes are correlated and can interfere (constructively and destructively) with each other. In this way, there are times where the total fluctuations reduce below the vacuum fluctuations of a single mode; a squeezed vacuum state is created! Close to the threshold of the OPO, almost all virtual photons are correlated to each other due to the stimulated emission, such that constructive and destructive interference is reached for them at the same time. For this reason, strongest squeezing and anti-squeezing are realized for input powers just below the OPO threshold.

In the sideband picture, squeezing can be understood as two-mode squeezed states of the modes with frequency $\omega_s = \frac{\omega_p}{2} + \Omega$ and $\omega_i = \frac{\omega_p}{2} - \Omega$, that together satisfy energy conservation from one pump photon with ω_p. Figure 2.5 illustrates the idea of noise cancellation in two-photon-correlated states: In a rotating frame with $\frac{\omega_p}{2}$, the signal and idler sidebands rotate both at the angular frequency Ω, but in opposite directions. Due to the correlation between signal and idler modes, the electric fields (and their fluctuations) periodically interfere constructively and destructively – twice per rotation. This leads to a periodic modulation of the vacuum noise with frequency 2Ω.

In the experiment, the low noise signals can be measured via balanced homodyne detection (see section 2.10) and subsequently electronically filtered to yield the noise in one specific quadrature $\hat{X}_\vartheta$ in a narrow frequency band $\Omega \pm \Delta\Omega$ of interest. Here, Ω is the sideband frequency for which the squeezing is measured, and $\Delta\Omega$ is the resolution bandwidth.

Below threshold, SPDC can, in principle, entangle any virtual photon pair for which energy conservation holds, and thus there is no fundamental limitation for which sideband frequencies Ω the noise can be squeezed. However, there are some practical limitations that suppress squeezing in certain frequency ranges. As already discussed, the conversion via SPDC requires an appropriate phase matching, and efficient generation of squeezing is only possible within the bandwidth of the parametric gain (which was in this experiment on the order of several GHz). When the squeezing is generated inside an optical cavity, the cavity imposes the additional constraint that the frequencies of both generated photons needs to be resonant to the cavity, that is that the sideband frequency Ω is smaller than the cavity linewidth γ, which typically reduces the bandwidth of squeezing to some tens of MHz. If squeezing at

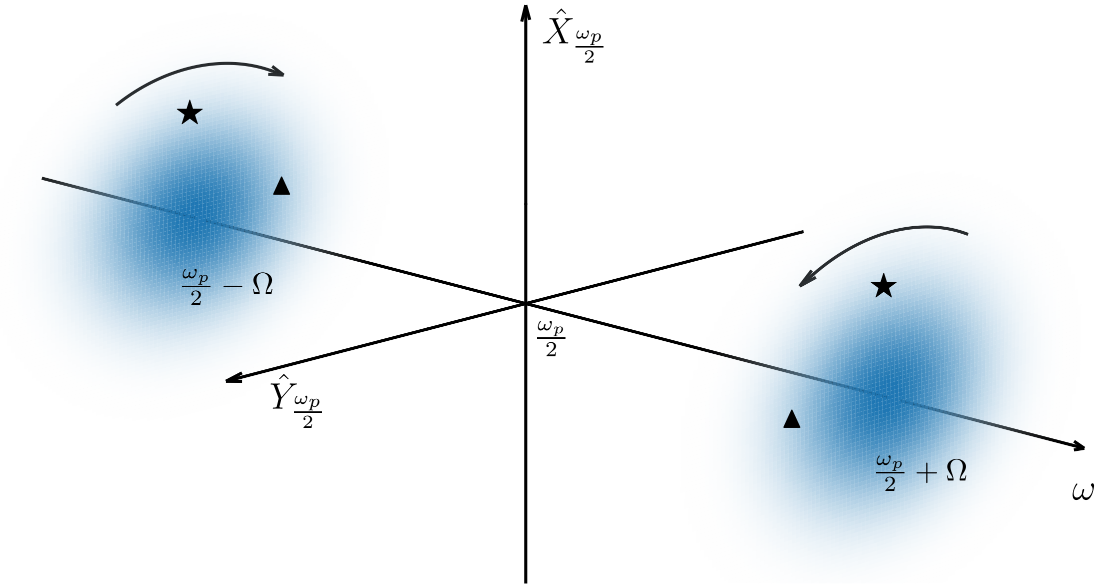

Figure 2.5.: Squeezed states of light in the sideband picture. One photon of frequency ω_p is down-converted to a photon pair at $\frac{\omega_p}{2} + \Omega$ and $\frac{\omega_p}{2} - \Omega$. In the rotating frame of $\frac{\omega_p}{2}$, the phasors rotate in opposite directions with frequency Ω, periodically yielding constructive and destructive interference of the correlated field fluctuations. The stars show constructive interference, while an instant later, the fluctuations would point towards the triangles in different directions, yielding destructive interference and reducing the combined fluctuations below the vacuum fluctuations of each individual mode. Figure inspired by [Sch17].

higher sideband frequencies is required, it is worth noting that if Ω is an integer multiple of the cavity's free spectral range, signal and idler photons can both be resonant with the cavity, albeit in different longitudinal modes.

2.7. Phase matching

As stated in the previous section, appropriate phase matching is important for efficient nonlinear interactions, as required for SHG or the generation of squeezed states of light in an OPO. This section briefly sketches the origin of the phase mismatch term and discusses techniques how to experimentally tune it. For a detailed derivation and solution of the coupled equations for SFG, SHG and DFG, see chapter 2 of [Boy08].

All three nonlinear optical processes sketched so far follow the same fundamental principle: One or more waves of the form of eq. (2.56) are sent through a nonlinear medium, which leads to the creation of an additional output wave at a new frequency. From eq. (2.59), it can be seen that the magnitude of the polarizability at the new frequency (which drives the new output field) depends on the amplitude of the incident wave(s).

Inside the medium, all waves have to obey Maxwell's equations. In the presence of a nonlinear polarization, this gives rise to a set of coupled differential equations, which link the amplitudes of all participating waves to one another. In the slowly varying amplitude approximation, for an SHG process driven by an incident field $\tilde{E}_1(t) = A_1 e^{i(\omega_1 t - k_1 z)}$, the equation for the amplitude A_2 of the newly generated wave $\tilde{E}_2$ is given by [Boy08]

$$\frac{\mathrm{d}A_2}{\mathrm{d}z} = \frac{i\omega_2^2 d_{\text{eff}}}{k_2 c^2} A_1^2 e^{i\Delta k z}, \tag{2.60}$$

where d_{eff} is the effective nonlinearity from eq. (2.55), and $\Delta k = 2k_1 - k_2$ is the phase mismatch. In the photon picture, it can be understood as summing the k-vectors of all incoming photons and subtracting those of all outgoing photons that participate in the nonlinear interaction. Since the SHG process converts two photons of ω_1 to one of $\omega_2 = 2\omega_1$, in this case $\Delta k = 2k_1 - k_2$. For SFG and DFG, similar differential equations can be formulated, in which the phase mismatch Δk can be interpreted in exactly the same way.

In the undepleted pump approximation, where the amplitude A_1 of the incoming beam does not change with z, eq. (2.60) can straightforwardly be integrated along the propagation direction z over the crystal length L. In this way, the amplitude $A_2(L)$ at the end of the crystal can be calculated. With the boundary condition $A_2(0) = 0$, this yields

$$A_2(L) = \frac{i\omega_2^2 d_{\text{eff}}}{k_2 c^2} A_1^2 \int_0^L e^{i\Delta k z}\, dz = \frac{i\omega_2^2 d_{\text{eff}}}{k_2 c^2} A_1^2 \left(\frac{e^{i\Delta k L} - 1}{i\Delta k} \right). \tag{2.61}$$

With $\left| \frac{e^{i\Delta k L} - 1}{i\Delta k} \right|^2 = L^2 \operatorname{sinc}^2\left(\frac{\Delta k L}{2}\right)$, absolute-squaring eq. (2.61) yields the output intensity

$$I_{\text{out}} = |A_2(L)|^2 = \frac{\omega_2^4 d_{\text{eff}}^2}{k_2^2 c^4} A_1^4 \left| \frac{e^{i\Delta k L} - 1}{i\Delta k} \right|^2 = I_{\max} \cdot \operatorname{sinc}^2\left(\frac{\Delta k L}{2}\right), \tag{2.62}$$

where, in the last step, all experimental parameters were summarized into the maximal output intensity $I_{\max}$ for the given parameters.

While the value of $I_{\max}$ and the contributions to Δk depend on the specific process, the phase mismatch factor $\operatorname{sinc}^2\left(\frac{\Delta k L}{2}\right)$ is universal for all above named nonlinear interaction processes, including the generation of squeezing in an OPO below threshold. It is depicted in figure 2.6 against $\frac{\Delta k L}{2}$. From this representation, it can be seen that significant nonlinear interaction between waves of different frequencies can occur only in a narrow band for which $\left|\frac{\Delta k L}{2}\right| \ll \pi$. Optimal conversion is achieved for $\Delta k = 0$. It must be noted that this result was derived using the approximation of plane waves; for focused Gaussian laser beams, optimal conversion requires a phase mismatch $\Delta k \neq 0$ to additionally account for the differences in Gouy phase between the fundamental and harmonic beam; for a more detailed treatment, see section 2.10 of [Boy08]. However, for clarity, the following sections will continue to assume plane waves.

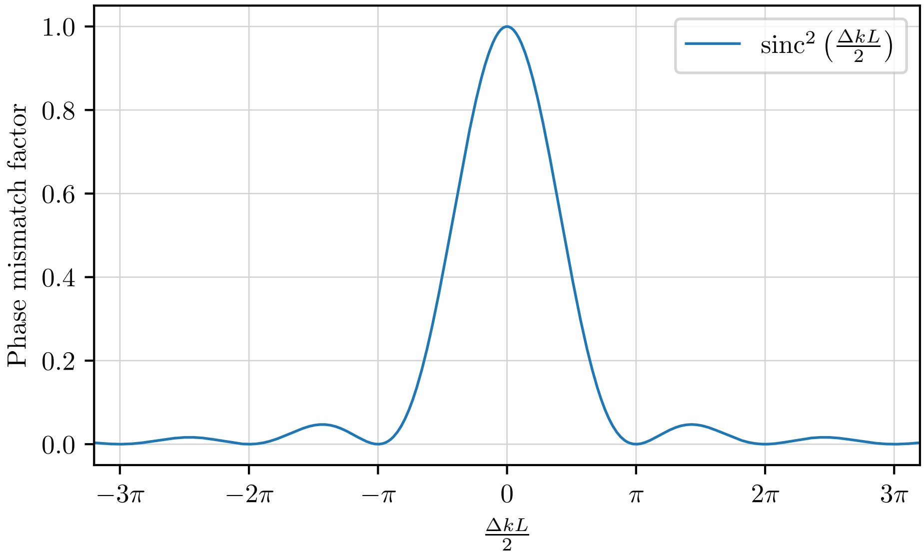

Figure 2.6.: Phase mismatch factor. Only when $\left|\frac{\Delta kL}{2}\right| \ll \pi$, the phases overlap coherently. For bigger phase mismatches, the frequency conversion is suppressed.

For the SHG process with $\omega_2 = 2\omega_1$, the phase-matching condition $\Delta k = 0$ can be written as

$$2k_1 = k_2 \quad \Leftrightarrow \quad 2\frac{n_{\omega_1}\omega_1}{c} = \frac{n_{2\omega_1}2\omega_1}{c}, \tag{2.63}$$

which requires for optimal conversion that the refractive indices are the same for fundamental and second harmonic: $n_{\omega_1} = n_{2\omega_1}$. This is typically not satisfied, since in normally dispersed materials, $n(\omega)$ increases monotonically with frequency. One solution is to use nonlinear media that show birefringence, such that the refractive indices are different along different polarization axes. In this way, equation eq. (2.63) can be satisfied when fundamental and harmonic wave have mutually orthogonal polarizations. To satisfy eq. (2.63) for specific given frequencies and adjust the refractive indices accordingly, typically, the crystal angle or the temperature of the crystal are tuned. For critical phase matching, the effective refractive index can be composed from the refractive indices n_o and n_e along the ordinary and extraordinary crystal axes, respectively, by adjusting the relative angle between the incident beam and the crystal ϕ:

$$n_{\mathrm{eff}} = n_{\mathrm{o}} \sin\phi + n_{\mathrm{e}} \cos\phi. \tag{2.64}$$

Critical phase matching is very sensitive to beam and angle misalignment, and the birefringence under an angle introduces a beam displacement between ordinary and extraordinary beams. This is avoided in non-critical phase matching, where all waves travel along the same crystal axis, and the different temperature dependencies of n_{o} and n_{e} are used to satisfy eq. (2.63) for the desired combination of frequencies.

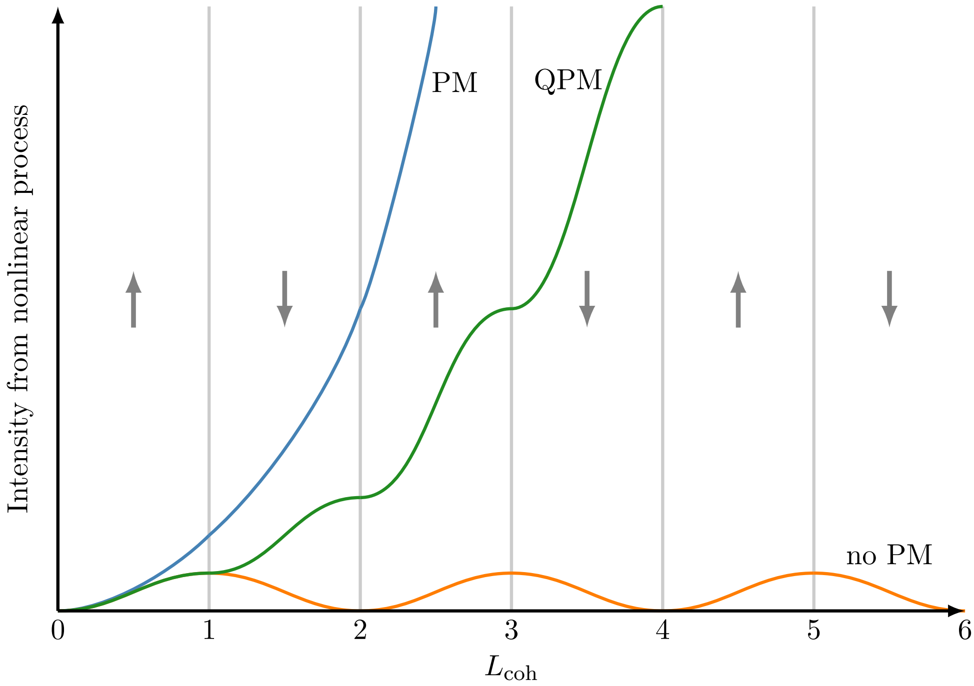

Figure 2.7.: Quasi-phasematching in periodically poled materials. Without phase matching, after each coherence length L_{coh} the newly generated light would start to interfere destructively with the previously generated light (orange). A periodic inversion of the crystal every L_{coh} adds an additional phase shift π and allows to constructively interfere light generated in successive coherence lengths; this process is linear in amplitude and quadratic in the generated intensity (green). For comparison, the blue curve shows a (hypothetical) material with the same optical nonlinearity that is perfectly phasematched, such that coherent amplification is satisfied over the whole crystal. Figure modified from [Sch19].

2.8. Quasi-phasematching

The aforementioned phase-matching techniques only allow frequency conversion involving light of different polarizations. However, for some materials, like e.g., $KTiPO_4$, significantly higher nonlinear coupling arises between waves of the same polarization, that is d_{11}, d_{22} or d_{33}. As discussed above, in this case, Δk cannot vanish. When evaluating the output intensity (e.g., of the SHG process) for different crystal lengths, the phase mismatch would lead to a periodic exchange of energy between the involved waves (see the orange line in figure 2.7), yielding only very low or no conversion at all. When the traveling distance inside the crystal exceeds the coherence length L_{coh}, the light generated beyond that point interferes destructively with the light generated up to this point.

This effect can be avoided by quasi-phasematching, where the crystal material is periodically poled [Fej+92]; in this case, the crystal structure is inverted after every coherence length L_{coh}, which inverts the sign of the $\chi^{(2)}$ nonlinearity, and corresponds to an additional phase shift of π per coherence length. In this way, the light generated in the next coherence length interferes constructively with the light already created; this is shown by the green trace in figure 2.7. Using this periodic nonlinearity, the coupled set of differential equations for the amplitude of the generated light has a similar form like eq. (2.60), but with a reduced effective nonlinearity [Boy08]

$$d_{\text{eff}} = \frac{2}{\pi} \cdot d_{33} \tag{2.65}$$

and a modified phase-matching condition

$$\Delta k_Q = k_1 + k_2 - k_3 + \frac{2\pi}{\Lambda}, \tag{2.66}$$

where $\Lambda = 2L_{\text{coh}}$ is the poling period, consisting of two crystal domains of opposite sign. Thus, the set of wave vectors between which nonlinear interaction can occur is determined by the poling period Λ chosen in the manufacturing process and can be fine-tuned by adjusting the temperature of the crystal, which changes the domain lengths by thermal expansion. For frequency conversion in the visible range in PPLN or PPKTP, Λ is typically on the order of a few micrometers. Experimentally, the periodic poling can be realized, e.g., by stacking crystal slices onto each other; however, the common method to date is flux-growing a crystal in the presence of a strong electric field and reversing the direction of the electric field after each domain of thickness $\Lambda/2$ is grown.

As can be seen from eq. (2.65), quasi-phasematching comes at the cost of reduced effective nonlinearity d_{eff} due to the phase walk-off within each domain. The upper blue line in figure 2.7 shows the hypothetical output power if it were possible to achieve a perfect phase matching with the nonlinearity d_{33} everywhere in the crystal. Quasi-phasematching is commonly used when the coupling coefficient between the same polarizations (d_{11}, d_{22}, d_{33}) is much stronger than the off-diagonal tensor elements in eq. (2.54). In this case, even the reduced d_{eff} exceeds the nonlinearity gained from perfectly (critical or non-critical) phase-matched orthogonal polarizations.

2.9. Squeezing susceptibility to optical losses

Since squeezing originates from the generation of correlated photon pairs, it becomes apparent that absorption of one photon breaks the entanglement, and consequently the destructive interference between upper and lower sideband is no longer possible: The noise level rises for quadratures in which it was reduced due to destructive interference, and it decreases for quadratures where beforehand constructive interference of fluctuations led to increased noise levels (antisqueezing). Therefore, squeezed states are very susceptible to optical losses.

Optical losses can be modeled like a beam splitter, where a quantum state of light is overlapped with a vacuum mode that is incident on the “empty” port of the beam splitter [LK87].

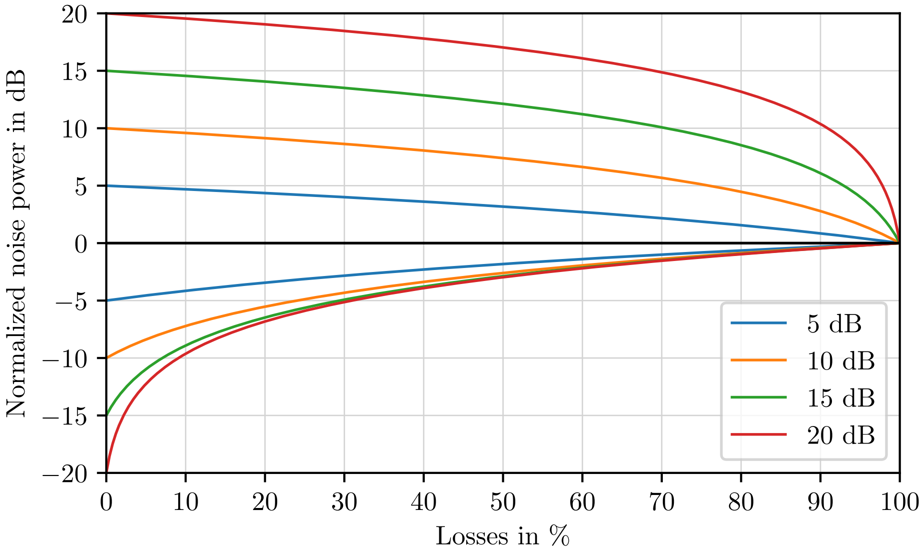

Figure 2.8.: Detectable squeezing and antisqueezing levels versus detection losses. Already losses of 10 % significantly reduce the achievable squeezing level while the losses have only limited effect on the antisqueezing level.

The splitting ratio can be interchangeably formulated in terms of the power losses L or the detection efficiency $\eta^2 = 1 - L$. The variance of the resulting state is calculated from $(\Delta\hat{X}_\theta)^2$ and $(\Delta\hat{X}_{\text{vac}})^2$ as [Sch17]

$$(\Delta\hat{X}_{\theta,\text{loss}})^2 = (1-L)\cdot(\Delta\hat{X}_\theta)^2 + L\cdot(\Delta\hat{X}_{\text{vac}})^2. \tag{2.67}$$

Figure 2.8 plots eq. (2.67) for several initial squeezing levels and varying overall losses in logarithmic scale. For moderate losses of 10 – 20 %, the squeezing decreases significantly, while the antisqueezing stays approximately at the same level. This happens because, on a linear scale, the vacuum noise would have the same effect on squeezing and antisqueezing, but the relative change in noise is much bigger when the initial noise level is much lower. It is as well for this reason, that the susceptibility to losses increases with increasing squeezing value.

If the losses L of the system are not known, they can be calculated from the measured and dark noise corrected squeezing and antisqueezing levels, here denoted as $(\Delta\hat{X}_{\text{sqz}})^2$ and $(\Delta\hat{X}_{\text{asqz}})^2$. Plugging $(\Delta\hat{X}_{\text{vac}})^2 = \frac{1}{4}$ from eq. (2.26) into eq. (2.67) and replacing $(\Delta\hat{X}_\theta)^2$ with the lossless optimal squeezing and antisqueezing levels from eq. (2.45) and eq. (2.46), respectively, the set of equations can straightforwardly be solved for L, yielding

$$L = \frac{1 - (\Delta\hat{X}_{\text{sqz}})^2(\Delta\hat{X}_{\text{asqz}})^2}{2 - (\Delta\hat{X}_{\text{sqz}})^2 - (\Delta\hat{X}_{\text{asqz}})^2}. \tag{2.68}$$

2.10. Balanced homodyne detection

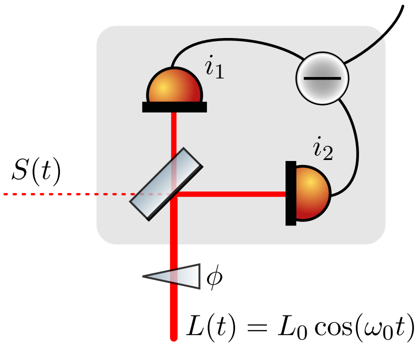

Figure 2.9.: Balanced homodyne detection. A small signal $S(t)$ is overlapped with a strong coherent local oscillator $L(t)$ on a 50:50 beam splitter. Both output beams are recorded and the photo currents are subtracted from each other. The resulting signal is a phase sensitive amplification of the weak signal. The phase shift ϕ allows to select the readout quadrature. Component icons by [Fra].

The variances $(\Delta\hat{X}_{\mathrm{sqz}})^2$ and $(\Delta\hat{X}_{\mathrm{asqz}})^2$ can (as well as any quadrature in between) be measured via balanced homodyne detection (BHD) [CLG87]. In BHD, a weak signal $S(t)$ is overlapped on a 50:50 beam splitter with a strong coherent local oscillator with amplitude L_0. The resulting output beams are detected and their photo currents are subtracted from each other as shown in figure 2.9.

As derived explicitly in appendix A, BHD has two key properties that make it suitable for the detection of very weak signals: First, the subtraction of photocurrents cancels all classical and quantum noises of the local oscillator beam, such that they do not disturb the measurement of $S(t)$. Secondly, the weak signal $S(t)$ is amplified by the amplitude L_0 of the local oscillator – in this way, also very small signals, such as (squeezed) vacuum fluctuations, can be measured. It is also shown in appendix A that BHD is robust against unequal detection efficiencies in both arms.

In the case of squeezing, no classical signal is present in the signal path, but the signal consists only of noise terms. The total noise in the signal path can be written in term of the noises $s^c(t)$ and $s^s(t)$ in mutually perpendicular quadratures as [Kor20]

$$S(t) = s^c(t)\cos(\omega_0 t) + s^s(t)\sin(\omega_0 t). \tag{2.69}$$

Sending this signal onto a lossless BHD yields (see eq. (A.15) in appendix A)

$$i_1 - i_2 \propto L_0\Big(s^c(t)\cos\phi + s^s(t)\sin\phi\Big), \tag{2.70}$$

where ϕ is the homodyne readout angle, i.e., the relative phase between the local oscillator and the signal beam. In the experiment, ϕ can easily be adjusted by increasing the optical path length in either the signal or the local oscillator path; e.g., by shifting one mirror in the beam path with a piezoelectric actuator. For $\phi = 0$, the BHD signal consists of the fluctuations $s^c(t)$ amplified by the local oscillator amplitude L_0. Similarly, by setting $\phi = \pi/2$, the noise in the other quadrature can be extracted.

BHD can be thought of as a demodulation between the signal and the local oscillator, and therefore, the resulting signal no longer oscillates at ω_0. Since $s^c(t)$ and $s^s(t)$ are by design random fluctuations, for chosen quadrature readout angle ϕ, the BHD signal shows random fluctuations, from which physical meaning can only be extracted by filtering its frequency. This is performed by a spectrum analyzer, which can either record the noise spectrum over a broad frequency band or determine the noise level at a specific sideband frequency Ω in a zero-span measurement (see also section 2.6). In this way, the squeezed and antisqueezed noise levels can be obtained for each specific sideband frequency and compared to the fluctuations of a vacuum state at these frequencies.

3. Efficient frequency conversion in a monolithic SHG cavity

The first stage of the experiment is the generation of the pump light for the squeezing cavity. Laser light with a wavelength of 800 nm is frequency-doubled in a monolithic SHG cavity to 400 nm. Periodically poled potassium titanyl phosphate (PPKTP) is used due to its high nonlinear susceptibility and the fact that its transparency window reaches down to approximately 380 nm. However, at the harmonic wavelength, substantial optical losses of around 20%/cm lead to a power dissipation and heating of the crystal when conversion occurs. This leads to a number of considerable effects in this experiment that will be presented and discussed in this chapter.

3.1. Properties of PPKTP

For both nonlinear cavities in this experiment, periodically poled $KTiPO_4$ (PPKTP) was chosen as the nonlinear crystal material because it offers many advantages compared to other commonly used nonlinear crystal materials. First of all, KTP has an extremely high optical nonlinearity ($d_{33} = (16.6 \pm 0.8)$ pm/V for 852 nm [Nik05]) compared to other nonlinear crystal materials. The nonlinearity increases slightly with decreasing wavelength in the visible and infrared region. Since d_{33} couples beams of the same polarization, the crystal must be periodically poled to quasi-phasematch both beams (see section 2.8). The effective nonlinearity reduces then to $d_{\text{eff}} = 10.5$ pm/V, which is still one order of magnitude higher than the coefficient of most ordinarily phase-matched materials like β-BaB_2O_4 (BBO) and LiB_3O_5 (LBO). The non-critical quasi-phasematching furthermore facilitates the experimental alignment, since beam walk-off is omitted. Only in this way, it is convenient to consider the monolithic cavity design presented in the following section 3.2.

Like most nonlinear crystals, PPKTP suffers from absorption in the UV-range. While BBO and LBO are transparent down to 200 nm and 155 nm respectively, PPKTP becomes opaque below 380 nm and already exhibits significant absorption losses around 400 nm. In previous measurements, the absorption in PPKTP has been measured to be $\alpha = 18.9$ %/cm at 397.5 nm [Yan+15] and $\alpha = 15.1$ %/cm at 423 nm [TR03]. At 800 nm, PPKTP is transparent

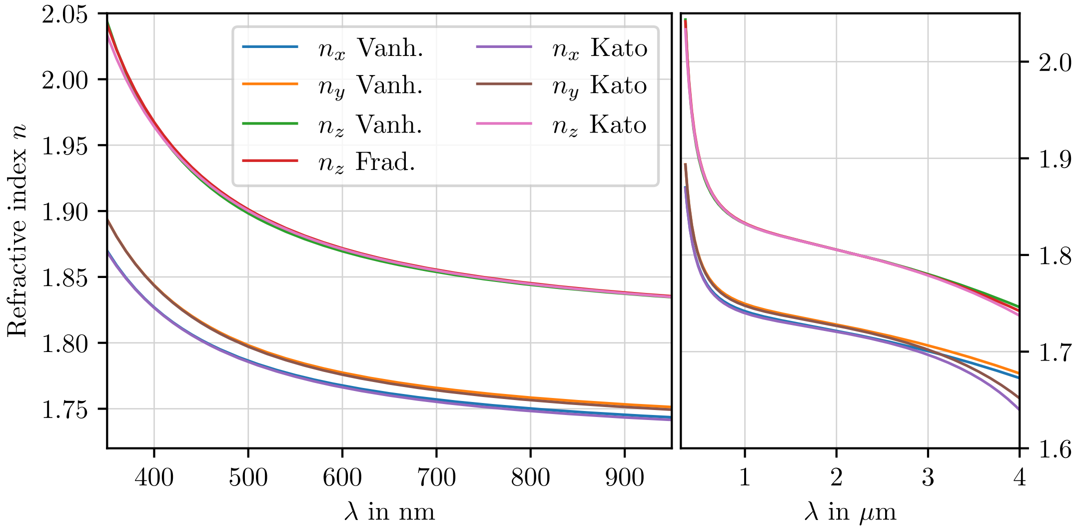

Figure 3.1.: Refractive indices of KTP as determined by Fradkin *et al.* [Fra+99], Vanherzeele *et al.* [VBZ88] and Kato *et al.* [KT02].

with measured absorption levels ranging between (127 ± 24) ppm/cm [Ste+13] and 0.1 %/cm [Yan+15]. Given this, PPKTP seems to be a reasonable tradeoff between absorption of the generated light and high optical nonlinearity.

PPKTP is a positive biaxial crystal [Nik05], and thus, the refractive indices depend on the polarization of the incident light. Since d_{33} couples light waves polarized along z, only this polarization is considered in the following. Several groups have determined Sellmeier equations for the refractive index with respect to the wavelength [KT02; VBZ88; Fra+99] (see figure 3.1). Although not specified for the near-UV wavelength range, all of them yield very good agreement for n_z around 400 nm: 1.9674 [Fra+99], 1.9650 [VBZ88] and 1.9640 [KT02]. While a deviation of 3‰ may be crucial for the manufacturing of periodically poled crystals according to given specifications, this uncertainty is well acceptable for the evaluations in this thesis. For 800 nm, the values for n_z yield 1.8452 [Fra+99], 1.8440 [VBZ88] and 1.8447 [KT02].

Due to the anisotropy of the crystal, also the thermal expansion coefficient α is different for each crystal axis. In the experiment, especially the thermal expansion along the beam propagation axis is of interest. At room temperature, $\alpha = (6.7 \pm 0.7) \cdot 10^{-6}/\mathrm{K}$ [EA03], which results in ordinary thermal expansion when the crystal is heated. However, this is not the dominating effect: Also the refractive index changes with temperature, with a wavelength-specific $\frac{\mathrm{d}n_z}{\mathrm{d}T}$. In [KT02], an equation of the form

$$\frac{\mathrm{d}n}{\mathrm{d}T} = \frac{A}{\lambda^3} + \frac{B}{\lambda^2} + \frac{C}{\lambda} + D \tag{3.1}$$

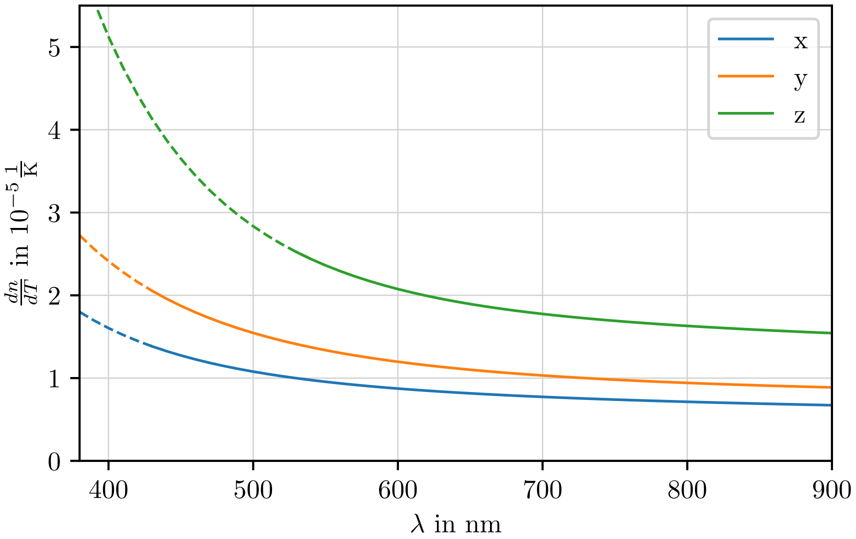

Figure 3.2.: $\frac{\mathrm{d}n}{\mathrm{d}T}$ versus wavelength. The solid lines are the wavelength regions from which the parameters in [KT02] were fitted. The dashed lines show extrapolations.

was fitted that allows to predict $\frac{\mathrm{d}n}{\mathrm{d}T}$ for all three polarization axes over the wavelength range $0.43 - 1.57\,\mu\mathrm{m}$. Figure 3.2 shows the wavelength range that was used to fit the curve as solid lines, together with an extrapolation to shorter wavelengths (dashed lines). It needs to be emphasized that the extrapolated numbers need to be handled with care and constitute only a rough estimate, especially for the relevant $\frac{\mathrm{d}n_z}{\mathrm{d}T}$. Comparison with the x- and y-components suggests that qualitatively, a further increase of $\frac{\mathrm{d}n_z}{\mathrm{d}T}$ is expected for shorter wavelengths; however, significant deviations from the fitted curve must be expected, and the calculated $\frac{\mathrm{d}n_z}{\mathrm{d}T} = 5.125 \cdot 10^{-5}\,\frac{1}{\mathrm{K}}$ at 400 nm may over- or underestimate the actual value. Albeit not giving a reliable quantitative result, this result allows the conclusion that for 400 nm, the effect of the temperature-dependent refractive index outnumbers the thermal expansion coefficient α by a factor of 7–8. In contrast to that, for 800 nm, the value for $\frac{\mathrm{d}n_z}{\mathrm{d}T} = 1.630 \cdot 10^{-5}\,\frac{1}{\mathrm{K}}$ is reliably known, which exceeds α by a factor of 2.43. When comparing $\frac{\mathrm{d}n_z}{\mathrm{d}T}$ for 400 nm and 800 nm, the refractive index changes with temperature more than three times as much for the harmonic wavelength as for the fundamental wavelength. Thus, a change in crystal temperature will first of all lead to an increment of the optical path length due to a change in refractive index and only later to thermal expansion of the bulk material, whose effect on the optical path length in the crystal will be small compared to the changes in the refractive indices.

3.2. Monolithic 3-temperature cavity design

The SHG cavity used in the experiment follows a monolithic cavity design by Prof. Dr. Roman Schnabel, Dr. Axel Schönbeck and Prof. Dr. Sebastian Steinlechner [SSS19], which was initially used as a squeezing cavity. It aimed at building the enhancement cavity around the nonlinear crystal as robust as possible and reduce the optical losses inside the cavity to a minimum by avoiding any anti-reflex-coating inside the cavity. Hence, the cavity's end mirrors are directly coated onto the nonlinear crystal.

3.2.1. SHG cavity parameters

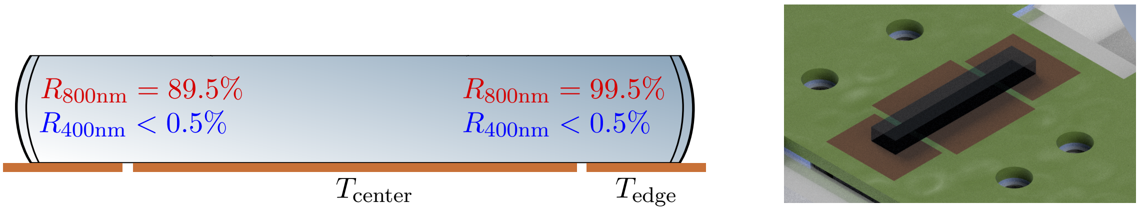

(a) Schematic of the SHG cavity

(b) CAD model

Figure 3.3.: The SHG crystal is placed on three metal plates, of which the center and one of the edge elements are temperature-controlled by Peltier elements. Mirrors with a radius of curvature of 10 mm are directly coated onto the crystal's end facets. The crystal is 11.56 mm long, 2 mm wide and 1 mm high.

The core element of the SHG is a 11.56 mm long PPKTP crystal, which is coated with reflectivities $R_{\text{in}} = 89.0\,\%$ and $R_{\text{out}} = 99.5\,\%$ at the fundamental wavelength of 800 nm (see figure 3.3). Together with the refractive index of $n_z = 1.8447$, this cavity has a free spectral range (FSR) of 7.034 GHz. For a fresh crystal, the absorption at 800 nm can be neglected (see section 3.1), and the chosen reflectivities yield a cavity with a finesse of 51.7 and a linewidth of 136.0 MHz.

To reduce optical absorption of the converted 400 nm light (and the thereby induced crystal damages and thermal expansion effects), the SHG cavity is only resonant for 800 nm. Both end mirrors are anti-reflex coated for 400 nm, such that the generated light can leave the cavity immediately. This comes at the cost of a reduced conversion efficiency in transmission, since the converted light power is split almost equally between both cavity output ports. Furthermore, there is no cavity that could define a TEM_{00} mode for the converted light; however, since it is generated from the intensity distribution of the well defined TEM_{00} mode of the pump beam, the beam shape and divergence of the converted light are sufficiently well-shaped to pump the squeezing cavity without using an additional mode cleaner.

The crystal's end facets have a radius of curvature of 10 mm, yielding a cavity mode with waist radius $w_0 = 28\,\mu\text{m}$ at the fundamental wavelength. This configuration has a Rayleigh length of $z_R = \pi w_0^2 n/\lambda = 5.75\,\text{mm}$. Consequently, the cavity mode diverges to a beam radius of approximately $\sqrt{2} \cdot 28\,\mu\text{m} \approx 40\,\mu\text{m}$ at the mirror surfaces. Here, the on-axis peak intensity $I_0(z) = \frac{2P_0}{\pi w^2(z)}$ drops to 50% of the intensity in the focus.

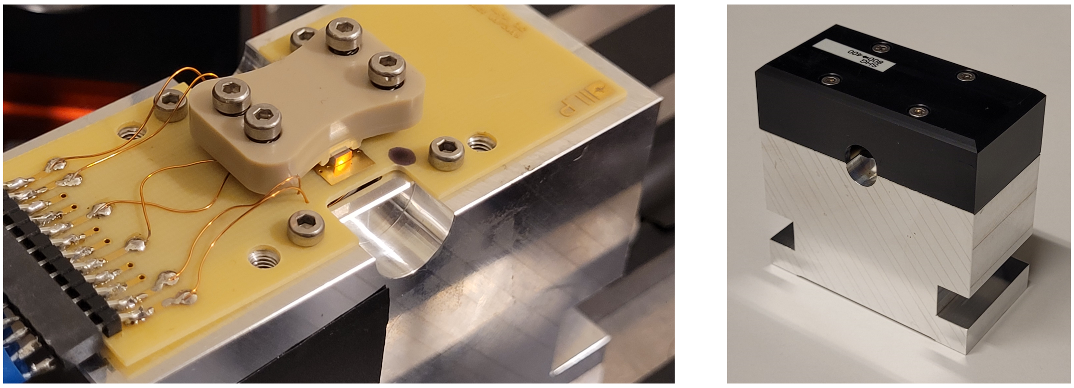

Figure 3.4.: Left: The nonlinear crystal is fixated on the circuit board with a yoke. The wires are connected to the Peltier elements below the board. Right: A housing reduces the airflow around the cavity.

For a confocal cavity, where the mirrors are placed at $z = z_R$ from the focal plane, the Gouy phases for different $\mathrm{TEM}_{\mathrm{nm}}$ modes $\phi_{\mathrm{nm}}(z) = -(1+n+m)\arctan\left(\frac{z}{z_R}\right)$ are multiples of π, which leads to simultaneous resonance of different modes. To avoid this degeneracy, the cavity length $L = 11.56\,\mathrm{mm}$ was carefully chosen, such that $L/2$ is close to, but not equal z_R.

3.2.2. Housing

To place the crystal at the correct beam height, apply the temperatures, and shield the crystal from surrounding airflow, it is placed in a housing that was designed by Dr. Axel Schönbeck and Dr. Jan Südbeck. Mechanically, four screws with springs gently clamp the crystal to a circuit board, which can be heated by two Peltier elements from below. The heat is transferred via metallic connections through the circuit board to the crystal. To avoid disturbances by air flow, the cavity is shielded by a cover surrounding the crystal. Two photos of the SHG cavity (with and without cover) are shown in figure 3.4. The temperature can be adjusted by a manual temperature controller designed by Dr. Jan Südbeck, which allows to set the temperature in three crystal regions separately as well as to apply temperature ramps to the different crystal regions.

3.2.3. Phase-matching temperature and temperature gradient

The PPKTP crystal is quasi-phasematched to operate as type-0 SHG. For given fundamental and harmonic wavelengths, the phase matching is realized by adjusting the domain length Λ, such that it satisfies the phase-matching condition (see section 2.8). For the crystals used in the experiment, the domain length is $3.25\,\mu\mathrm{m}$. This domain length originates from the demand to obtain quasi-phasematching for conversion from $799\,\mathrm{nm}$ to $399.5\,\mathrm{nm}$ slightly above room temperature at $23\,^{\circ}\mathrm{C}$.

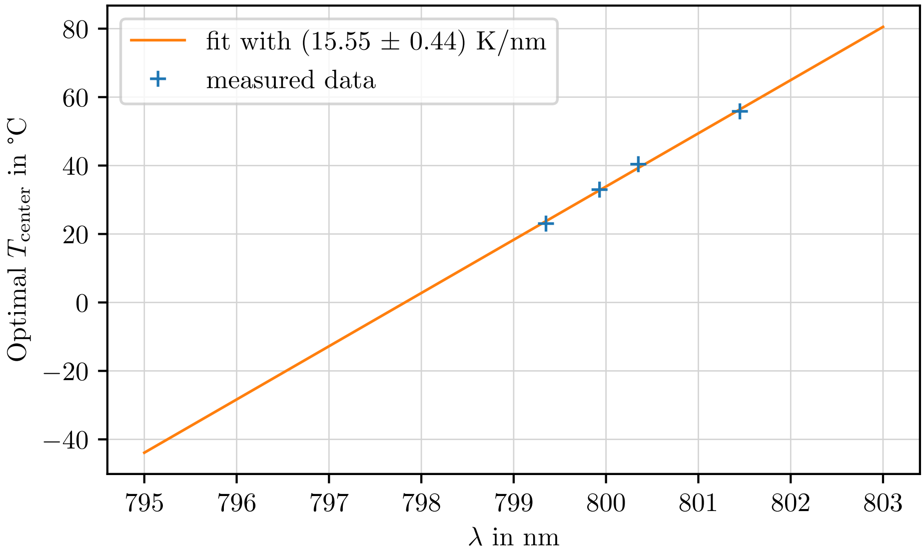

Figure 3.5.: Phase-matching temperature versus laser wavelength.

The wavelength of optimal conversion efficiency can be modified by choosing an appropriate crystal temperature. To calculate this, both the thermal expansion and the thermo-induced change in the refractive index need to be taken into account. A Python package by Maik Schröder allowed to calculate the dependence between crystal temperature and wavelength of optimal phase matching. The results show a gradient of around 17 K/nm. This value could, in good approximation, be verified in the experiment, as shown in figure 3.5: Four different wavelengths (ranging between 799 – 801.5 nm) were set for the laser. The wavelength was measured by a Bruker Equinox 55 spectrometer. Around this center wavelength, the laser frequency was ramped such that three to four resonance peaks could be detected on the oscilloscope. Only the center Peltier element was powered; its temperature was adjusted to find optimal conversion for the resonance peak in the center of the frequency ramp. The crystal temperature was calculated from the NTC voltage of the Peltier element. Fitting the measurements yields a gradient of (15.55 ± 0.44) K/nm, which is in reasonable agreement with 17 K/nm from the simulation by Maik Schröder. At 800 nm, this gradient corresponds to 30.0 GHz/K.

At operation below room temperature, water vapor may condense on the crystal's surfaces, which will lead to substantial absorption and beam distortion. Therefore, operation below 799 nm should be avoided. The Peltier elements allow to heat the crystal to about 65 °C, which means approximately 45 °C above design temperature. With 15.55 K/nm, this corresponds to a shift of 2.9 nm, yielding a maximal wavelength of operation of around 801.9 nm.

For most time of the experiment, the laser wavelength was set to 800.43 nm. For this wavelength, the optimal temperatures for phase matching range between 35 – 39 °C (see section

3.8.2). In this temperature range, the crystal can both be heated and cooled reasonably fast. In the initial measurements on the SHG cavity, the system was operated closer to the design temperature at 799.35 nm. Here, the optimal phase-matching temperature was in the range between 23.5 °C and 25 °C. These parameters are in good agreement with other SHG experiments in the same wavelength range (see, for example, [Wan+17]).

3.2.4. Crystal sections and degrees of freedom

The monolithic design as depicted in figure 3.3a comes at the cost of limited degrees of freedom; in fact, only the crystal temperature can conveniently be adjusted. However, due to the divergence of the cavity mode, one can distinguish three regions in the crystal, which will react in different ways to a change in temperature and can therefore be adjusted independently from each other. Due to the focusing of the beam, the intensity in the center of the crystal is approximately twice the intensity at the crystal's end facets. Since the conversion scales with the intensity squared (see eq. (2.62)), the proper phase matching is more important in the center of the crystal than on its edges. Consequently, the end regions can be used to tune the overall cavity length while keeping the phase-matching temperature in the center constant. Since the SHG cavity is only resonant for the pump wavelength, it suffices to power one of the edge temperatures for cavity length adjustment while the other edge section is not powered but thermalizes to the center temperature of optimal phase matching. In principle, heating the center temperature while reducing the edge temperature (and vice versa) allows to adjust the phase-matching temperature while keeping the cavity's resonance frequency constant; however, best frequency conversion efficiencies have only been obtained when all temperature sections were set to the same value. The following sections will discuss in which ways these temperatures are coupled and how the experimentally relevant quantities are affected by them.

3.2.5. Temperature distribution inside the crystal

To quantify the heat distribution inside the crystal, the system was simulated using the finite-element-modeling software COMSOL Multiphysics. The software allows to model complex physical systems and solve the corresponding set of coupled differential equations numerically. For the analysis in this thesis, the heat transfer module was used. The PPKTP crystal was modeled with its original dimensions and material properties. The following set of boundary conditions were defined for the simulation: Center temperature and edge temperature can be set to well defined values (since they are placed on heat conducting metal surfaces that are powered by Peltier elements). The non-powered edge element is modeled as an open boundary, since it is connected to a well-conducting but non-powered element that will thermalize with the crystal temperature. The ambient temperature is room temperature (20 °C). An outward heat flux is modeled by heat convexion on all sides and on top of the crystal. The

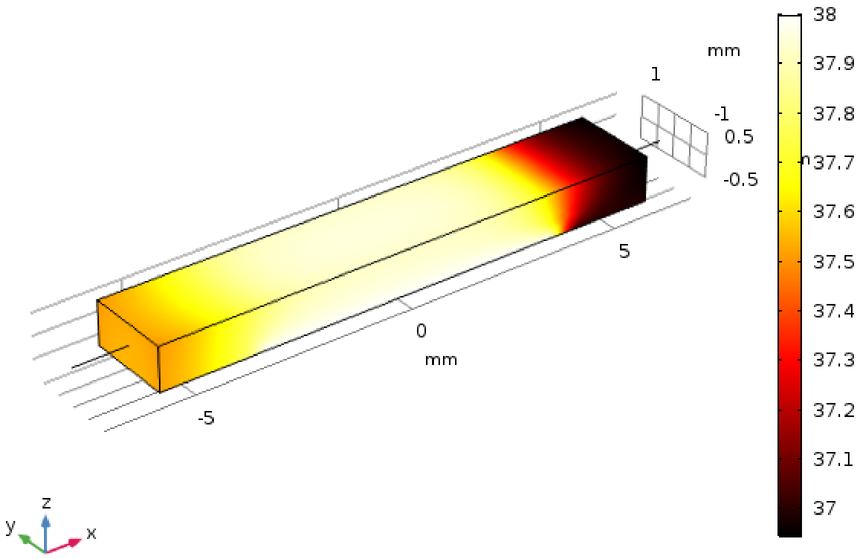

Figure 3.6.: Temperature distribution in °C in the crystal (COMSOL simulation). The center temperature is powered to 38 °C while the right edge temperature is held at 37 °C. The simulation shows that the edge temperature is homogeneous within one millimeter from the edge of the crystal. Then, at the beam height, there is a transition zone of approximately another millimeter before the temperature stays homogeneous over the center temperature region.

CAD model does not contain the plastic yoke, that would in the experiment be placed on top of the crystal. However, it is assumed that the yoke does not significantly impact heat flux and temperature distribution within the crystal. In a preliminary study, heat transfer due to radiation was found to be negligible at temperatures close to room temperature and was therefore not modeled in the presented simulation.

Figure 3.6 shows the simulated temperature distribution inside the crystal. From the simulation, it can be verified that center and edge temperatures act on well separated sections of the crystal: while the major part of the crystal is heated in good approximation homogeneously to the center temperature, the edge region of the crystal (approx. 1 mm) maintains the edge's set temperature. Along the beam path in the center of the crystal, there is about 1 mm of temperature gradient, continuously matching center and edge temperature to each other. This simulation shows that both temperatures can be actuated well separated from each other. However, highest conversion efficiency is reached when the quasi-phasematching condition is satisfied over the whole crystal, which requires that edge and center temperatures are equal.

In a second step, the thermalization when a laser is locked to the cavity was studied. From a steady state solution with both center and edge temperature set to the same value, a line of heat deposition was modeled in the center of the crystal, just where the laser beam would be situated. The line heat deposition aims to model the losses of blue light, that is produced

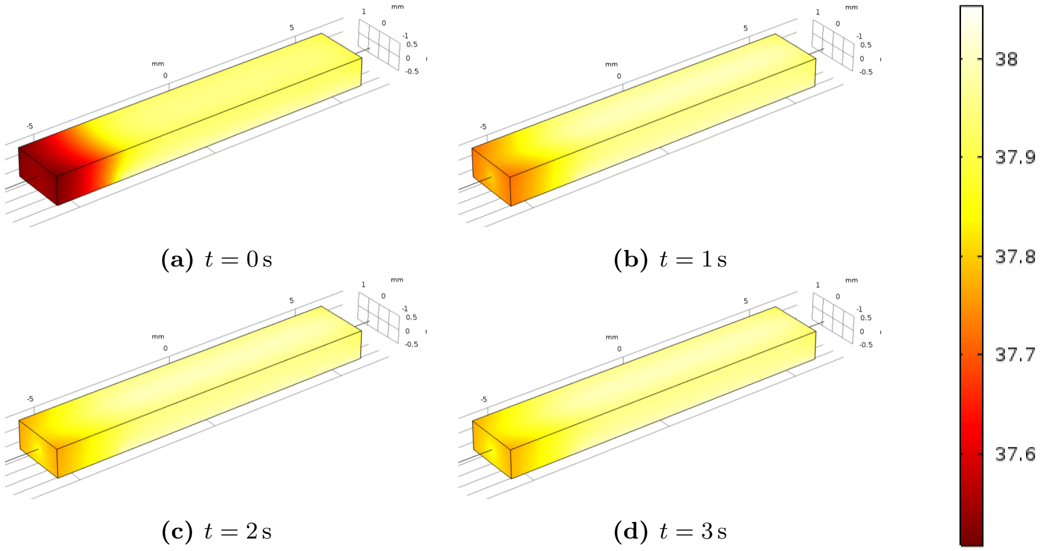

(a) $t = 0\,\mathrm{s}$ **(b)** $t = 1\,\mathrm{s}$

(c) $t = 2\,\mathrm{s}$ **(d)** $t = 3\,\mathrm{s}$

Figure 3.7.: COMSOL simulation of the heat transfer inside the crystal when a laser is switched on. The heat deposition is modeled with 18 mW/cm. The center and one edge temperature are powered with 38 °C while the surrounding is at room temperature. The laser is switched on at $t = 0\,\mathrm{s}$. The new equilibrium temperature is reached after few seconds of thermalization.

inside the cavity. With typical losses of 21 mW over the crystal length of $L = 11.56\,\mathrm{mm}$, the heat deposition is modeled with 1.8 W/m. A time-dependent solver models the heat distribution in the crystal over time after the heat source is switched on at $t = 0\,\mathrm{s}$. From figures 3.7, one can see that the crystal thermalizes on timescales of $2 - 4\,\mathrm{s}$, which is in agreement with the thermalization time scales observed in the experiment (see figure 3.17 in section 3.7.4 for the corresponding experimental data).

3.2.6. Feedback effects due to absorption inside the crystal

In the absence of optical losses, there are no back-action effects in the monolithic design. However, for conversion from 800 nm to 400 nm, the absorption coefficient of PPKTP at 400 nm leads to significant thermal feedback effects once converted light is present inside the crystal. Light that is absorbed inside the crystal leads to a temperature rise along the beam path as discussed in section 3.2.5. This gives rise to two effects that mutually influence each other and thereby add complexity to the system.

First of all, a rise in temperature increases the optical path length in the cavity due to the temperature-dependence of the refractive index and the thermal expansion of the crystal – this reduces the cavity's resonance frequency. This effect occurs whenever 400 nm light is present in the cavity, which means that, for example, when the cavity is resonant with the input laser beam and the phase-matching condition is satisfied, the heating due to the newly generated 400 nm light may push the cavity off resonance.

Secondly, the refractive index and the domain length impact directly on the phase-matching condition. With rising temperatures, the phase-matching condition is satisfied at longer wavelengths (or lower frequencies, respectively), as shown in section 3.2.3; this also holds for small temperature drifts. Consequently, the heating due to the generated light can shift the gain profile, such that the phase-matching condition is no longer satisfied and the output power is significantly reduced – even if the cavity remains resonant with the input beam throughout.

Additional complexity is added in the monolithic design, since, here, the two processes are inevitably coupled to each other: The converted output power depends on the gain profile, evaluated at the cavity's resonance frequency at a certain moment of time. Since both the resonance frequency and the gain profile move with increasing temperature, and the amount that they move is determined by their previous positions, a non-trivial set of differential equations would be required to describe the dynamics of the system; however, this approach was not further pursued within this thesis. Nevertheless, the qualitative argument is very useful to interpret the measurement data and make qualitative predictions on how the system will behave in specific scenarios (see section 3.7). These coupled back-action effects are a key signature of a monolithic cavity design operating close to the end of the opacity range.

3.3. Pump laser

The light source in the experiment is a Toptica TA pro laser head, whose wavelength can be tuned in a range between 795 nm and 803 nm. The tapered amplifier allows for output powers up to 1.0 W. However, the mode shape after the TA chip is by far not Gaussian, and a polarization maintaining fiber is used to clean the optical mode. After the fiber, the light is split for different parts of the experiment. Up to 200 mW can be used to pump the SHG cavity, while additional 500 mW serve as control beam and local oscillator.

The TA pro laser is an external cavity diode laser (ECDL), in which a cavity is formed between the laser diode and a Bragg grating, that is placed on a piezoelectric actuator. The laser frequency can be coarse-tuned by adjusting the angle of the grating. A change in grating angle also slightly changes the output mode, which requires a re-adjustment of the beam position and angle for the TA chip. For smaller and faster frequency changes, the grating position can be adjusted by the piezo actuator. In this way, a frequency offset of up to 25 GHz can be applied to fine-tune the laser frequency, which covers up to four resonances (and three free spectral ranges (FSRs)) of the SHG cavity. The laser frequency can be ramped in this frequency range at a ramping frequency of up to 500 Hz; usually ramping frequencies of 25 Hz were used for the measurements. A fast frequency ramp allows to probe the spectroscopic response of the cavity over a broad frequency range and monitor changes in the cavity resonance instantaneously. Furthermore, the limited thermalization time on resonance allows to study the system outside thermal equilibrium.

Even faster adjustments of the laser frequency (although at lower amplitude) are possible by modulating the current of the master laser diode. To maintain mode-hop free operation over the whole traveling range of the piezoelectric actuator of more than 30 GHz, a feed-forward is applied, that adjusts the master current proportional to the applied piezo voltage. The master current can also be modulated to produce the error signal for the laser's built-in locking feature: for the SHG cavity, the reflected power is monitored on a self-built monitor photodiode and demodulated with the laser's modulation frequency. The resulting error signal allows the laser's piezo actuator to follow the cavity's resonance frequency up to the end of its traveling range. The piezo voltage can be read out and (after calibration with e.g., two cavity resonances with known free spectral range between them) translated into an offset of the laser frequency.

The master laser supplies a power of some tens of milliwatts, that are amplified by a tapered amplifier (TA) chip. The amplification depends on the amplifier current, which does not impact on the laser frequency. The output beam from the TA is neither Gaussian nor elliptical, but heavily distorted. Therefore, it is mode-cleaned by a polarization maintaining optical fiber. Due to the distorted mode, the optimal coupling efficiency to the fiber was around 70 %. The amplifier current can be used to compensate for power fluctuations by monitoring the output power on a photo diode and sending a feedback signal to the amplifier.

3.4. Impact of center and edge temperature on gain curves and resonance shift

In section 3.2.5, it was shown theoretically that center and edge temperatures act on different parts of the crystal; they therefore impact on the cavity's resonance frequency in different ways. Figure 3.8 illustrates this with experimental data: the laser frequency was ramped at 10 mW input power and the transmitted output light from the SHG cavity at 800 nm was monitored by a photodiode. Higher ramp voltage applied to the piezo actuator corresponds to higher laser frequency offset, i.e., figure 3.8 shows a rising laser frequency ramp. The traces show equally spaced cavity resonances, which indicates that close to 100 % of the pump light are coupled into the TEM_{00} mode of the SHG cavity. An initial trace was recorded with both crystal sections set to the same temperature $T_{\mathrm{center}} = T_{\mathrm{edge}} = 36.24\,^{\circ}\mathrm{C}$ (blue). From this, the temperatures were lowered by 1.83 °C in both crystal sections separately (red for T_{center} and green for T_{edge}), and for each case, a trace of the shifted mode spectrum was recorded after reaching thermal equilibrium. Since the center temperature acts on a bigger part of the crystal, the same temperature reduction in the center temperature leads to a further shift of the resonance frequency (exceeding one FSR) than the same reduction in the edge temperature. For comparison, the yellow trace was recorded, where the center temperature was lowered by only 0.46 °C; this led approximately to the same shift as reducing the edge temperature by 1.83 °C.

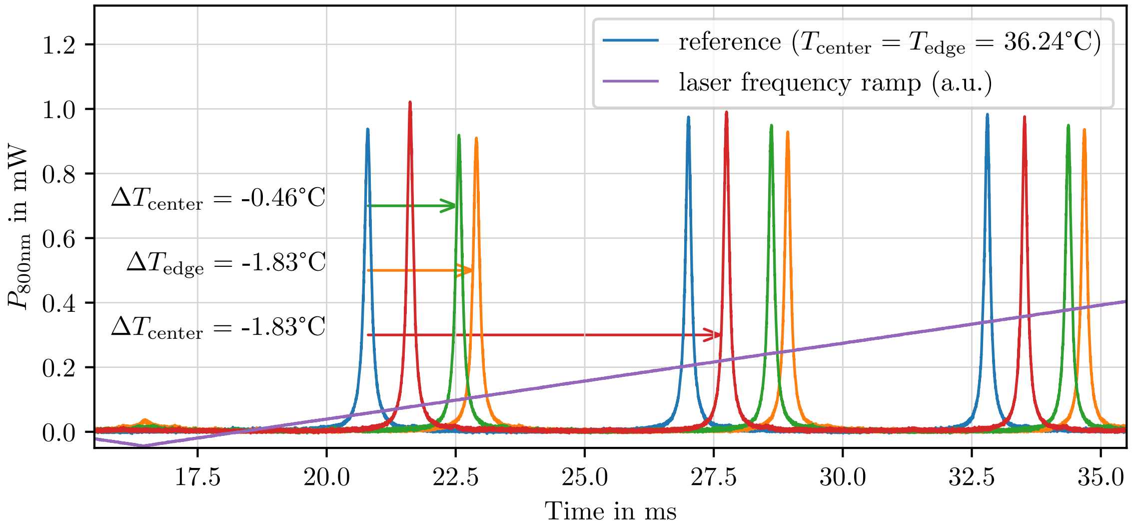

Figure 3.8.: Resonance frequency drift due to a change in center temperature and edge temperature. Reducing the temperature of the crystal shifts the cavity's resonances to higher frequencies (to the right). Reduction of the center temperature by 0.46 °C (green) has a similar effect like reducing the edge temperature by 1.83 °C (orange). A reduction of the center temperature by 1.83 K (red) shifts the resonance by more than one FSR.

To quantify the drift of the resonance frequencies due to changes of the crystal temperatures with a second method, the crystal temperature was tuned and the shift of the resonances was observed. One specific frequency is chosen, and as the crystal is heated, it is observed at which temperatures other cavity resonances pass the chosen frequency. While tuning the center temperature from 25.0 °C to 31.65 °C, the mode spectrum is shifted by 6 FSRs of 7.034 GHz each, thus 42.2 GHz in total. This corresponds to a gradient of 6.35 GHz/K, or, in other words, a shift of 1 FSR per 1.11 K increment in phase-matching temperature. For this measurement, only the center temperature was powered.

In a similar way, the drift was quantified when both center temperature and edge temperature were powered. With the edge temperature at a constant 36.2 °C, close to the optimal phase-matching temperature, a temperature increase from 31.9 °C to 41.5 °C led to a shift of six FSRs. This results in an averaged frequency shift of 4.4 GHz/K, corresponding to 1.6 K per FSR, in reasonable agreement with the measurement presented in figure 3.8. For comparison, when the center temperature is kept at a constant 35.8 °C, a temperature increment of T_{edge} from 32.6 °C to 38.1 °C shifts the resonance frequencies by one FSR, thus 1.28 GHz/K. This means that the center temperature shifts the cavity's resonance frequency almost 3.5 times as much as the edge temperature. Both gradients are smaller than for the case when only the center temperature was powered, since center and edge temperature act against each other when they are simultaneously heated and set to different temperatures.

3.5. Output power and conversion efficiency

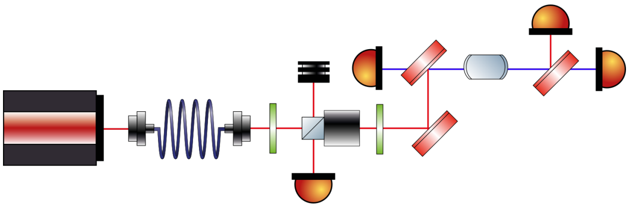

Figure 3.9.: Experimental setup for the conversion efficiency measurement of SHG. A polarization-maintaining fiber is used to clean the mode of the Toptica TApro laser head. A $\lambda/2$-waveplate and a polarizing beam splitter cube allow to adjust the input power. With a Faraday rotator, the incoming and reflected beams at 800 nm can be separated. Dichroic beam splitters separate the outgoing 400 nm and 800 nm powers in both output ports, which are monitored by separate photodiodes. Component icons by [Fra].

The SHG output is intended to be used as the pump for the nonlinear squeezing process; this requires sufficient and stable output power. Up to the OPO threshold, an increase in pump power leads to increased squeezing. Therefore, the achievable output power from the SHG process is a relevant characteristic quantity. Apart from the output power in transmission P_{trans} (which can directly be used to pump the OPO), also the total output power $P_{\text{tot}} = P_{\text{trans}} + P_{\text{refl}}$ (i.e. the sum of output power in both ports) can be a quantity of interest, for example, to determine the total conversion efficiency that can be obtained in the SHG process. The corresponding conversion efficiencies are obtained by dividing the output powers by the input power P_{in}. The external conversion efficiency in transmission is defined by $\eta_{\text{trans}} = \frac{P_{\text{trans}}}{P_{\text{in}}}$, while the total conversion efficiency is denoted by $\eta_{\text{tot}} = \frac{P_{\text{tot}}}{P_{\text{in}}}$.

Figure 3.9 shows the schematic setup for the characterization and conversion efficiency measurement of the SHG. The laser mode is cleaned in an optical fiber. Power can be adjusted via a combination of $\lambda/2$-waveplate and a polarizing beam splitter (PBS). Dichroic mirrors prior and after the SHG cavity allow to monitor all light exiting the SHG cavity, both in transmission and reflection separately. To separate the input and reflected 800 nm beam paths, a Faraday rotator adds on each of the two passes an additional 45° rotation to the polarization, such that after reflection from the SHG cavity, the light is reflected off the PBS onto a photodiode. Its signal can then be used both for locking the laser to the SHG cavity and to monitor the reflected 800 nm-power.

For stable operation at optimized output powers, the laser is locked to the SHG cavity. In this case, both crystal temperature sections can be used to adjust the temperature gradient inside the cavity to yield highest output power, and the thermally induced changes in the cavity's resonance frequency are automatically followed by the laser. In general, highest conversion efficiency was reached when $T_{\text{center}} = T_{\text{edge}}$, and therefore, for this measurement, only the center temperature was powered. When the laser is locked, the cavity heats up

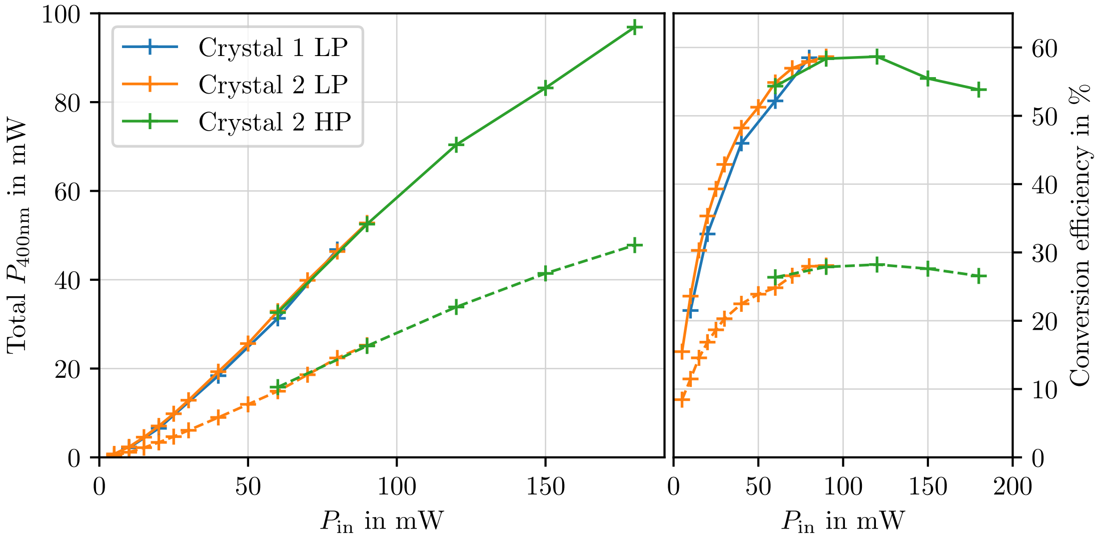

Figure 3.10.: SHG output power (left) and conversion efficiency (right) versus pump power for two fresh SHG crystals (LP = low power, HP = high power). Solid lines: Total output from both output ports. Dashed lines: Output in transmission port only.

and both laser frequency and gain profile drift (see sections 3.7.4 and 3.8.3); for this reason, several neighboring resonances need to be checked to find the best combination of resonance frequency and gain after thermalization. Due to the limited traveling range of the piezo actuator, for input powers $\geq 100\,\mathrm{mW}$, a two-step locking procedure turned out to be useful: the laser was then locked to some cavity resonance for about 5 seconds, during which the crystal heats up and the resonance frequencies shift to lower frequencies. The laser was then unlocked and directly locked again to another mode of higher frequency, that had in the meantime been shifted into the frequency window covered by the laser's piezo. In this way, new combinations of crystal temperature and frequency could be reached. This procedure turned out crucial to obtain high output powers from the SHG cavity.

The generated 400 nm output powers and corresponding conversion efficiencies are shown in figure 3.10 for two different SHG crystals from the same lot. The conversion efficiencies below 100 mW were measured on both crystals and are in excellent agreement. The optimal total conversion efficiency peaked at around 58.6 % for 120 mW input power. The output power is evenly split between both output ports of the cavity; the dashed line shows the output power and conversion efficiency in transmission. The total conversion is in good agreement with the optimal SHG conversion efficiencies from 795 nm to 397.5 nm in PPKTP reported in [Han+16] .

3.6. Intracavity losses at 400 nm

The setup from figure 3.9 allows to monitor all output powers, and the initial light power can be determined with a power meter. Thus, a loss analysis can be performed for varying input power by subtracting all output powers from the input power; the missing energy must have been absorbed inside the crystal or on the optical elements along the beam path. This was one of the first measurements performed on the SHG cavity.

Top left of figure 3.11 plots the total losses against the input power at 800 nm. It can be seen that, especially at low input powers, the losses increase disproportionally high with input power. If the losses would arise from absorption of 800 nm light, one would expect a linear increment with increasing pump power. This means that other absorption mechanisms are responsible for most of the observed losses.

Due to the high absorption coefficient of 18.9 %/cm at 400 nm [Yan+15], it is expected that in the presence of converted light, this will be the main loss channel; this can be observed in top right of figure 3.11, where the same losses as before are plotted versus the total blue light power that exits the system through either the transmission or reflection port. In this representation, the data can well be fitted by a linear function through the origin, which suggests that the losses mainly originate from the absorption of the 400 nm light.

The bottom right of figure 3.11 divides the losses by the blue output power. For blue output powers above 10 mW, almost independent of the input power, an additional portion of 50%

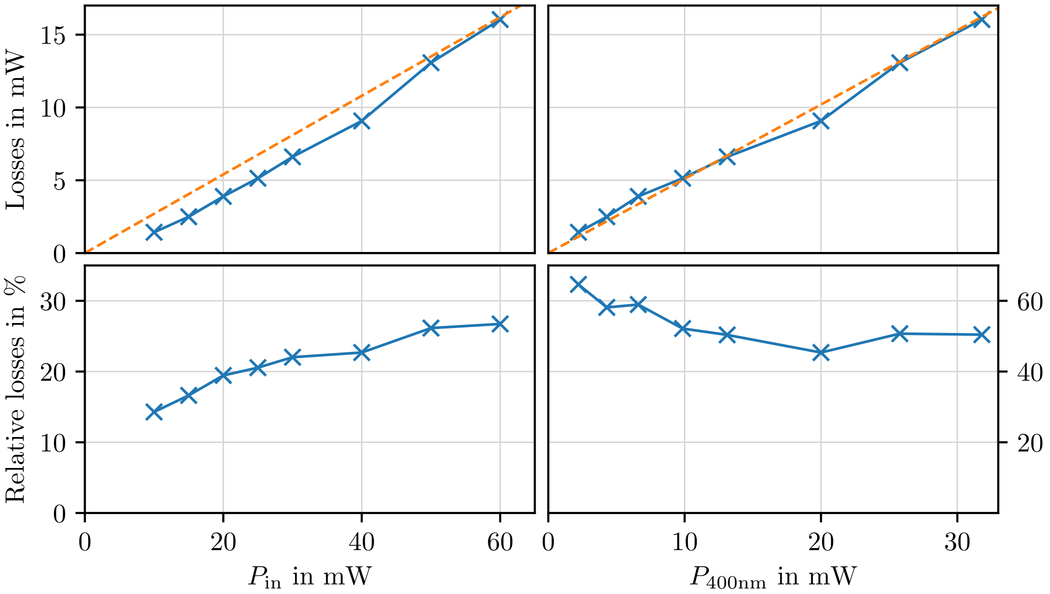

Figure 3.11.: Loss analysis on a fresh crystal. Top: Losses versus 800 nm input power (left) and losses versus total 400 nm output power (right). Bottom: Relative Losses per input power (left) and per total 400 nm output power (right).

of the output 400 nm light is absorbed inside the crystal before it can escape; it is therefore not detected by any photodiode. The increased losses at output powers below 10 mW can be attributed to residual absorption at 800 nm, which makes a significant (but not dominant) contribution when barely any light is converted and thus mainly the pump light is present in the system. For higher output power, this loss channel becomes negligible. This observation seems plausible when comparing the absorption coefficient $\alpha = 18.9\,\%/\mathrm{cm}$ at 400 nm with $\alpha = 0.015\,\%/\mathrm{cm}$ at 800 nm [Ste+13].

With this assumption, one can estimate an upper limit to the internal conversion efficiency

$$\eta_{\mathrm{int}} = \frac{P_{\mathrm{tot}} + P_{\mathrm{loss}}}{P_{\mathrm{in}}}, \tag{3.2}$$

taking also the converted light into account that gets absorbed before it can exit the cavity. This is shown in figure 3.12: for 60 mW input power, in addition to the 53% external conversion efficiency, 26.5% of the input light are converted to 400 nm but are absorbed before leaving the crystal. Accounting for this absorption leads to an internal conversion efficiency of $\eta_{\mathrm{int}} = 79.5\,\%$ inside the crystal, which shows that the system is operated not too far from the optimally achievable conversion efficiency. In other words, even an internal conversion efficiency of 100% would lead at maximum to 66% of external conversion efficiency. Comparing this with the measurement in figure 3.10, one can see that the SHG was operated not far from optimal conversion efficiency.

Another consistency check for this hypothesis can be performed by recording the red and blue output powers in both directions and subtracting them from the input power. If the resulting losses are completely attributed to absorption of blue light, one gets an upper limit of the internal conversion efficiency. The result is shown as the orange curve in figure 3.12.

It needs to be noted at this point that the measurements presented in this section were performed on a fresh crystal. When the measurement from figure 3.11 was performed again a few days later, the losses were no longer proportional to total blue power, but the losses of the 800 nm pump light seem to have increased significantly, opening a second loss channel. This was a first experimental sign of photochromic damage of the crystal, so-called gray tracking, which occurs when near-UV light is absorbed and damages the crystal, thereby increasing the absorption over the whole visible range [Bou+99]. Already small additional absorption at the fundamental wavelength can have significant effects, since it significantly reduces the finesse of the cavity and consequently also the intracavity power. The degradation and its effect on the output power will be investigated further in section 3.9.

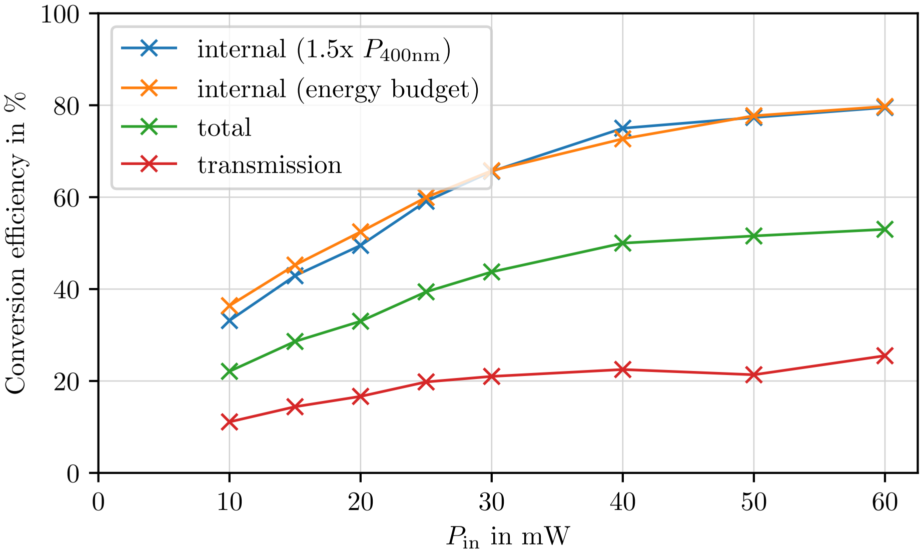

Figure 3.12.: Conversion efficiency versus input power. For this measurement, the crystal temperatures were optimized for highest total output power. Plotted are the conversion efficiency in transmission η_{trans} (red), the summed conversion efficiency from both output ports η_{tot} (green) and two estimations for the internal conversion efficiency η_{int}: The blue curve corrects for the 33% of the generated 400 nm-light that get absorbed inside the crystal by multiplying the green curve η_{tot} with 1.5. The orange curve estimates the total conversion efficiency from the energy budget by attributing all losses to absorbed 400 nm light. It is calculated by subtracting the residual 800 nm output powers from the input power.

3.7. Thermal effects

A characteristic property of the monolithic cavity design, operated at wavelengths with substantial absorption in the cavity, are thermal feedback effects. This section studies asymmetries in temperature and laser frequency ramps as well as the drift of the resonance frequency when the laser is locked to the cavity. It furthermore demonstrates why it is not trivial to find the combination of laser frequency and gain temperature that yields the highest output power after thermalization.

3.7.1. Temperature ramp with free floating laser

The laser can be operated free-running without active adjustments or modulations of the laser frequency, and the cavity's resonance frequency can be ramped over the laser frequency by rising and lowering the crystal temperature. The crystal temperature is controlled by a negative temperature coefficient thermistor (NTC), whose set voltages were entered into a LabVIEWview script and transmitted to the temperature controller via a Keysight 33511B waveform generator. The photodiode voltages for the transmitted 800 nm light were acquired with a Keysight FS-3004 oscilloscope and saved on the computer.

Figure 3.13 shows the transmitted 800 nm light for input powers between 1 – 30 mW for rising (solid) and falling temperature ramp (dashed). The measurement was performed on a fresh crystal at temperatures far from the phase-matching condition, such that no 400 nm light was produced. Data points were recorded in steps of 618 ms, which is the fastest acquisition speed that the data readout allowed; during this time, the temperature changed by 0.0046 K (corresponding to an increment of 0.1 mV in set voltage). Due to the heat propagation in the crystal, the resonances on rising and falling ramp did not appear for the same NTC set temperature; this effect was corrected by a applying an offset to all decreasing temperature traces. Additional offsets were added to the individual traces to account for small laser frequency drifts between the measurements.

The measurement shows a strong asymmetry depending on the ramp direction, that is already visible for input powers as low as 2 mW and becomes more and more severe with increasing input power. When the temperature increases, the optical path length of the cavity expands and the cavity's resonance frequency decreases. When the cavity approaches the laser frequency, the light can enter the cavity. Consequently, the intracavity losses accelerate the heating and pull the cavity's resonance frequency towards the laser frequency; for higher input powers, this shift may be so strong that the cavity gets pulled over the laser frequency, as can be seen by the spikes in the traces for 20 mW and 30 mW. It must be noted that this effect originates only from the 0.012 – 0.1 %/cm absorption of a fresh crystal at 800 nm; at the phase-matching temperature, already fractions of milliwatts of the generated 400 nm light suffice to pull the cavity through resonance due to the higher absorption at this wavelength.

On the contrary, when the temperature is lowered, the cavity length reduces and the resonance frequency increases towards the laser frequency. When approaching resonance, the absorption starts to heat the crystal, which counteracts the external temperature reduction. In this way, the external temperature can be lowered without changing the cavity's resonance frequency proportionally. Closer to resonance, the intracavity power and consequently also the absorption losses increase and contribute more to the heat budget. The temperature can be lowered until the reduction in temperature is smaller than the increase in temperature due to absorption of the increased intracavity power (or harmonic output power, if the system is operated at the phase-matching temperature). Beyond this temperature, the conversion breaks down immediately and the cavity's resonance frequency jumps instantly to the frequency given by the external set temperature (see left side of figure 3.13). Up until this point, stable operation at high output powers is possible, however always under the risk of accidentally losing resonance.

The described thermal effects do not only arise in the SHG cavity, but also in the OPO, where 400 nm light is used as the pump light to generate squeezing. Since the frequency of the pump light is defined by the SHG cavity, that scenario can be considered as a fixed laser

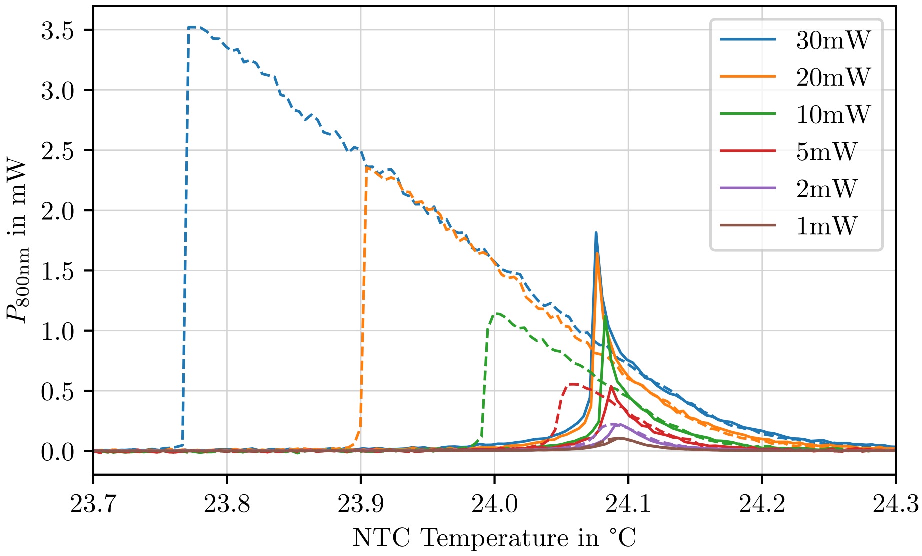

Figure 3.13.: Temperature ramps for free floating laser frequency at various input powers. Solid (dashed) lines correspond to increasing (decreasing) temperatures. Offsets were added to the NTC temperature to account for drifts of the laser frequency between measurements and hysteresis effects between rising and falling ramp (see text).

frequency, to which the OPO needs to be brought to resonance by tuning the temperature. When optimizing the system, it was a challenge to improve performance without crossing the points at which the conversion breaks down and resonance is lost. Once this happens, the point of stable operation can only be reached again by crossing the resonance and then decreasing the temperature towards the point of optimal operation again. For more details, see section 4.5.

Temperature locking To ensure resonance of the laser with a given laser frequency, temperature locking schemes were considered. However, figure 3.13 illustrates the difficulties that would arise when the cavity's resonance frequency is locked via the crystal temperature. First of all, the point of highest output power is not stable and consequently a top of fringe temperature lock to the optimum output power is not possible. Locking to the side of the fringe (i.e., to a fixed output power) seems in principle possible for a fixed laser frequency when the operational point is approached by lowering the temperature; the output power or intracavity power could then be compared to some set point, and the difference can be fed back to the Peltier driver. This could then cool or heat the cavity to push the cavity resonance towards or away from the laser frequency. Since the thermalization happens on time scales of $0.5 - 1\,\mathrm{s}$, the bandwidth of such a lock would be of the order of $1\,\mathrm{Hz}$. It seems that operation at a constant laser frequency would, in principle, be possible as long as the pump powers and ambient temperatures do not change over time.

Nevertheless, the above reasoning also shows the limitations when the laser frequency is given by an external frequency reference (e.g., some external optical cavity with time-dependent resonance frequency). In this case, fluctuations and drifts of the laser frequency have to be negligible compared to the cavity linewidth (136 MHz) to avoid that the cavity becomes resonant with a random fluctuation of the laser frequency and is then pushed out of its metastable state. Drifts, on the other hand, need to be sufficiently slow, such that they can be followed by a temperature side of fringe lock, i.e., slower than the timescales of thermalization of the crystal.

3.7.2. Laser frequency ramp

Instead of ramping the crystal temperature, also the laser frequency can be ramped over a cavity resonance for a given crystal set temperature; this can be performed much faster than the temperature ramp of the preceding section. As long as the phase-matching is detuned and no significant conversion occurs in the crystal, the line shape of the resonance is symmetric and independent of the ramp direction. However, as soon as the phase-matching condition is satisfied, one can observe that the resonance line becomes distorted, depending on the ramp direction and input power, as shown in figure 3.14: for rising laser frequency, the linewidths seems to become narrower, while the line broadens when the resonance is crossed by a decreasing laser frequency. The distortion and asymmetry increase with input power and duration of the ramp cycle and are clearly visible already for input powers as low as 20 mW and ramp frequencies as fast as 25 Hz.

The described effect originates from thermal expansion and the temperature-dependent refractive index of the crystal: When reaching resonance, significant amounts of light are converted from 800 nm to 400 nm. The latter is partially absorbed in the crystal, which leads to heating and consequently thermal expansion and increasing refractive index. The increase of optical path length inside the cavity shifts the resonance frequency to lower values. Consequently, on the falling ramp, the thermal expansion moves the cavity's resonance frequency in the same direction as the laser frequency, and resonance is maintained for a longer time. On the contrary, on the rising ramp, the laser frequency increases while the cavity's resonance frequency decreases once the laser becomes resonant with the cavity. The thermal expansion therefore pushes the cavity off resonance, in this case, and the resonance line seems narrowed.

In figure 3.14, this effect was systematically studied for varying ramping speed and input power. The traces are plotted versus laser frequency offset, which was obtained from the piezo voltage by calibration with several neighboring resonances, for which the FSR of 7.034 GHz is known. Since the transfer function of the piezo actuator is not perfectly linear, this introduces a systematic error of 5 − 8 % to the value of the laser frequency offset. The raw data was furthermore subject to a hysteresis of the piezo actuator, since, even for small powers of

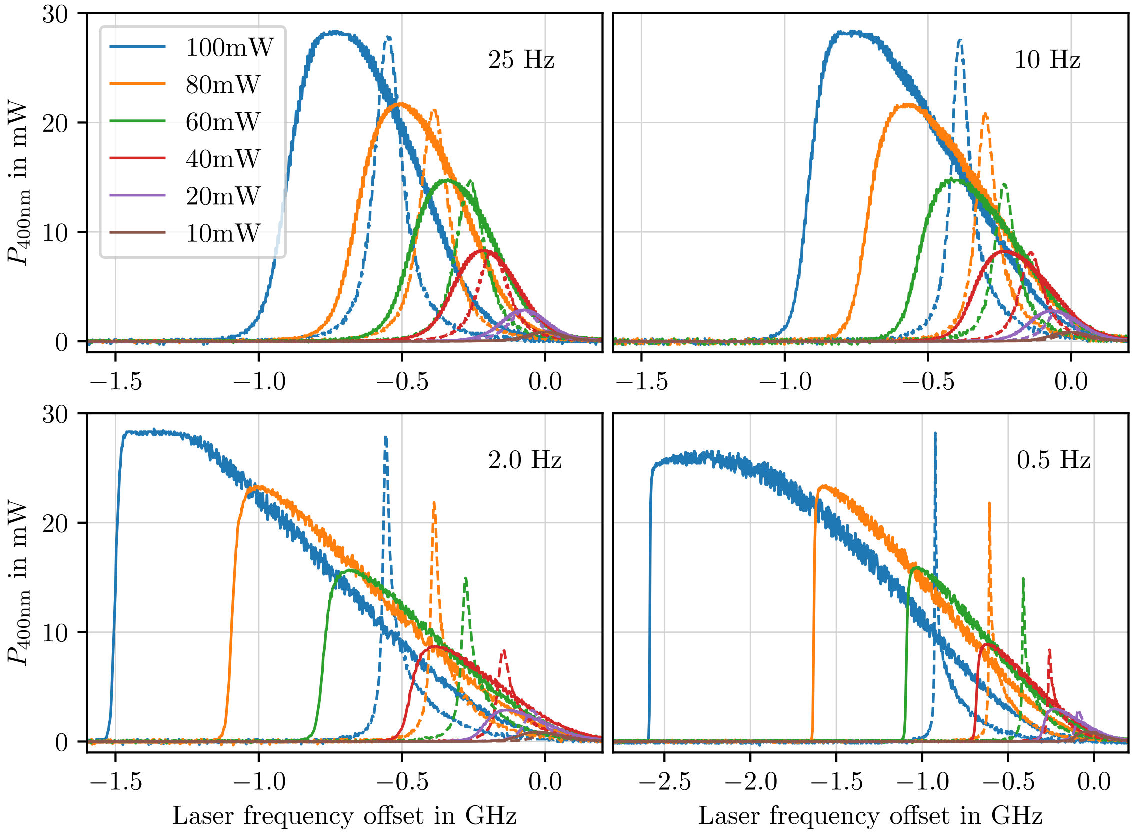

Figure 3.14.: SHG cavity resonance line distortion due to thermal expansion. For different ramping frequencies and input powers, the output power at 400 nm in transmission is monitored versus the laser frequency offset. Solid lines depict the spectroscopic response on falling frequency ramp (recorded from right to left) while dashed lines show the response on the rising ramp. The frequency offset is normed to the resonance frequency at 10 mW for each ramping speed. The plot for 0.5 Hz ramp frequency was extended to show the 2.6 GHz drift of the resonance frequency on falling ramp.

10 mW (where no significant thermal effects are expected or observed), the resonance lines on rising and falling ramp did not appear at the same piezo voltage. This offset was subtracted for all traces of the same ramping speed and input power.

The measurement presented in figure 3.14 was taken in 4 blocks (one for each ramping speed). Between the blocks, the resonance frequency at 10 mW input power varied by up to 330 MHz (corresponding to approximately 2.4 linewidths of the SHG cavity). This can be explained well by slight temperature drifts in the laboratory, which cause the resonance frequency to change over time. For better comparison between different ramping speeds, the traces of each block were normed to the resonance frequency at 10 mW.

Figure 3.14 shows the transmitted 400 nm output power when the laser frequency is ramped, after the before-mentioned corrections. The solid line shows the cavity resonance on falling ramp (laser frequency decreasing, recorded from right to left) while the dashed lines show the corresponding signal half a ramping cycle later on rising ramp (recorded from left to right). From the top left graph in figure 3.14, it can be seen that the resonance frequencies drift to lower frequencies with increasing input power, both on rising and falling ramp. This can be explained by the heat deposition inside the crystal. Although the ramp covers more than one FSR and, therefore, the cavity is only resonant for a small fraction of the time, the generation and absorption of blue light on resonance suffices to increase the average temperature of the crystal. The peak output power appears to be independent of the ramp direction.

With 25 Hz ramp frequency, the systems seems to be too fast to cool down before the next resonance is probed and heats the crystal again. This is in contrast to the measurements at 10 Hz (top right of fig. 3.14): while the resonances on falling ramps have similar shapes and frequency displacements as for 25 Hz, the rising ramp resonance lines appear less shifted. An explanation is that there is more time between the resonance on falling ramp (where most of the heat is applied to the crystal) and the rising ramp's resonance. The additional fraction of a second between two heatings allows the heat to dissipate away from the optical axis into the crystal. This explains why, for example, for 100 mW input power, the frequency on rising ramp gets shifted by 0.4 GHz rather than 0.6 GHz when the ramping frequency is reduced from 25 Hz to 10 Hz.

At lower ramping speeds of 2 Hz (see bottom left of figure 3.14), the cavity gets a lot of time to heat up and follow the resonance frequency. For 100 mW, the resonance frequency shifts by 1.5 GHz before the conversion breaks down. Since the laser frequency goes linear with time, the deposited energy can be understood as proportional to the integral over the blue output power traces. When the laser stays resonant with the cavity for such a long time, the whole crystal is heated, which moves all resonances to lower frequencies. On the rising ramp, the resonances appear narrower than for 25 Hz, since the cavity has more time to push its resonance frequency towards the laser. The relative shift between rising and falling ramp and the shape of the resonance lines depends mainly on the ramping speed, while the input power only adjusts the peak value.

With the low ramp frequency of 0.5 Hz in the bottom right plot in figure 3.14, there is enough time to heat not only the laser beam axis, but also some of the surrounding bulk material. For 100 mW input power, the cavity stays on resonance for 0.2 s on the falling ramp; this is almost on the order of reaching thermal equilibrium inside the crystal (see section 3.2.5). During this time, the resonance frequency drifts by 2.6 GHz, which is one third of the FSR, before the conversion breaks down. It must be noted that the frequency axis scaling in this plot differs from the other three plots in 3.14 to show the whole drift.

The distortion of resonance lines with respect to the direction of the frequency ramp can be used to perform very precise absorption measurements of the material, as for example reported in [Las+10; Ste+12]. These works focused on the detection of small absorption coefficients $\alpha < 10^{-4}/\mathrm{cm}$. Similar evaluation should, in principle, also be possible from the measurement data presented in this section (although more complicated, as the light is generated inside the crystal and the absorption can, therefore, not be considered constant along the beam path). However, since the high absorption of PPKTP at 400 nm can be determined more directly with high precision, this approach was not pursued further.

3.7.3. End of ramp

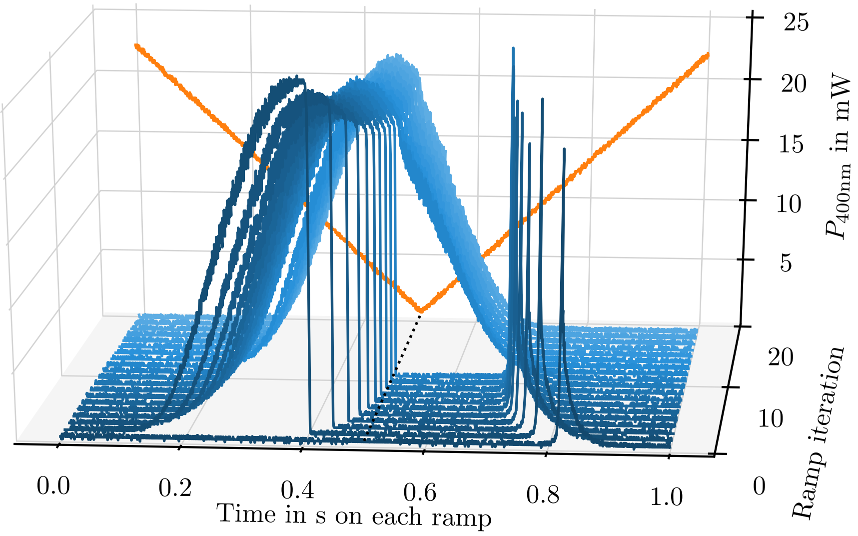

Figure 3.15.: SHG cavity's resonance frequency reaching end of laser frequency ramp. The plotted lines originate from one single time trace of duration 20 s, stacked into traces of 1 s from front to back. The input power was 95 mW and the laser frequency was ramped over 4.9 GHz with a ramping frequency of 1 Hz. The orange trace in the back plane shows the laser's frequency offset in arbitrary units. The laser was unblocked around 0.5 s. The heat deposition inside the crystal shifts its resonance frequency to lower frequencies (center of the plot) and leads to the asymmetric line shapes discussed in section 3.7.2. After 11 s, the resonance frequency has shifted so much that resonance does not break down until the end of the ramp is reached.

When the laser is switched on in ramp mode, it takes several ramp cycles to heat the crystal to its equilibrium temperature. During this process, the resonance frequencies both on rising and falling ramp reduce. If the resonance is too close to the end of the ramp in the beginning, the cavity may still be on resonance when the laser frequency reaches the end of the ramp. This is shown in figure 3.15.

For an input power of 95 mW and a ramp frequency of 1 Hz, the laser was unblocked at around $t = 0.5$ s and the time trace was recorded. Each ramp cycle is plotted in a single trace from front to back, which means the trace in the back shows the time trace for $t = 19$ s

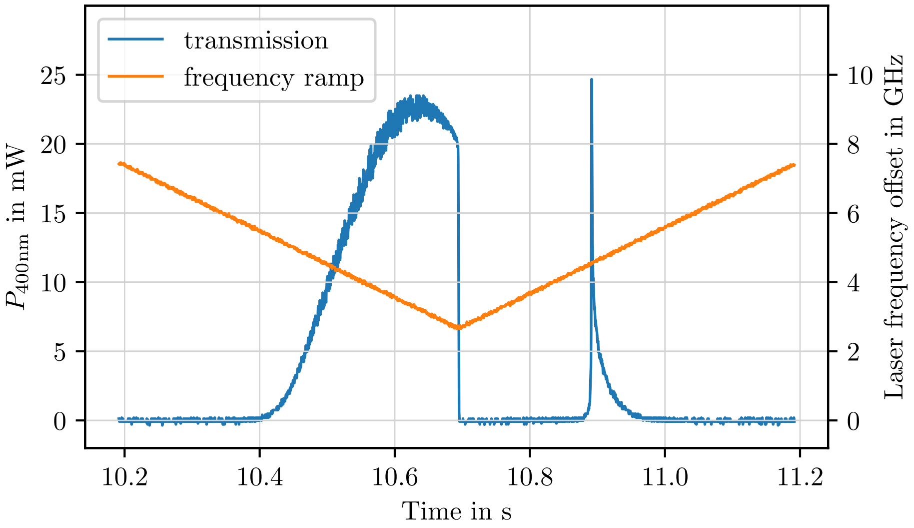

Figure 3.16.: Last slice of figure 3.15 before resonances fall together. Conversion breaks down at a laser frequency offset of 2.651 GHz while only milliseconds later, the cavity is no longer resonant at the same frequency. Resonance on rising ramp is only established at an offset frequency of 4.542 GHz 0.2 s later.

to $t = 20\,\mathrm{s}$. Apart from the discussed ramp asymmetries, it can be seen that, over time, the resonance frequencies move to lower resonance frequencies. The output power reduces during this frequency shift. After around 11 s, the resonance frequency is shifted so much that the cavity is still resonant when the end of the ramp is reached.

The ramp cycle before the end of the ramp is actually reached is of interest, since it is possible to infer a lower bound for the change in resonance frequency once no 400 nm-light is present in the cavity any more; it is therefore depicted separately in figure 3.16. The conversion breaks down at the end of the frequency ramp at an offset frequency of 2.651 GHz. Only milliseconds after, the laser reaches the same frequency again on rising ramp. One could expect that, on these timescales, temperatures change sufficiently slowly such that the laser becomes resonant again with the cavity at approximately the frequency where the resonance was lost. However, it can be seen in the experimental data that the cavity drifts away rapidly, and resonance is only reached again at a laser offset of 4.542 GHz. Thus, the resonance frequency of the cavity shifts by more than 1.891 GHz within the 0.2 s between losing resonance and gaining it again. The line shape on rising ramp does not significantly differ from a resonance in the center of the ramp; from this, it must be concluded that the resonance frequency moved much faster than the laser frequency and was already settled when the laser reached resonance on the rising ramp. Thus, the resonance frequency drift must by far exceed the ramping speed of 9.47 GHz/s. This observation is another indicator that, for fast changes on the system, the temperature-dependent refractive index has the biggest impact on the resonance condition of the cavity. Thermal expansion is too slow to explain these rapid frequency changes.

3.7.4. Resonance frequency upon locking

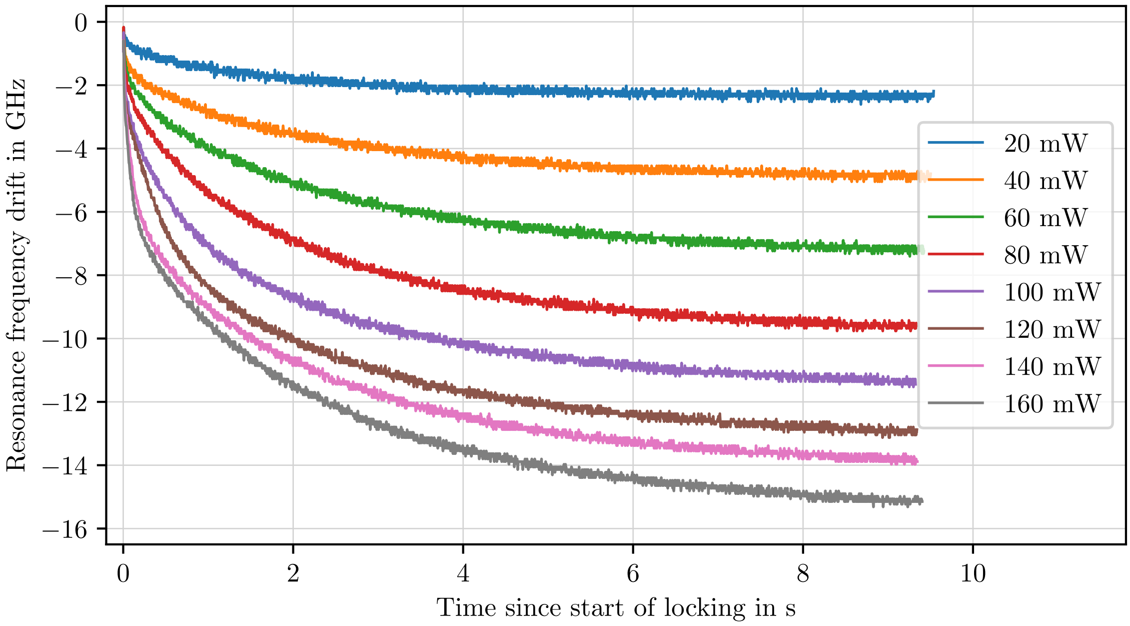

Figure 3.17.: Cavity's resonance frequency drift upon locking for varied input power. The cavity is locked at $t = 0\,\mathrm{s}$. Within few seconds, the system thermalizes to a new resonance frequency. For input powers up to 80 mW, the resonance frequency shifts by approx 0.125 GHz/mW.

As stated before, for stable output power, it turned out useful to lock the laser to the SHG cavity. Figure 3.17 shows for various input powers how the resonance frequency drifts over time towards the new equilibrium resonance frequency once the laser is locked to the SHG cavity and the generated 400 nm light heats the crystal. The system thermalizes on the order of few seconds, where the equilibrium is reached in good approximation after $6-8\,\mathrm{s}$. The most significant change in resonance frequency happens within the first two seconds after locking, which is in good agreement with the COMSOL simulation presented in section 3.2.5. Even for small input powers of 20 mW, the applied heat of approx. 1.5 mW leads to a decrease in resonance frequency by 2.4 GHz. For input powers up to 80 mW, the resonance frequency shifts by approx. 0.12 GHz/mW before reaching the new equilibrium. For 60 mW, a frequency drift of 7.24 GHz was measured, which corresponds to a shift of more than one FSR of the cavity with respect to the resonance frequency prior to locking, and for an input power of 160 mW, the frequency drift of 15.14 GHz even exceeds two FSRs.

Figure 3.18 shows the corresponding total blue output power over time after locking. For low input powers of 20 mW, the output power of the 400 nm light stays constant on the level to which it was locked. For higher input powers, the initial output power decreases slightly after the lock is closed; at 80 mW, this reduction becomes so pronounce that the output power

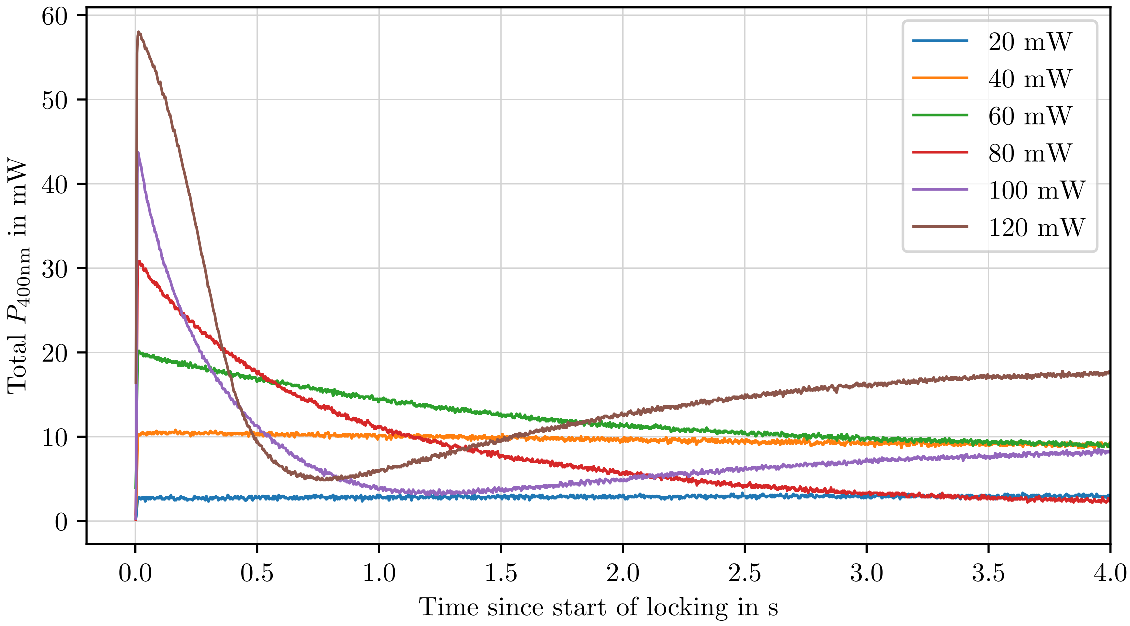

Figure 3.18.: Output powers at 400 nm upon locking. While for input powers below 40 mW the output power stays constant, it decreases over time for higher input powers. For input powers above 100 mW, the output power reaches a minimum before rising again to a constant output power.

decreases toward the same level reached with an input power of 60 mW. For even higher input powers, the initially high output powers break down within fractions of seconds. For input powers above 100 mW, the output power increases again after passing a minimum and tends to a constant output power. The figure shows that the minimum is crossed faster the higher the input power is. The traces recorded for 140 mW and 160 mW are not shown in figure 3.18 for clarity; however, they follow the same trend as the other curves: starting at higher output levels, decreasing faster and reaching higher equilibrium output power with increasing input power.

Since the laser is locked to the cavity, the reduced output power cannot be attributed to a dissonance between laser and cavity frequency, but must be due to a reduced conversion efficiency. By monitoring all output ports, it was verified that, with decreasing output power at 400 nm, the intracavity power at the fundamental 800 nm increases. The change in crystal temperature shifts both the gain profile (i.e., the wavelength at which optimal conversion occurs, see section 3.2.3) and the laser frequency itself. Up to this point, there would be two possible explanations for the decrease in power: If the speed of the resonance frequency drift exceeds the shifting speed of the gain profile, the resonance frequency could drift off the gain profile to frequencies where sufficiently less input power is converted. On the contrary, if the gain profile moves faster than the resonance frequency, it may drift away such that efficient conversion is no longer possible at the resonance frequency of the cavity.

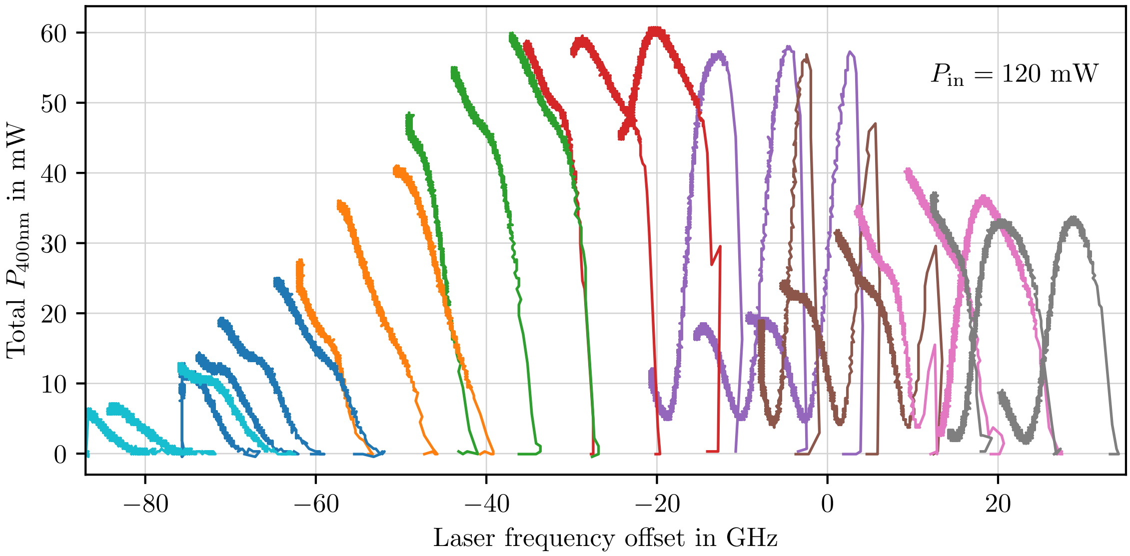

Figure 3.19.: 400 nm output power versus cavity resonance frequency at start of locking. Input power was 120 mW. Each line belongs to one cavity resonance to which the laser was locked. Traces of same color were neighboring resonances on the same ramp. Due to the limited frequency range of the laser, the crystal temperature was tuned and – with the results from section 3.8.3 – converted to an effective frequency shift. The data can be interpreted by a gain profile moving from right to left upon locking and the output power “surfing” on it, eventually reaching an equilibrium state.

Since output powers and laser frequency offset were recorded simultaneously in this measurement, it is possible to plot them against each other. In this way, the frequency drift can be visualized together with its source: the absorbed 400 nm power that heats the crystal. This is shown in figure 3.19. All data points are equally spaced in time. At an input power of 120 mW, the laser was locked to different resonances. Due to the limited traveling range of the laser’s piezo actuator, the laser can only be locked to two or three neighboring resonances for a given crystal temperature. The graphic is therefore stacked from measurements at different crystal temperatures. With the evaluation following in section 3.8.3, the increase in temperature could be converted to an effective laser frequency shift, such that the system’s behavior can be displayed over a broader frequency range. The measurement was repeated at different input powers and for each input power, a similar stacking of the measurement of single traces to a coherent picture was possible.

The frequency offset was calibrated with the frequency of optimal conversion efficiency in ramp mode at low input powers. This means that in the absence of thermal effects, the peak of the gain profile was situated around 0 Hz. For 120 mW, the initial position of the gain profile is already shifted slightly to lower frequencies.

When the laser is locked, the laser frequency offset drifts to lower frequencies as expected. While on the left side of figure 3.19 the output power increases continuously, on the right side, the output power drops to almost zero before increasing again. This behavior can be explained by a shift of the gain profile to lower frequencies, which travels faster than the laser frequency. The output power is proportional to the gain profile, evaluated at the specific laser frequency; it can therefore be thought of as "surfing" on the shifting gain profile. The rise on the left side originates therefore mainly from the gain profile shifting "under" the laser frequency and lifting the output power. Similarly, the drop in output power on the right side can be understood as the falling flank of the gain profile moving away from the laser frequency. From the re-rise of the output power, it can be concluded that the experimental gain curve has a minimum and increases again at higher frequencies. The actual form of the gain profile can be estimated from the data point right after the laser is locked, when there is no time for thermalization and shift of frequency or gain profile.

From figure 3.19, it can be seen that the right of the green traces yields the highest equilibrium output power. This point is only reached by the highly nonlinear and coupled interplay between the drifts of the gain profile and the laser frequency, which challenges the reproducibility of the optimal output power, especially at input powers above 100 mW.

3.8. Probing the SHG parametric gain profile

To characterize the SHG cavity, both the width of the parametric gain profile in frequency space and the phase-matching temperature range in which reasonable conversion occurs are quantities of interest. In a system where the cavity's resonance frequency and the phase-matching temperature can be tuned independently, these are straightforward measurements. However, this is not possible in the monolithic design, where these quantities are directly coupled to each other. Therefore, a more sophisticated approach is necessary to characterize the gain profile.

For the measurements presented in this section, the crystal's center and edge temperatures were set via a LabVIEW script and the measurement data from the oscilloscope was saved on a computer (in the same configuration as described in section 3.7.1). In this way, automatized parameter sweeps could be performed on the crystal temperatures.

3.8.1. Temperature ramp with locked laser

In a first measurement, the output power was recorded versus the crystal's center temperature for several input powers. To ensure resonance throughout the measurement, the laser frequency was locked to the SHG cavity. Together with the output powers, the laser's piezo voltage was recorded. The traveling range of the piezo actuator allowed the laser frequency to follow the cavity's resonance for more than two FSRs; in this way, mode-hops could be avoided and the traces shown in this section belong to the same longitudinal cavity mode.

For the data shown in figures 3.20 and 3.21, the NTC set voltage was increased/decreased in steps of 0.001V, corresponding to 0.045 °C. The data points were acquired with a thermalization time of 0.61 s per data point, which was the fastest that the communication for the data readout allowed. With this, a typical trace of 6.4 °C takes around 90 s to acquire.

In figure 3.20, the $P_{400\mathrm{nm}}$ output powers from both output ports are plotted separately versus the increasing and decreasing crystal temperature for various input powers between 20 mW and 140 mW. The left plots show the transmission port, while the right graphs show the power exiting in reflection. In the bottom plots, the temperatures are increased; thus, the displayed lines must be read from left to right. Similarly, the upper graphs, with decreasing temperature, were recorded from right to left. The graphs within each of the plots seem to evolve quite continuously from each other when the input power is changed. When comparing both ramp directions for the same output port, it seems that, in general, the same gain profile is shown, but stretched or compressed along the temperature axis. The two output ports show quite different responses to the temperature sweeps; both seem to have their individual gain profile, and where the output power peaks in one direction, the gain profile has a dip for this frequency in the other port. The different gains for both output ports make sense, since the generated light passes through the crystal only once before leaving the cavity; due to slight imperfections in the manufacturing process and the asymmetric temperature distribution, it is therefore no surprise that the phase matching is not exactly the same in both directions. Since the power that exits the SHG cavity in one port can no longer be converted in the other direction, it follows that the total output power must be split between both output powers, and higher gain in one port leads to a reduced output power in the other.

As expected from the discussion in section 3.7, higher input powers require a lower set temperature to reach optimal conversion; this is well displayed in the data by a shift to the left for increasing input power. It must be additionally noted that the set temperature on the bottom of the crystal does, in general, not agree with the actual temperature in the crystal; the crystal temperature will reach the set temperature only some instance after the corresponding current is applied to the Peltier element. One would for that reason expect that the gain profile probed on rising ramp is shifted to higher temperatures while the ramp down is shifted to lower set temperatures, which is in agreement with figure 3.20. This effect can be observed already at low input powers, where effects due to heating are negligible.

At higher input powers, the heating of the crystal on resonance becomes the dominating effect: When significant second harmonic light is generated in the cavity, the cavity heats up and the crystal temperature exceeds the set values (which are still the horizontal axis of the plot). This introduces a skewness into the shape of the gain profile: As the temperature is

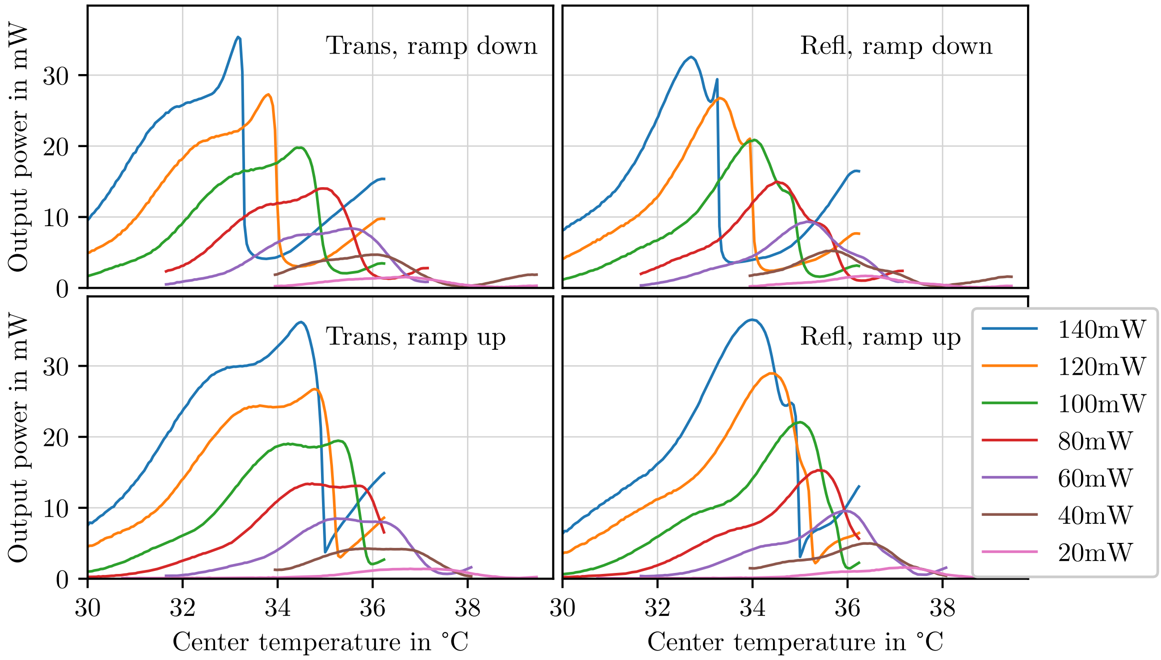

Figure 3.20.: Output powers in transmission port (left) and reflection port (right) versus the crystal's set temperature. The temperature is continuously decreased in the upper plots and increased in the lower plots.

increased towards the temperature of optimal conversion (see bottom plots in figure 3.20), a symmetric gain profile would continuously shift to higher temperatures, leading to a reduced slope compared to the (hypothetical) non-shifted gain profile. After the temperature of optimal conversion is surpassed, the heating of the crystal reduces and the gain profile starts to shift back to the left. This, in turn, reduces the output power and cools the crystal even further. The shifted gain profile now moves back to its initial position – without a change in set temperature. For this reason, once a critical set temperature is crossed, the conversion breaks down almost immediately, which is marked by the sharp edges on the right.

A similar edge arises on the falling temperature ramp (see top plots in figure 3.20, read from right to left), but at lower temperatures. Here, the gain profile remains unshifted until the set temperature approaches the phase-matching temperature. When a critical temperature and the beginning of the gain profile is reached, a self-amplifying process starts that increases the output power, further heats the crystal, and pushes the gain profile to higher temperatures such that the gain increases even more. All this happens at the same NTC set temperature, which leads to the immediate increase in output power in the top graphs of figure 3.20.

As the hysteresis arises from the fact that the set temperature and actual temperature along the beam axis do not agree, it makes sense to plot the gain profile against the laser frequency, which changes immediately with a temperature change along the beam axis. In figure 3.21,

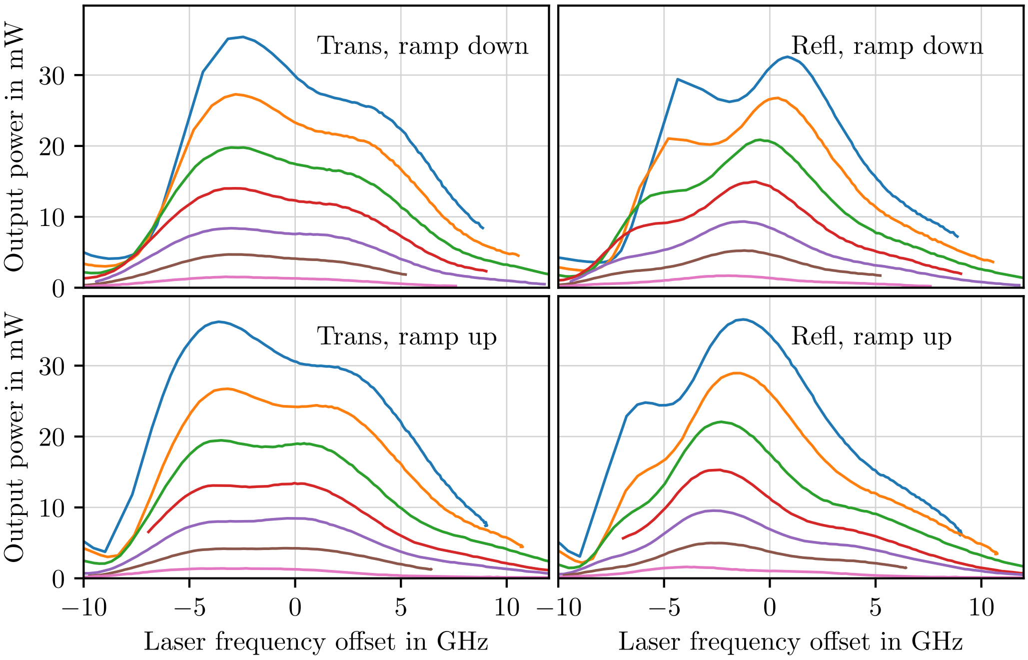

Figure 3.21.: Output powers in transmission port (left) and reflection port (right) versus the laser frequency offset. In the upper (lower) plots, the set temperature is continuously decreased (increased), which leads to an increase (decrease) in laser frequency. For legend see fig. 3.21.

the traces from figure 3.20 are plotted against the laser frequency offset. In this representation, the gain profiles look much more symmetric and the differences between rising and falling ramp reduce significantly. Since a decreasing temperature corresponds to an increasing frequency, the lines must be read in the opposite directions compared to the lines in figure 3.20. At the critical temperatures, both the output power and the laser frequency change very fast, which results, in moderate slopes for the left flank of the gain profile. Since this region is passed very fast, the density of data points is lower in this region than elsewhere in the graph; the spikes in the top right plot therefore originate from undersampling. In this representation, the gain profile seems to be almost independent from the ramp direction, but it becomes apparent that both output ports have their individual gain profile.

The nonlinear relation between the crystal's set temperature and cavity's resonance frequency at high input powers is displayed in figure 3.22. For low powers, the relation is rather linear. The hysteresis effects at low input powers can clearly be attributed to the start and end of the temperature ramp, where the set-temperature still needs to propagate to the optical axis; this effect could be reduced by using longer thermalization times for each data point. As before, the solid lines belong to the decreasing temperature ramp (read from right to left), while the dashed line of increasing temperature is read from left to right.

For high input powers, the critical temperatures, at which the system behaves nonlinearly to a change in temperature, can be read off as the temperatures at which the frequency changes

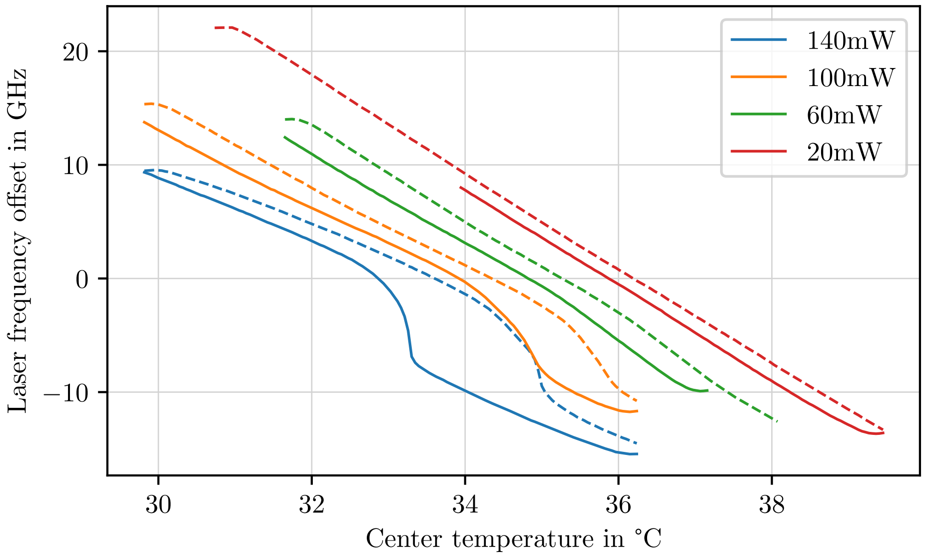

Figure 3.22.: Hysteresis of the cavity's resonance frequency for linear temperature ramp. Solid lines show decreasing temperature (and are to be read from right to left) while dashed lines correspond to increasing temperature. The response becomes significantly nonlinear for input powers above 60 mW due to heating of the cavity on resonance.

immediately. In comparison with figure 3.20, it can be seen that these critical temperatures are indeed the temperatures at which the output power suddenly increases/decreases. This nonlinear response to the only experimentally accessible parameter makes it hard to operate the monolithic SHG cavity close to resonance at high input powers.

3.8.2. 2D Temperature scan

The measurement from section 3.8.1 was extended to a 2D scan, where the crystal's center and edge temperature could be set separately. The center temperature was increased in steps of 0.0025 V in the NTC-voltage, corresponding to 0.115 °C. For each center temperature set point, the edge temperature was tuned between 33.48 °C and 41.74 °C in steps of 0.23 °C. The 2D-parameter space was scanned in a snake-like pattern: While the center temperature was continuously increased, the edge temperature was alternating between rising and falling temperature to avoid temperature jumps between adjacent data points. The thermalization time was 8.6 s for each data point at an input power of 20 mW. The scanned parameter space was limited by the traveling range of the piezo actuator; in this range, the laser stayed locked to the same longitudinal mode throughout the measurement, following all thermal drifts.

On left side of figure 3.23, the total output power is shown. One can see that high conversion efficiencies are only reached in a narrow temperature range for the center temperature of

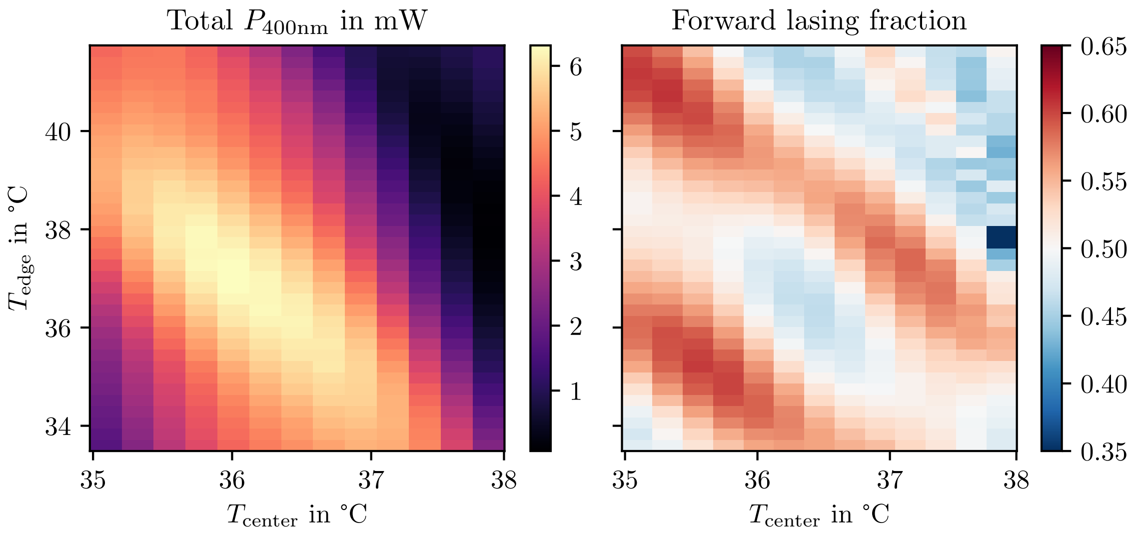

Figure 3.23.: Total output power (left) and forward lasing fraction (right) versus crystal's center and edge temperatures. The data was recorded at an input power of 20 mW and a thermalization time of 8 s for each data point.

35 – 37 °C, while a much broader edge temperature range 34 – 40 °C is compatible with high conversion efficiencies. This in good agreement with the design considerations that the edge temperature has only limited influence on the total output power and can be used to tune the cavity's resonance frequency without significantly reducing the conversion efficiency.

The optimal output power is reached at a center temperature of 36.0 °C and an edge temperature of slightly higher 37.0 °C. This makes sense, since these temperature are the set temperatures at the bottom of the crystal, and the center of the crystal is shielded better than the end facets, which directly allow heat dissipation into the surrounding air. The diagonal orientation of the area with high conversion efficiency indicates that the set temperatures in the center and edge region of the crystal can, at least partially, compensate each other.

The right side of figure 3.23 shows the forward lasing fraction. Where high conversion occurs, the light seems to have a weak preference to exit through the reflection port. Neither center nor edge temperature can tune this ratio without significantly reducing the total output power.

In initial measurements with a ramped laser, it could be observed that the parametric gain vanishes for temperatures below the design phase-matching temperature, but that above this temperature, conversion periodically reoccurs (albeit at much lower conversion efficiency). This feature is not expected from the theoretical considerations in section 2.7. To study this feature, a 2D temperature scan similar to the one in figure 3.23 was performed for a broader temperature range; the results are shown in figure 3.24. T_{center} was ramped from 33.5 °C to 46.3 °C in steps of 0.459 K, while T_{edge} oscillated between 32.6 °C and 43.9 °C, also in steps

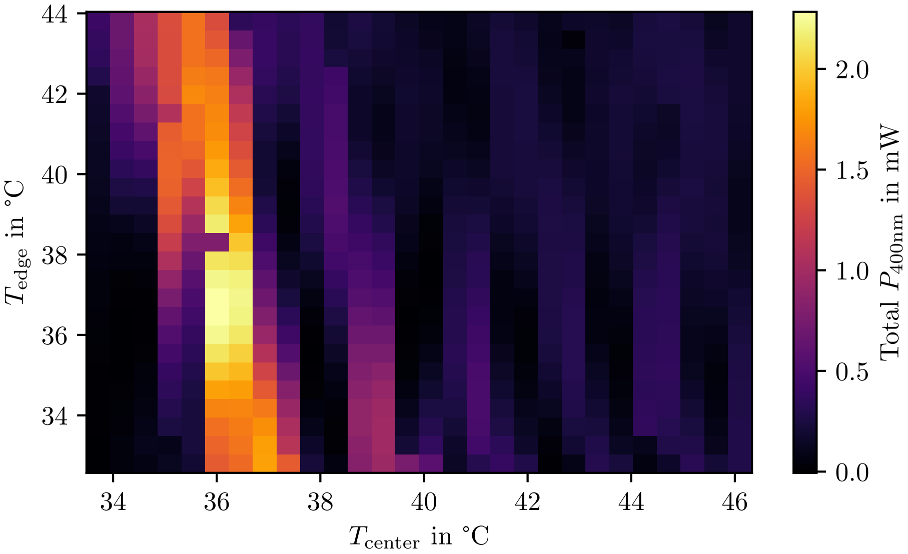

Figure 3.24.: Total output power versus the crystal's center and edge temperatures. Above the phase-matching temperature, a reduced conversion reoccurs approximately every 2 K.

of 0.459 K. The thermalization time in this measurement was 2 s per data point. Due to the broader temperature range, the laser could not remain locked to the same longitudinal mode. Instead, the piezo's traveling range was limited to 15.5 V, which corresponds to one FSR. If the resonance frequency drifed out of this frequency range, a relocking scheme found the next cavity resonance within the region of interest and locked to this. It is due to this feature that figure 3.24 contains discontinuities: the conversion efficiency on two neighboring resonances can be quite different. Single dark spots correspond to points where the resonance was lost due to the relocking procedure at the moment of data acquisition. The measurement was performed at an input power of 10 mW.

As expected from the previous observations, figure 3.24 shows moderate revivals of the output power when T_{center} increases. For a fixed edge temperature (e.g., $T_{\mathrm{edge}} = 36.0\,°\mathrm{C}$), some output power is also generated for $T_{\mathrm{center}} = 39\,°\mathrm{C}$, $41\,°\mathrm{C}$, $43\,°\mathrm{C}$ and $44.5\,°\mathrm{C}$. As before, the edge temperature may compensate for the center temperature, such that higher edge temperatures shift the revivals to lower center temperatures.

3.8.3. Linewidth and temperature drift of the gain profile

For a single pass SHG, the gain profile versus laser frequency can be recorded directly by applying a laser frequency ramp. If the nonlinear crystal is placed inside a cavity, the cavity needs to be resonant with the laser throughout the measurement to obtain this information. In the monolithic design, this cannot be realized due to the coupled degrees of freedom.

For fixed crystal temperature, the laser is resonant only at the cavity resonances, which are, in this case, spaced by 7.034 GHz. With a maximal laser frequency range of up to 25 GHz, at maximum four resonances appear on the laser frequency ramp; the SHG gain profile can therefore only be probed at these specific frequencies. Consequently, a fit with three free parameters (width, height and centroid position of the gain profile) cannot return any scientifically meaningful results. However, with the procedure described below, it was possible to infer a linewidth of the gain profile in frequency space and to quantify the gain profile drift due to changes in the crystal temperature.

A 2D-Scan of the crystal temperatures similar to the one in section 3.8.2 was performed with an input power of 20 mW and a thermalization time of 10 s. The center temperature was increased in steps of 0.229 °C, while the edge temperature was ramped up and down in steps of 2.29 °C. In contrast to the measurement from section 3.8.2, the laser was not locked, but its frequency was ramped. For each combination of temperatures, the ramp and the resulting mode spectrum of the 400 nm-light were recorded. This data set provides several traces that are all subject to the same gain profile, but shifted with temperature and probed at different laser frequency offsets. Consequently, it makes sense to fit the properties of the gain profile with a joint fit of the form

$$P_{400\mathrm{nm}} = A \cdot \exp\left(-\frac{1}{2}\left(\frac{\Delta f - (f_0 + \chi_T \cdot T_{\mathrm{center}})}{\sigma}\right)^2\right) \tag{3.3}$$

to the magnitude of the resonance peaks of the traces recorded at different center temperatures T_{center}. In this fit, A is the amplitude and σ is the standard deviation of a Gaussian gain profile (from which the FWHM-linewidth γ can be obtained by $\gamma = 2\sqrt{2\ln 2}\sigma$), Δf is the laser frequency offset, and $f_0 - \chi_T \cdot T_{\mathrm{center}}$ is the temperature-dependent center frequency of the gain profile; the model assumes a linear drift χ_T of the gain profile with the crystal's center temperature T_{center}. The parameter f_0 would be the (hypothetical) center of the gain profile for $T = 0\,^{\circ}\mathrm{C}$.

The Gaussian fit is a simplification to obtain a measure for the width of the gain profile and its drift. In the experiment, it can be observed that basically no conversion occurs below the optimal phase-matching temperature, while many local conversion maxima and minima can be observed when increasing the phase-matching temperature beyond this point (see figure 3.24). To avoid the fitting of data points that cannot be well approximated by a Gaussian, the fitted data was restricted to data points from the central peak and of sufficient prominence.

Only the traces with an edge temperature of 36.0 °C were used for the fit. Hysteresis effects could be observed depending on the ramp direction of the laser frequency and whether the data point had been recorded on increasing of decreasing edge temperature. To allow for different frequency offsets that absorb this effect, the parameters were fitted for all four cases individually and the fitted linewidths and temperature shifts were averaged afterwards.

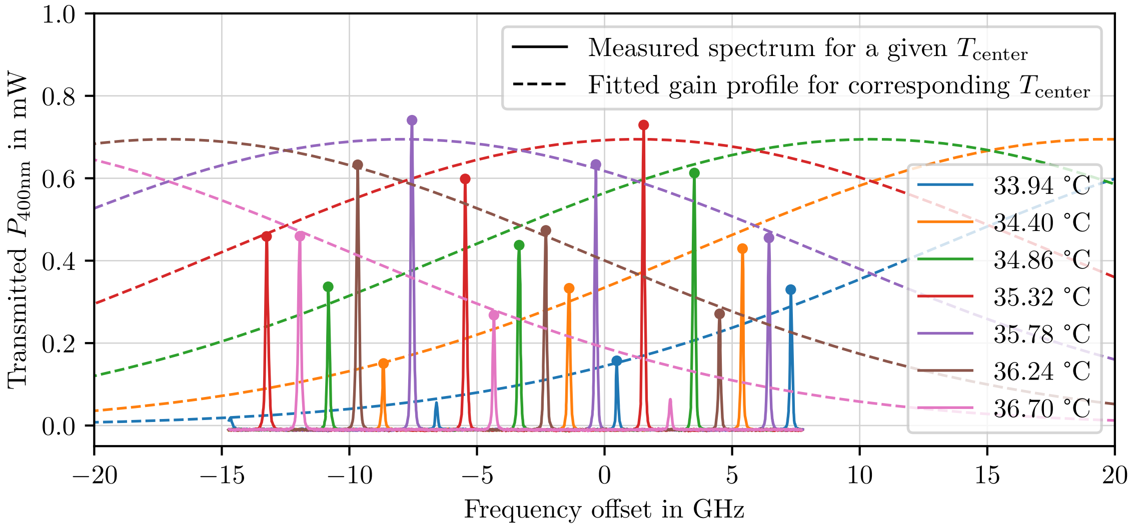

Figure 3.25.: SHG gain profile fit versus laser frequency for various crystal center temperatures. Solid lines show the measured spectra. All marked peaks were included in a joint fit to yield the FWHM of the gain profile ((38.95 ± 2.62) GHz) and its shift with temperature ((−20.04 ± 1.02) GHz/K). The dashed lines show the fit result for given T_{center}. Input power was 10 mW.

Figure 3.25 shows the data for increasing edge temperature and rising frequency ramp. Each color belongs to one specific T_{center} between 33.94 °C (blue) and 36.7 °C (rose) in steps of 0.46 °C, for which the spectrum was recorded (solid lines). The dots indicate the peak positions that were included in the fit. The fitted width σ and shift with respect to temperature χ_T of the gain profile can be found in the first line of table 3.1. The other lines are similar evaluations, performed on the data sets with different ramp directions for frequency and edge temperature. Averaging all four evaluations and performing Gaussian error propagation yields $\sigma = (16.28 \pm 0.48)$ GHz, corresponding to a FWHM linewidth $\gamma = (38.34 \pm 1.13)$ GHz, and a drift of the gain profile of (-20.01 ± 0.55) GHz/K. With 33 %, this is significantly smaller than the 30 GHz/K from section 3.2.3; however, this deviation originates from the fact that in section 3.2.3, the edge temperature was not powered (and the whole crystal could follow the set temperature) while for this section's measurement, the edge temperature was

Temperature ramp	Laser ramp	σ [GHz]	$\Delta\sigma$ [GHz]	χ_T [$\frac{\text{GHz}}{\text{K}}$]	$\Delta\chi_T$ [$\frac{\text{GHz}}{\text{K}}$]
up	up	16.28	±0.90	-20.04	±1.02
up	down	16.08	±0.92	-20.11	±1.06
down	up	16.22	±0.90	-19.94	±1.03
down	down	16.54	±1.11	-19.95	±1.24
	averaged	16.28	±0.48	-20.01	±0.54

Table 3.1.: Fitted SHG gain profile parameters

kept at 36.0 °C; consequently, the center temperature acts only on part of the crystal and is always counteracted by the edge temperature. The impact of the center temperature on the system is therefore reduced, and the gain profile shifts less with the same change in the center set temperature.

The joint fit leads to a remarkable agreement with the experimental data: While fitting each trace separately does not lead to scientifically meaningful results, the joint model reasonably describes the heights of different peaks depending on the center temperature. All peak positions lie very close to the fitted gain profiles. It must be emphasized once more that all dashed lines belong to the same fit, but differ in shape, since they belong to different parameters T_{center}. In this way, information about the gain profile could be obtained that is not directly accessible in the monolithic design.

3.9. Degradation of monolithic SHG cavity

3.9.1. Conversion efficiency over time

In the long run of the experiment, a substantial decrease in output power was observed. Figure 3.26 shows four conversion efficiency curves: The blue curve was recorded directly after crystal 1 was integrated into the setup. Since the initial measurements on crystal 1 were limited to input powers of 80 mW, the high power values displayed in the orange curve were

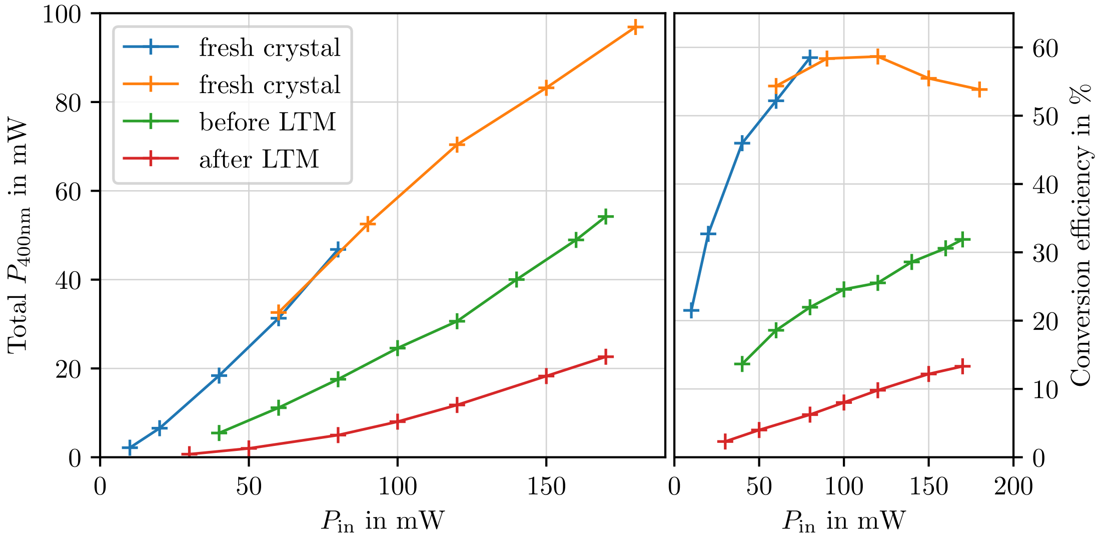

Figure 3.26.: Degradation of the SHG cavity's output power (left) and conversion efficiency (right) in crystal 1. Conversion efficiencies were measured on fresh crystals (blue and orange), after all measurements on crystal 1 were performed (green) and after the longterm measurement (LTM) at $P_{\mathrm{in}} = 170\,\mathrm{mW}$ over 96 h (red).

measured on crystal 2; however, since both crystals were manufactured in the same process and figure 3.10 shows perfectly similar behavior of crystal 1 and crystal 2 at low powers, it can be assumed that the initial output powers of crystal 1 most likely were on the same level. This performance level stayed constant over several months, during which occasionally characteristic measurements were performed on the SHG cavity at low input powers of usually 20 mW or below. The green curve was recorded after the majority of the measurements presented in this thesis have been performed, including the squeezing measurements described in the next chapter, which required a continuous 400 nm output power at around 15 – 20 mW in transmission. At that time, this output was generated from 100 – 150 mW input power over several hours of continuous operation. During the measurements, the total conversion efficiency dropped from more than 58 % to at maximum 30 %, which could only be reached for input powers above 160 mW. To study the degradation further, a longterm measurement with an input power of 170 mW was performed over 97 h, which further reduced the maximal conversion efficiency to around 13 %, as can be seen from the red trace in figure 3.26. The longterm measurement will be described in detail in section 3.9.3. The reduction in conversion efficiency can be explained by gray tracking of the crystal due to photochromic damage.

3.9.2. Gray tracking in KTP

Degradation effects as presented in figure 3.26 have been observed and studied since the first experiments with KTP for frequency conversion [Dri+86]. After illumination with visible light from the blue-green spectrum, KTP shows photochromic damage, increasing the absorption in this crystal regions over the whole visible and into the infrared spectrum [Bou+99]. Due to the visible gray tracks along the laser axes, this phenomenon is also referred to a gray tracking. Already early studies found that gray tracking in KTP is correlated with Ti^{3+} color centers [Roe89; And+92] that can be activated by 532 nm [Loi+92] and 355 nm-light [Bou+94]. It was also reported in these early works that most of these gray tracks vanish at room temperature on different timescales, ranging from minutes to months [Loi+92].

Around the same time, Polzik *et al.* observed increased absorption losses in $KNbO_3$ for 854 nm, which occurred only in the presence of a 427 nm blue pump beam [PCK92b; PCK92a; MPK94]. Phenomenologically, this blue-light induced infrared absorption (BLIIRA) was defined as “the difference between the passive infrared absorption of a crystal and the infrared absorption that it exhibits when it is simultaneously illuminated by blue light” [MPK94]. For $KNbO_3$, Mabuchi *et al.* found that the infrared absorption level increases within milliseconds after the start of illumination and relaxes within fractions of a second after illumination [MPK94]. Measurements by Hirohashi *et al.* show that other ferroelectrics like (MgO-doped) $LiNbO_3$ [Fur+01] or (MgO-doped) $LiTaO_3$ [Nak+02] experience a similar time dependence in increased absorption after illumination with blue or green light. In this view, also the temporal dynamics of increasing and decreasing absorption in KTP after illumination has been studied, showing a similar behavior like the aforementioned ferroelectrics, but on much

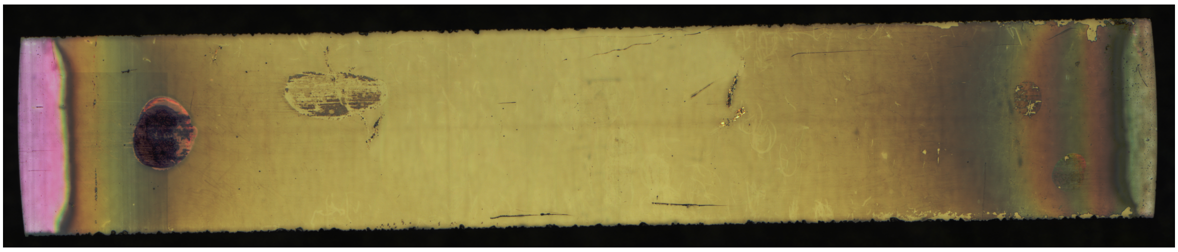

Figure 3.27.: After the longterm high-power measurement, gray tracks in the SHG crystal are clearly visible along the laser beam path. The colors at the crystal edges originate from diffraction on the coating material. The dot on the left is a marker on the surface for the orientation of the crystal. The picture is a composite of 16 microscope images.

slower timescales [Hir+07]; hence, the gray tracking of KTP has in some cases also been termed BLIIRA [WPL04; Hir+07; Tjö+15], although, in this case, the absorption persist clearly beyond the illumination.

Although the microscopic mechanisms may be specific to the material, the fundamental concepts for BLIIRA in $KNbO_3$ and gray tracking in KTP are the same: both processes are associated with color centers, that can be activated by illumination with blue light and that decay on specific, temperature-dependent time scales. In this way, BLIIRA can be understood as gray tracking of the crystal that decays on very short timescales after and during illumination. Gray tracking and BLIIRA can be saturated [Hir+07]; in KTP, the saturation absorption depends on the density of Ti color centers [WPL04], which depends on the manufacturing process and stress within the crystal. For this reason, periodically poled crystals in general face higher absorption after illumination with blue light than bulk crystals (despite having the same absorption coefficients in the infrared spectrum prior to the illumination) [WPL04; Hir+07]. Since most early experiments used pulsed lasers to reach high peak intensities, Fève *et al.* studied the gray-tracking threshold dependence on the Q-switch frequency and concluded that the relevant quantity for the gray-tracking saturation level is the average applied power [Fèv+97]. The details of the gray-tracking mechanism are still not fully understood and subject of ongoing research [Boc+20; BGS25].

Gray tracking effect could directly be observed in the experiment: After the longterm measurement presented in section 3.9.3, the crystal was removed from the experiment and observed under a ZEISS Imager.D2m microscope. The crystal was illuminated with white light from the back. Figure 3.27 is a composite from 16 high-resolution images; a gray track of increased absorption is clearly visible along the beam propagation axis in the center of the crystal. In the measurements by Boulanger *et al.*, the gray tracking increased the losses over the whole visible spectrum, reducing the transmission through a KTP sample of 8 mm length by 1 − 2 % for wavelengths around 800 nm and by 3 − 8 % for 400 nm [Bou+99]. Due to the high finesse of the cavity at 800 nm, already small absorption at 800 nm can become the dominating limitation, since it significantly reduces the intracavity power and, thus, the effective pump power for the SHG process. The reduction in conversion efficiency shown in figure 3.26 can therefore well be explained by gray tracking of the PPKTP crystal.

3.9.3. High-power longterm measurement on degraded crystal

Two longterm measurements were conducted to survey stability and conversion efficiency of the SHG cavity over several hours of operation. In a first measurement, the degraded crystal from figure 3.26 was pumped with 170 mW input power over 67 h; all output powers (400 nm and 800 nm in both transmission and reflection) and losses are plotted against the time in figure 3.28. The powers were acquired in time steps of 5 s for 46 h, after which the data acquisition accidentally stopped; the operation continued for another 21 h. Due to the high finesse of the cavity at 800 nm, the transmitted pump power is in good approximation proportional to the intracavity power. The total optical losses were calculated by subtracting all output powers from the input power. Temperatures were adjusted after 18 h, 41 h and 63.5 h to optimize total output power.

Figure 3.28 shows different phases, in which different processes lead to the reduction of the total output power. At the beginning of the measurement, the laser was locked and the crystal temperatures were tuned to achieve the highest total output power of 51.2 mW; this was the case for $T_{\text{center}} = 33.72\,^{\circ}\text{C}$ and $T_{\text{edge}} = 30.78\,^{\circ}\text{C}$. Within the first four hours of operation, the output power reduced to below 20 mW; after this time, the output powers show only slight fluctuation and decreasing output power. This reduction comes together with an increase in the intracavity power and increased reflection of the input light. The increased intracavity power indicates that the reduction in output power does not originate directly from increased absorption in the crystal, but that the gain is reduced, supposedly due to a rise in temperature along the beam axis, which shifts the gain profile away from the laser frequency, thereby reducing the conversion efficiency. As shown in the top plot of figure 3.28, the overall optical losses increase once less power is converted to 400 nm; this means that the losses are dominated by absorption at the fundamental wavelength when the intracavity power increases. On the contrary, if the losses were primarily due to absorption of the 400 nm light, one would expect a reduction of the overall losses with decreasing harmonic output power.

After 18.5 h of operation, the temperatures were adjusted to yield highest output power again; this was the case for $T_{\text{center}} = 33.26\,^{\circ}\text{C}$ and $T_{\text{edge}} = 31.10\,^{\circ}\text{C}$, which yielded a total output power of 37.2 mW. The reduced center set temperature compensates for increased absorption along the beam path, that had heated the crystal to temperatures above optimal conversion. With the new crystal temperatures, the output powers in transmission and reflection behave similarly to the start of the longterm measurement, although on slower timescales: First, the power in the reflection port decreases continuously, while the transmission port remains relatively constant. After a certain time, the power in the transmission port breaks down and

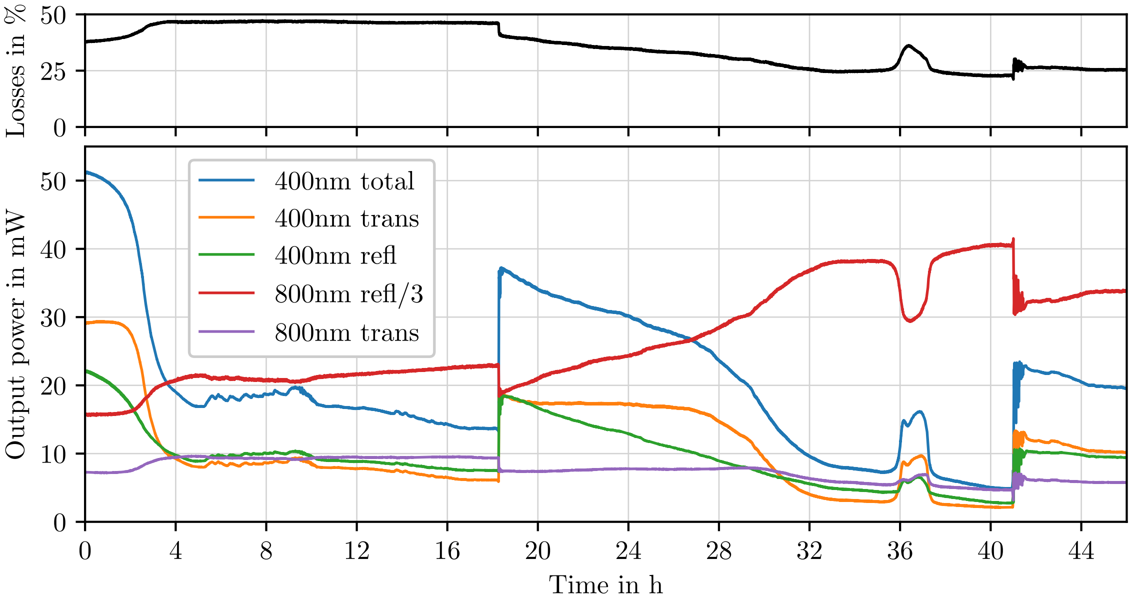

Figure 3.28.: Longterm measurement on a degraded crystal. For clarity, the reflected 800 nm light is scaled down by a factor of 3 (with the actual powers ranging between 47 – 124 mW). The total optical losses are given in fractions of the input power $P_{\text{in}} = 170\,\text{mW}$. The transmitted 800 nm trace is proportional to the intracavity power.

decreases much faster than the power in the reflection, yielding a steady state in which the output power in transmission is lower than the power in the reflection port. This behavior makes sense, since both processes are subject to the same parametric gain profile, that gets shifted with increasing crystal temperature. In section 3.8.1, it was shown that transmission and reflection ports have different gain profiles, which explains why, in both descends, the reflection port decreases first and the transmission stays approximately constant before decreasing rapidly below the output power in the reflection port.

For the second descend, it must be noted that, in contrast to the first descend, the intracavity power decreases this time (although the laser was locked to the cavity and resonance is maintained throughout the measurement). The reflected power doubles, which indicates that the 800 nm light is back-reflected and can no longer enter the cavity as easily as before. Both effects can be explained by increased intracavity losses for the 800 nm pump wavelength. Since only the light entering the cavity is subject to absorption, the overall losses reduce during the second descend.

41 h after start of the measurement, the temperatures were adjusted again to yield highest conversion on the mode that the laser was locked to. This time, a slight decrease in set temperature of $T_{\text{center}} = 33.07\,°\text{C}$ at a stable $T_{\text{edge}} = 31.06\,°\text{C}$ was necessary to optimize output power. This optimization was a lot less responsive than the previous ones: it was not

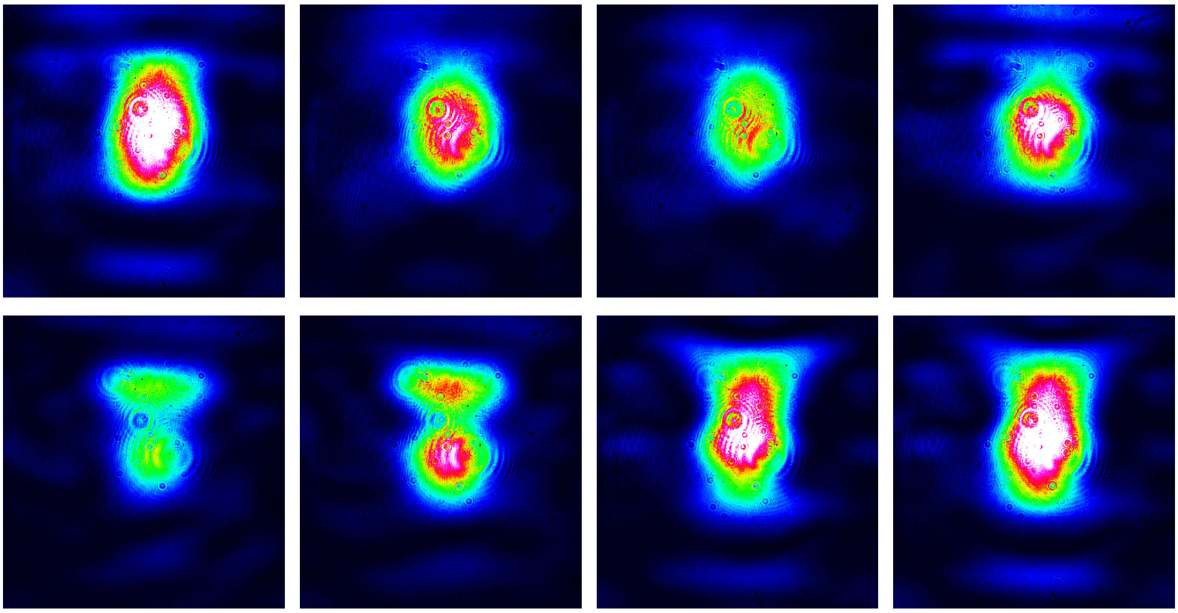

Figure 3.29.: Beam profile of the transmitted 400 nm light after high power longterm measurement for different T_{center}. The laser stayed locked to the same longitudinal mode throughout the measurement.

possible to operate stably on the temperatures that yielded highest overall output power. A point of stable operation was found at $T_{\text{center}} = 34.13\,°\text{C}$ and $T_{\text{edge}} = 32.34\,°\text{C}$, which were the parameters that were kept until the end of the measurement. In contrast to the first temperature adjustment, the intracavity power increased this time, which also lead to an increase in output power.

The data acquisition stopped after 46 h due to a technical error, and the laser stayed in lock for another 17.5 h. The output power after this time was not recorded. Adjustments of $T_{\text{center}} = 34.08\,°\text{C}$ and $T_{\text{edge}} = 32.58\,°\text{C}$ optimized the output power to 15.77 mW (8.51 mW in transmission and 7.20 mW in reflection). With a decrease of the center temperature to $T_{\text{center}} = 33.85\,°\text{C}$ and an almost constant $T_{\text{edge}} = 32.43\,°\text{C}$, a strong asymmetry in the output ports could be reached, with 9.54 mW in transmission and 5.33 mW in reflection.

The laser remained locked to the same mode for another 3.5 h. During this time, the beam profile was recorded with a Thorlabs BC106-VIS CCD camera beam profiler for small adjustments of the center temperature T_{center}. For a fresh crystal, a symmetric Gaussian beam profile would be expected, and an adjustment of the phase-matching temperature should not change the spacial beam profile. However, the beam profiles shown in 3.29 were all recorded while the laser stayed locked to the same cavity resonance.

The displayed beam shapes are far from the expected TEM_{00} mode. Most of the shapes are elliptical, while for some temperatures, there are even two separated regions with high intensities with a low-intensity region in between. To explain this, it must be noted that the shape of TEM modes is derived from the assumption of a homogeneous medium between two conductors and constructive interference of all round trips. In the degraded crystal, the gray tracking leads to spatially inhomogeneous absorption coefficients. When the cavity mode changes due to a change in crystal temperatures, this may lead to a changing spatial intensity distribution with new mode shapes. Once absorption increases along the center of the beam axis, it may be that the fundamental intracavity power gets optimized by a spatial intensity distribution that avoids high intensities in the high absorptive crystal regions. The laser is locked to the condition that most light enters the cavity; therefore it seems plausible that the coupling efficiency can be optimized for deviations from the TEM_{00} that are subject to fewer losses. Also, if the temperature is not tuned, slow changes in the absorption distribution may lead to changes in the spatial mode shape.

The described mechanism would, on one hand, explain why such different output beam shapes can be generated from the same symmetric input beam. On the other hand, it is one plausible explanation for the interesting feature that arose 36 h after the start of the longterm measurement, when suddenly the output power increased again for 45 minutes to around 16 mW before continuing the descend in output power to the previously stable 8 mW of total output power. The output power increased mainly in the transmission port. It seems plausible that, at this point, the initial mode was degraded with ever increasing absorption and another spatial intensity distribution yielded higher intracavity power. Once the light travels in regions it did not before, it passes regions where absorption is low and higher intracavity power is possible (as recorded in the experiment). A heating of the crystal may then even push the gain profile in a beneficial direction, such that the total output power significantly increases. Once the absorption increases in this region, too, the beam shape may return to the initial configuration. There is no evidence for external factors that could have triggered or would explain the rise in output power after 36 h of measurement: the feature appeared around 7:30 am in the morning, when nobody was present in the laboratory. There were no irregularities in the air conditioning system. Temperature fluctuations may have triggered the transition; however, the ambient temperature was not changed during the measurement and can therefore not be the single reason for a change of the crystal temperature and shift of beam profile. Also a shift of the gain profile alone cannot explain the rise in intracavity power after 36 h, since this would lead to a decrease of the intracavity pump power, which was not observed.

Immediately after the laser was unlocked after the longterm measurement, the oscilloscope traces from figure 3.30 were recorded at an input power of 170 mW. The laser ramp covers three FSRs, and prior to locking for the longterm measurement, exactly three cavity resonances indicated the excellent mode matching of the laser to the TEM_{00} of the SHG cavity. However, after the longterm measurement, these modes have disappeared completely; the left plot of figure 3.30 was recorded at $T_{\mathrm{center}} = 26.0\,^{\circ}\mathrm{C}$ and is exemplary for most crystal temperatures: the increased optical losses in the center of the crystal omit an increased in-

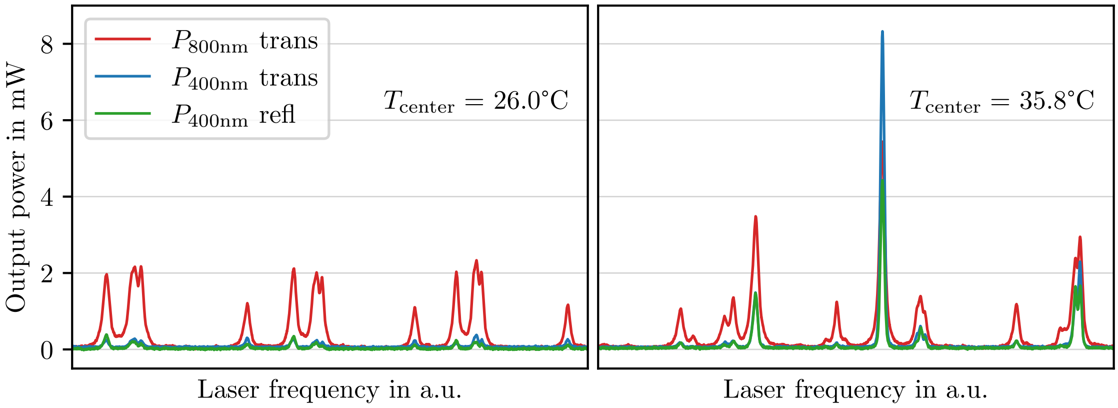

Figure 3.30.: Mode spectrum after the longterm measurement below (left) and at the phase-matching temperature (right) at 170 mW input power. Although there should be three TEM_{00} resonances on the ramp, they are no longer visible. At the phase-matching temperature, there is exactly one mode for which the light can still enter the cavity and conversion occurs.

tracavity power on resonance. The periodicity in the intracavity power indicates different FSRs of the cavity, but the TEM_{00} resonances are no longer visible. As expected, far from the phase-matching condition, no output power is generated.

Close to the optimal phase-matching temperature (where the SHG cavity was operated during the longterm measurement), even the periodicity for successive FSRs vanishes, as can be seen in the right plot of figure 3.30. The resonance peak in the center is the only TEM_{00} mode at which some light can still enter the cavity and significant harmonic output power is produced. The output power is on the level recorded at the end of the high power longterm measurement. It seems plausible that this mode has formed over time such that intensity distributions and loss distributions match to each other, and that the other longitudinal modes are no longer compatible with the spatial distributions of the absorption centers.

3.9.4. Longterm measurement on fresh crystal

To yield more quantitative results, a similar measurement as presented in the preceding section was performed on a fresh crystal, that had, with few exceptions, only been operated at input powers below 20 mW to avoid degradation effects as much as possible; the conversion efficiency measurement presented in figure 3.31 and the measurements described in section 3.8.1 were the only measurements, which required input powers of more than 20 mW, and the grid measurement from figure 3.23 was acquired during 20 min at a moderate input power of 20 mW. The green curve in figure 3.31 shows a drop in conversion efficiency due to the absorption induced by these measurements. Subsequently, a longterm measurement was performed for 17 h, during which the laser was illuminated with 100 mW input power.

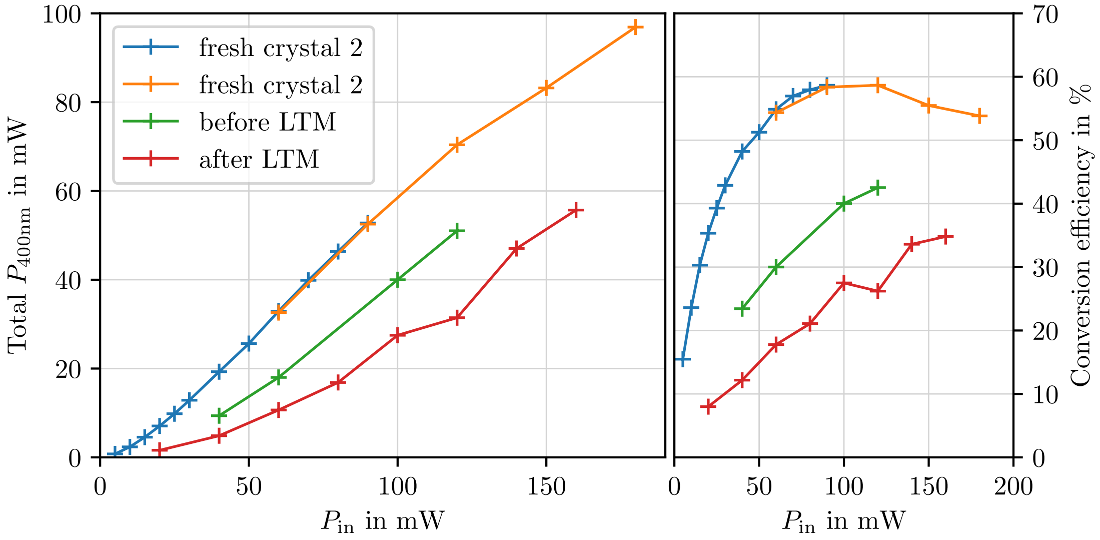

Figure 3.31.: Degradation of the SHG cavity's output power (left) and conversion efficiency (right) in crystal 2. The performance was measured on a fresh crystal (blue and orange), after few hours of operation at input powers below 20 mW (green) and after the longterm measurement (LTM) of 17 h at an input power of 100 mW (red).

The red trace in figure 3.31 shows the direct effect of the 17 h longterm measurement, which significantly reduced the output power that could be obtained from the SHG cavity.

The longterm measurement data is shown in figure 3.32. For $P_{\text{in}} = 100\,\text{mW}$, the system initially yields a total 31 mW output power. While the transmitted power decreased from 17 mW to 10 mW, the power in transmission decreased from 14 mW to 12.5 mW. During this time, the intracavity power remained relatively approximately constant. From the low conversion efficiency, it must be concluded that the measurement was not performed at the optimal phase-matching temperature, but that substantial pump light was not converted but absorbed inside the crystal.

The beam profile in transmission was measured at the beginning and at the end of the longterm measurement – the exact moments can be seen in figure 3.32, when the blue trace drops to zero. The recorded beam profiles are shown in figure 3.33. The initial similarity of the spatial intensity distribution with a TEM_{00} mode indicates that, up to this point, there was no significant impact of absorption on the mode shape. However, during the measurement, the total losses increased, which deforms the mode: After 17 h, the beam profile has become significantly more vertically stretched out – not elliptical, but with a dip in the center. It must be pointed out that the laser was locked to the same spatial mode the whole time, and figure 3.33 really shows the evolution of the fundamental cavity mode as the absorption along the beam axis gradually increases.

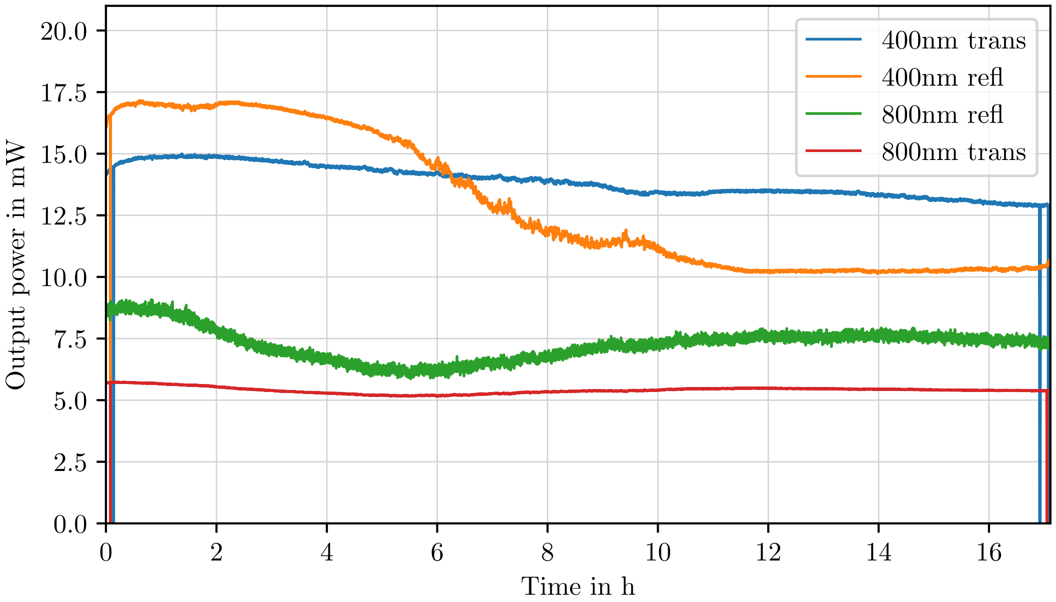

Figure 3.32.: Longterm measurement on a fresh crystal. During 17 h of measurement with 100 mW input power, the intracavity power (red) stays constant. While the transmitted 400 nm output power reduces only slightly from 15 mW to 13 mW (blue), the power in the reflection port decreases from 17 mW to 10.5 mW (orange).

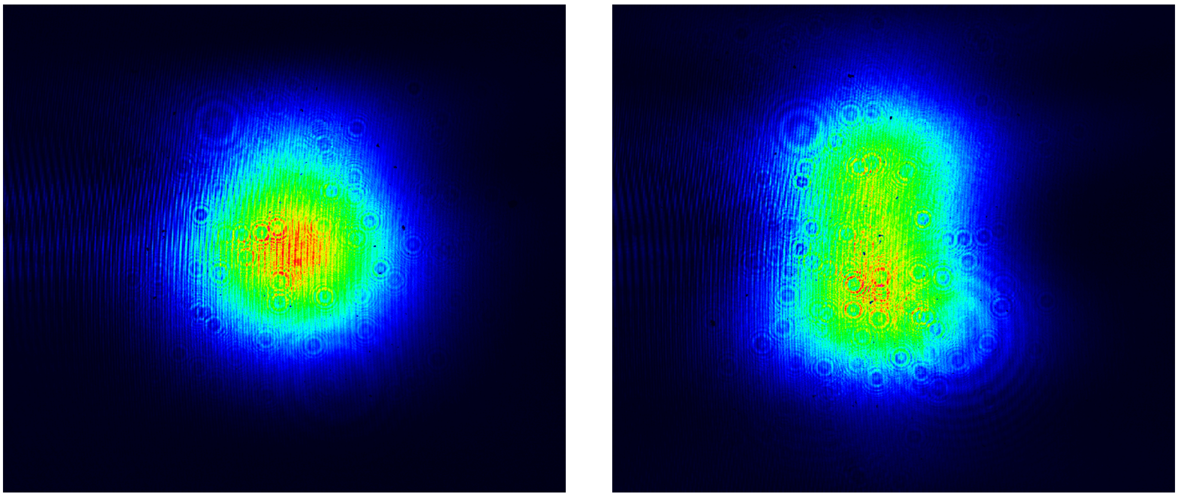

Figure 3.33.: Mode shapes of the transmitted 400 nm light before (left) and after the longterm measurement (right) for 17 h at 100mW with a fresh crystal.

3.9.5. Crystal recovery

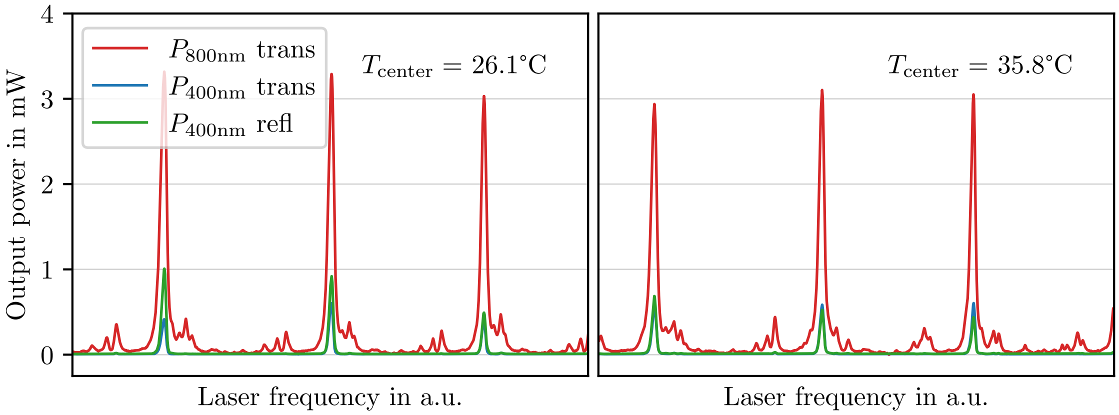

Figure 3.34.: Mode spectrum after 97 h of recovery at 135 °C at an input power of 80 mW. The temperatures are the same as in figure 3.30, allowing direct comparison. The TEM_{00} modes are partially restored and weak conversion occurs for both temperatures.

Previous experiments suggest that residual gray tracks in KTP can be substantially reduced or removed completely by heating the crystal; it can, however, not prevent the forming of increased absorption in the first place [Tjö+15]. The characteristic relaxation time constant strongly depends on the crystal temperature, ranging from 31 min at 85 °C to 17 min at 95 °C down to 9 min at 115 °C [WPL04]. Complete recovery of the gray tracks was reported by annealing a KTP crystal at 200 °C for 30 min [Zha+11]) or 100 °C for two days [Bou+99].

To reduce the absorption, the gray-tracked crystal from the high-power longterm measurement in section 3.9.3 was heated to 135 °C for 97 h. It was subsequently integrated into the experiment again, and the mode matching was optimized. The monolithic design ensures that the relative position between induced absorption regions in the crystal and the cavity mode cannot change during this process; thus after mode matching, the laser travels exactly along the same cavity mode as before, and any change in the transmitted output power must be attributed to a change of absorption along the beam axis due to the annealing process. Figure 3.34 shows the oscilloscope traces at the crystal temperatures from figure 3.30, although recorded at 80 mW input power. The TEM_{00} modes are visible again and dominate the spectrum; this indicates that the optical losses have significantly been reduced.

Apparently, also the parametric gain profile was affected by the baking of the crystal: While before the longterm measurement, frequency conversion occurred only in a narrow temperature region about 1 K around the optimal phase-matching temperature, the recorded traces show that after the recovery, frequency conversion occurs both at a crystal temperature of 26 °C and 35 °C, with even a higher conversion efficiency at 26 °C. With this, up to 5 % total conversion are reached when the laser frequency is ramped, while only 3 % is converted at

35 °C. It seems plausible that the periodic poling of the crystal was damaged during the annealing, such that the domains are no longer as precisely separated as before. It seems worthwhile to study whether the absorption can also be removed at lower temperatures that do not harm the quasi-phase-matching poling period, so that the high effective nonlinearity of PPKTP is preserved while the intracavity losses are eliminated. This would enable the refurbishment degraded crystals and prolong the operational lifetime of monolithic SHG cavities.

3.10. Conclusion

The PPKTP-based monolithic SHG setup allows efficient generation of 400 nm-light. Internal conversion efficiencies of up to 80 % were inferred, and the SHG gain profile was characterized. Thermal feedback effects and cavity resonance drifts due to absorption of the generated harmonic 400 nm light were studied. The coupled degrees of freedom and the very low bandwidth of thermal feedback loops in the monolithic design limit the operability when a tunable laser frequency is required (i.e., to keep the input laser light resonant to some external cavity).

When converting 800 nm to 400 nm, grey tracking of the PPKTP crystal is a limiting factor for the applicability of monolithic SHG cavities as a tool in scientific experiments: the fast degradation does not allow longterm operation over many hours, days or even months on a constant performance level. Since the monolithic design allows exactly one TEM_{00} mode per crystal, a degraded cavity mode requires to change the entire crystal, although the gray tracking is localized to less than 100 µm from the optical axis; it remains to show whether the crystal can be refurbished using lower temperatures, to avoid a damaging of the periodic poling. To study this, the monolithic design brings the advantage that the well-defined cavity mode is not lost during the annealing process, but direct comparative measurements on the same mode are possible.

However, in the present setup, the monolithic SHG cavity allowed to supply sufficient amounts of 400 nm pump light for the generation of squeezed light in a monolithic optical parametric oscillator (OPO); this will be the subject of the next chapter.

4. Squeezing in an absorptive nonlinear medium

The main aim of the experiment is the generation and detection of squeezed states of light at 800 nm. This chapter will explain the experimental setup, present measurement results and discuss current experimental limitations.

4.1. Squeezing cavity parameters

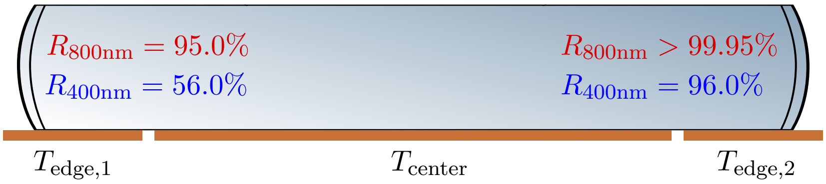

Figure 4.1.: OPO cavity design. The end mirrors are directly coated onto the end facets of a monolithic PPKTP crystal. The 400 nm pump light enters through the coupling mirror from the left and the squeezed vacuum leaves the cavity through the same mirror. The control beam at 800 nm is sent into the cavity from the right through the highly reflective mirror. The crystal is separated into three temperature regions, each powered by a separate Peltier element. Cavity dimensions and mode properties are identical to the SHG cavity from section 3.2.

The heart of the squeezing part of the experiment is an optical parametric oscillator (OPO), in which the squeezed light is generated via spontaneous parametric down-conversion (SPDC). The cavity design follows the same monolithic 3-temperature cavity design as the SHG cavity (see section 3.2). Crystal dimensions, material, poling period, radii of curvature, and consequently also beam waist radii are identical; only the reflectivities of input and output mirrors differ from the SHG cavity. The mirror reflectivities are 95 % / HR for 800 nm and 56 % / 96 % for 400 nm, yielding a simulated linewidth of 58.0 MHz and a finesse of 121.6 at 800 nm. For 400 nm, the low reflectivity of the coupling mirror leads to a calculated finesse of 10.0 in the absence of losses; however, the significant losses of around 18.6 %/cm at 400 nm [Wan+17] reduce the simulated finesse to 5.7 and lead to a broad linewidth of around 1.15 GHz for the 400 nm light.

4.2. Experimental setup

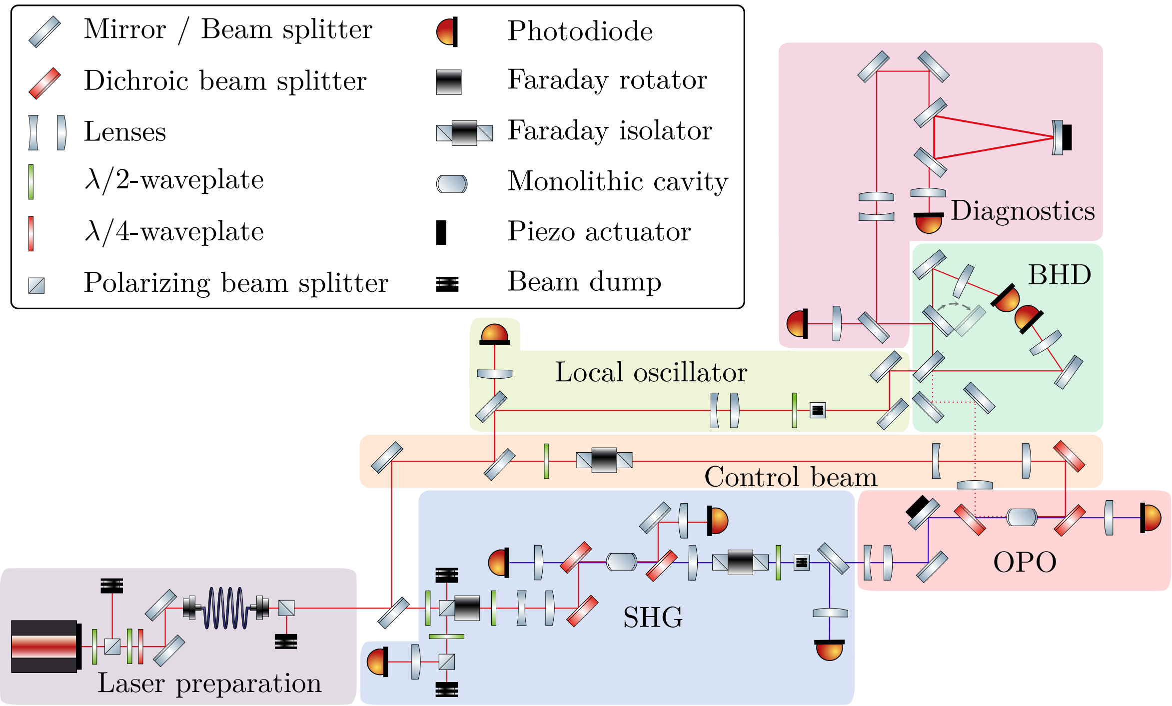

Figure 4.2.: Full experimental setup for the squeezing measurement. The laser is mode-cleaned in a polarization-maintaining optical fiber and split by a partially reflective mirror. Up to 200 mW of pump light are sent to the SHG section and converted to 400 nm pump light for the squeezing process in the OPO. Up to 350 mW can be sent as control beam through the HR side of the OPO. A local oscillator (LO) is picked off from the control beam, that can be overlapped with the light from the squeezing cavity on the 50:50 beam splitter of the balanced homodyne detector (BHD). The squeezing path is indicated with dashed lines. Both LO and squeezing path can separately be monitored on a photodiode and mode-matched to a diagnostic mode cleaner in the diagnostics section. Component icons by [Fra].

The full experimental setup for the squeezing measurement is displayed in figure 4.2. It consists of seven main parts: laser preparation, SHG, OPO, control beam, local oscillator (LO), balanced homodyne detector (BHD) and a diagnostics section.

As described in section 3.3, the output of the Toptica TA pro laser head is mode-cleaned by an optical fiber. The output beam is separated on a 70:30 beam splitter. While most of the light power is reflected off into the control beam, up to 200 mW of the 800 nm light can be sent into the SHG cavity, where it is converted to 400 nm. The transmitted 400 nm light passes a Faraday isolator and is mode-matched via lenses and mirrors to the OPO. The last reflective mirror in front of the OPO is a phase shifter, which allows to adjust the relative phase between the second-harmonic pump light and the local oscillator. To separate the 400 nm pump light from the 800 nm squeezing path, a dichroic beam splitter is placed immediately in front of the OPO.

For the control beam, powers of more than 300 mW are required to send it through the highly reflective mirror surface at the back of the OPO. To avoid back reflections into the laser, another Faraday isolator is placed in the control beam path. The little power that is transmitted through the OPO suffices to monitor the mode matching between control beam and OPO on a photodiode in the diagnostics section. In this way, the laser can also be locked to the OPO's resonance frequency. Due to the high finesse at 800 nm, the transmitted light from the control beam exits the OPO in a well defined mode. The light is reflected off the dichroic beam splitter towards the homodyne detector and the diagnostics section.

Around 20 mW of the control beam are picked off as a local oscillator (LO) for homodyne detection, and its power is stabilized by a feedback loop to the tapered amplifier current. To ensure a high interference contrast between local oscillator and the squeezing path, both are separately mode-matched to the same diagnostic mode cleaner (DMC). Here, the beam from the OPO is taken as a reference, since, in case of an angular adjustment of the homodyne beam splitter, no pointing is introduced into the beam path to the DMC. Once the mode matching between squeezing path and LO is established, the flip mirror to the diagnostics section can be removed. Now, due to the 50:50 splitting ratio of the homodyne detector, the same power is sent to each of both homodyne photodiodes. The AC difference signal between both photodiodes is displayed on a Rohde & Schwarz FSV3004 spectrum analyzer.

In a setup with two monolithic cavities, the laser can only be locked to one of them. Therefore, the laser was locked to the SHG cavity to obtain a stable pump for the OPO. As argued in section 3.7.1, locking the OPO via a temperature controller is not possible due to the thermal hysteresis effects. Resonance was therefore always achieved by manually reducing temperature in the OPO (see sections 4.5 and 3.7.1). Simultaneous resonance of the 400 nm pump light and the 800 nm control beam in the OPO can be reached by tuning of the SHG temperature, i.e., adjusting the laser frequency. The temperature controller also allows to ramp the OPO temperatures, which is required to match the modes of the fundamental and the harmonic beam in the OPO.

4.3. Mode matching SHG cavity to OPO

To obtain reasonable levels of squeezing, a good mode overlap between the 400 nm pump beam and the 800 nm OPO mode is required. The lens positions were calculated using the mode-matching software JamMt [TL]. For a coarse adjustment of beam position and angle, the intensity distribution leaving the OPO is observed on a screen: Due to the low reflectivity at 400 nm, a separate spot appears for each round trip. By overlapping these spots, the incoming beam is aligned to the optical axis of the cavity; in this case, circular interference pattern appear.

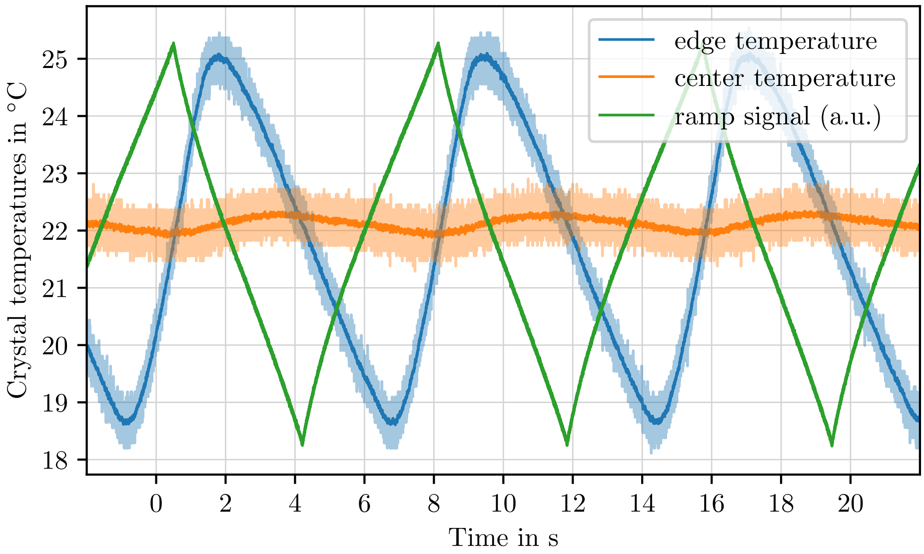

Figure 4.3.: Temperature ramp by heating/cooling the edge region of the OPO. The green signal is the modulating offset signal for the Peltier element, generated by the temperature controller. The actual NTC-temperature approximately follows the ramp signal. Rising ramp is steeper, since the heating power of the Peltier is higher than cooling power. The mean of the center temperature drifts by only 0.3 K due to the modulated edge temperature. The light colors show the fluctuation of the measurement data; the solid line is a rolling mean from 50 data points.

Once this level of adjustment is reached, a temperature ramp is applied to the edge temperature of the OPO to shift its resonance frequency with respect to the pump laser. Figure 4.3 shows the signal applied to the edge temperature and the corresponding measured temperatures by the NTC elements for the edge and center region. The crystal temperature follows the ramp signal with a delay of around 2 s. At the center, the ramp is approximately linear, with a higher gradient for increasing than for decreasing temperatures. From the orange trace, it can be inferred that a temperature ramp on the edge temperature imposes a tiny drift of 0.3 K on the center temperature.

Figure 4.4 shows that a variation of the edge temperature in the range of 40.3 – 43.7 °C covers three resonances and consequently more than two full FSRs of the cavity within one ramp of 2 s duration. The low repetition rate of 0.25 Hz and the asymmetry depending on the ramp direction impede a good mode matching between the pump beam and the TEM_{00} mode of the OPO. Furthermore, the low reflectivity of the coupling mirror of 56 % and the intracavity losses at 400 nm lead to very broad linewidths, that cannot be well separated from each other and lead to a significant residual transmission through the OPO, even when the cavity is not resonant. Figure 4.4 shows a lag of approximately 1.3 s between the crystal's set-temperature and the actual temperature at the bottom of the crystal, as well as an estimated lag of around 0.4 s from the temperature at the bottom of the crystal to the beam axis (since the resonances appear at different NTC temperatures on rising and falling ramp).

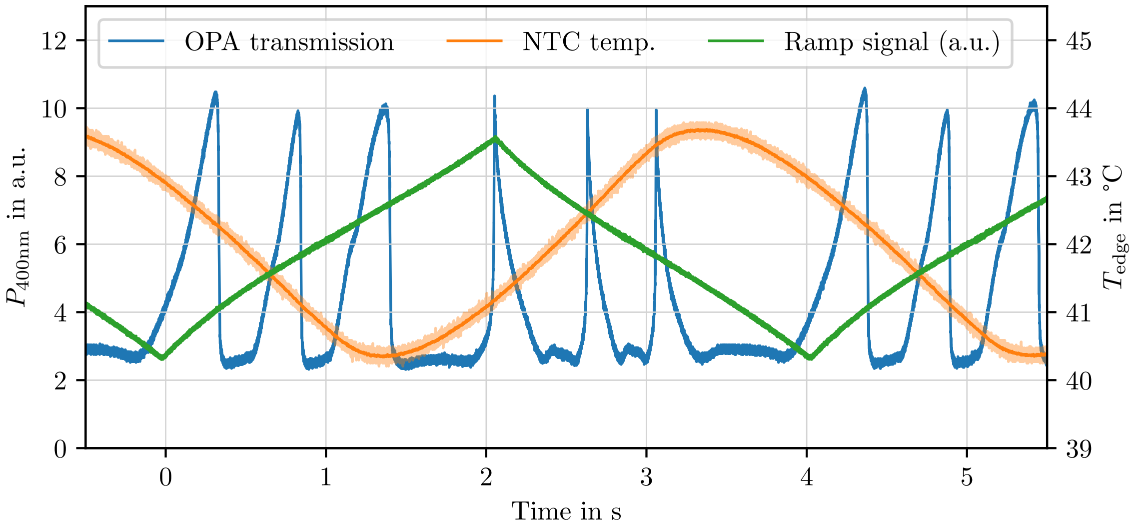

Figure 4.4.: Mode matching the SHG output beam to the OPO using a temperature ramp. The transmitted $P_{400\mathrm{nm}}$ behind the OPO (blue) is shown together with the ramp signal (green) and the temperature measured by the NTC at the bottom of the crystal (orange). The ramp covers three TEM_{00} resonances that appear strongly distorted depending on the ramp direction. The opaque orange line is a rolling mean of 50 data points.

Due to the low repetition rate, the effect from adjusting beam position and/or beam angle can only be seen seconds later – this limits the ability to fine-tune the mode matching using a temperature ramp. To overcome this, an alternative approach was used to optimize the mode overlap: The cavity was ramped, and the shape and interference fringes of the transmitted light were observed on a screen. From the symmetry of the interference fringes and the subjective relative brightness of the TEM_{00} mode, the mode matching could be optimized, which was then also verified via the oscilloscope trace. However, with the data presented in figure 4.4, it is not possible to reliably quantify the mode matching between pump beam and the squeezing mode.

4.4. Homodyne detection

As described in section 2.10, squeezed states of light can be conveniently measured with a balanced homodyne detector (BHD). It consists of a 50:50 beam splitter, where the squeezed light from one port and a local oscillator the other port are overlapped. Both output ports are detected by photodiodes and the photocurrents are subtracted from each other. In the resulting signal, the noise from the squeezed light field is amplified by the light power in the local oscillator path. The measurement is phase-sensitive, that means the quadrature, in which the noise is read out, can be chosen by adjusting the relative phases between the local oscillator and the light from the squeezing path. In the experiment, the phase can be shifted by a mirror placed on a piezo actuator that adjusts the optical path between SHG cavity and OPO by a few wavelengths.

4.4.1. Quantum efficiency of the photodiodes

Since squeezed states of light are very susceptible to optical losses, the losses must be minimized wherever possible. For the BHD, a high quantum efficiency of the photodiodes is required. For the desired wavelength around 800 nm, three silicon photodiodes from Hamamatsu were considered: S3883, S5971 and S5972. All of them have a reasonable value-for-money ratio and can be delivered with AR-coated windows or as a windowless model. The quantum efficiencies as specified by the manufacturer are listed in table 4.1. To avoid high expenses and long lead times, the standard S5971 photodiode was bought and the window cap was removed, since the windowless model was not on stock. The quantum efficiency was determined afterwards by measuring the photocurrent generated from a defined incident light power.

In the tested reverse voltage range between $0-20\,\mathrm{V}$, the quantum efficiency was constant. The incident light power was measured with a Thorlabs S130C power meter and the resulting quantum efficiency meets the manufacturer's specification almost exactly. The specified error of the power meter of 3% limits the accuracy of the quantum efficiency measurement.

In addition to the quantum efficiency under perpendicular incidence, the quantum efficiency was determined for light hitting the photodiode under angles between $0-30°$. It was hypothesized that around Brewster's angle the quantum efficiency could be increased even further. However, increasing the angle of incidence in horizontal and vertical orientation did not increase the quantum efficiency. The photodiodes were therefore used with illumination perpendicular to their surface.

Model	QE (with windows)	QE (w/o windows)	measured
S3883		95.5%	
S5971	88.0%	97.7%	97.5% (w/o windows)
S5972		94.3%	87.2% (with windows)

Table 4.1.: Specified and measured quantum efficiencies (QE) of different Hamamatsu silicon photodiode models.

4.4.2. Linearity of the homodyne detector

To obtain reliable squeezing measurements, the homodyne detector must be shot noise limited. In this case, a doubling of the local oscillator power increases the noise level by +3 dB (whilst classical noises increase the noise level by +6 dB upon doubling of the LO power). From figure 4.5, it can be seen that the homodyne detector is shot noise limited up to 2 mW for frequencies up to 500 kHz, while the it saturates for higher frequencies. In the frequency region between 0.05 – 5 MHz, the detector responds linear to input powers between 0.03125 – 0.5 mW. For the linearity measurement, the dark noise was subtracted from each trace and the noise was normalized to the noise at 0.125 mW LO power.

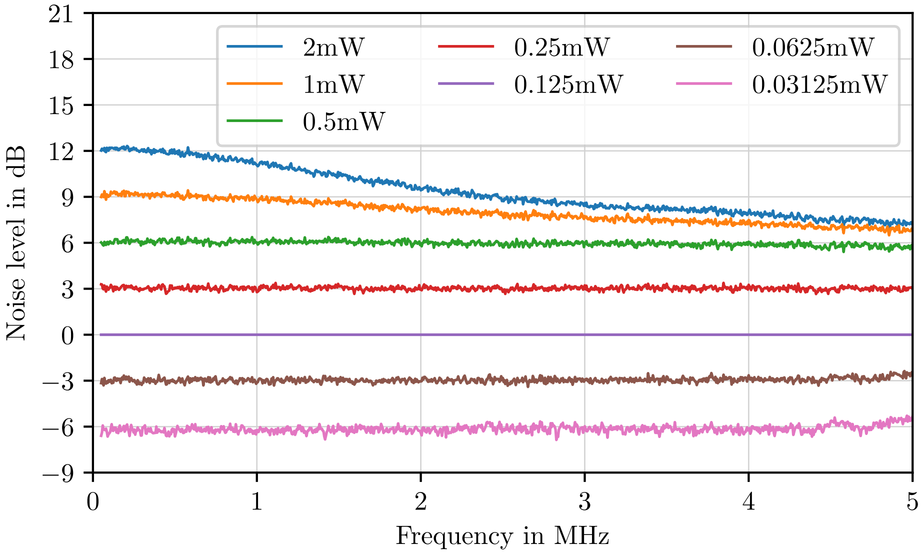

Figure 4.5.: Linearity of the homodyne detector (dark noise corrected). Doubling the LO power increases the noise level by +3 dB for powers up to 0.5 mW over a frequency range from 0.05 – 5 MHz. For frequencies from 50 – 500 kHz, the detector behaves linear for local oscillator powers up to 2 mW.

4.4.3. Mode matching squeezing and local oscillator path

The homodyne detection requires a good mode overlap between the local oscillator beam (LO) and the mode carrying the squeezed light on the 50:50 beam splitter. To achieve this, both modes are matched onto the same mode of a triangular diagnostic mode cleaner (DMC), which ensures the mutual overlap of both modes also at the homodyne beam splitter.

First, the OPO mode is matched to the DMC. To do so, the laser is locked to the OPO. The 800 nm light that enters the cavity is now in the cavity's TEM_{00} mode and leaves the

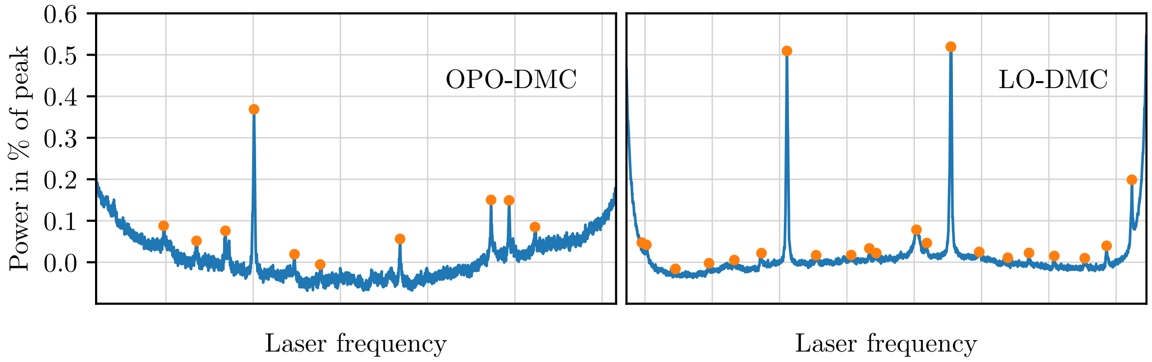

Figure 4.6.: Mode matchings from OPO (left) and local oscillator (right) to the DMC. The plots show the residual modes within one FSR that have been used to calculate the mode matching. The magnitude is given in % of the TEM_{00} peak (which is cut off on both sides of the plots).

cavity in the same mode as the squeezed light. By adjusting the mirrors and lenses in front of the DMC, it can be brought to spatial overlap with the fundamental mode of the DMC. This is monitored by ramping the length of the DMC via a piezo actuator and detecting the transmitted light on a photodiode. The DMC separates different TEM-modes from one another, since the Gouy-phase enforces resonance at different frequencies for fundamental and higher order modes. When the mode matching is optimized, close to 100 % of the power is transmitted when the cavity becomes resonant for the TEM_{00} mode and all other modes carry negligible power. The mode-matching efficiency is defined by

$$\eta_{\mathrm{MM}} = \frac{P_{\mathrm{max},00}}{\Sigma_i P_{\mathrm{max},i}}, \tag{4.1}$$

where the summation in the denominator runs over the peak powers $P_{\mathrm{max},i}$ of all cavity resonances above the noise threshold and $P_{\mathrm{max},00}$ denotes the peak power in the TEM_{00} mode. To reduce the noise offset, the acquisition mode of the oscilloscope was set to 4x averaging; this allowed to detect higher order modes that would otherwise be hidden in the noise floor. The left part of figure 4.6 shows a full FSR between two TEM_{00} resonances, recorded in transmission of the DMC. For the measurement presented in the following sections, the mode matching between the squeezed mode from the OPO and DMC was $\eta_{\mathrm{MM}}^{\text{OPO-DMC}} = 99.0\,\%$.

Next, the mode matching from the local oscillator (LO) to the DMC was optimized using only the lenses and mirrors in the LO path (without moving any optical elements after the homodyne's beam splitter). The mode matching in the LO path was brought to a moderate overlap of $\eta_{\mathrm{MM}}^{\text{LO-DMC}} = 97.9\,\%$. The corresponding residual modes are shown on the right side of figure 4.6.

From these two values, a lower bound can be estimated for the mode matching: While in the best case, the deviation from the DMC mode goes in the same direction and the mode-matching efficiency $\eta_{\mathrm{MM}}^{\text{OPO-LO}}$ may be better than each mode matching to the DMC separately, in the worst case, the deviations from the DMC mode are in different directions. In this case, both single mode-matching efficiencies are multiplied to yield a lower bound for the mode-matching efficiency between squeezing beam path and LO:

$$\eta_{\mathrm{MM}} \equiv \eta_{\mathrm{MM}}^{\text{OPO-LO}} = \eta_{\mathrm{MM}}^{\text{OPO-DMC}} \cdot \eta_{\mathrm{MM}}^{\text{LO-DMC}} = 0.99 \cdot 0.979 = 96.85\,\% \tag{4.2}$$

The mode-matching efficiency quantifies the overlap of the spatial amplitudes; however, to estimate the visibility on the homodyne detector, the amplitude overlap must be squared to obtain powers (and determine losses in the further evaluation). Thus, up to $1 - \eta_{\mathrm{MM}}^2 = 6.2\,\%$ of optical losses must be expected from the imperfect mode overlap between the squeezing mode and the local oscillator.

4.5. Classical parametric gain and obtaining double resonance

The squeezing measurement requires simultaneous resonance both for the fundamental and the pump wavelength. Additionally, the phase-matching condition must be satisfied (i.e., the crystal temperature must be within a narrow temperature region). Once these three conditions are met, the vacuum field at 800 nm is squeezed. However, realizing these conditions simultaneously is not straight forward in a design with monolithic SHG and monolithic OPO.

The resonance for the 400 nm pump light can be easily monitored by a photodiode in transmission to the OPO. To ensure resonance of the OPO for 800 nm, a control beam at 800 nm is sent through its highly reflective backside and monitored by the photodiode in the diagnostic section. With both beams present in the cavity, the control beam also allows to verify the correct phase-matching temperature: If the phase-matching condition is satisfied, the classical control beam is periodically (de)amplified inside the OPO when the relative phase between pump and control beam is ramped; this is shown in figure 4.7 and will be discussed further below.

To obtain double resonance, the laser is locked to the SHG cavity, whose crystal temperatures are set to optimize output power in transmission. The OPO's crystal temperatures are set to the optimal phase-matching temperature, which is, in this case, approximately equal to the SHG temperatures. By tuning either of the OPO crystal temperatures, the OPO can be brought to resonance with the incident laser beams; however, in general, 400 nm and 800 nm do not become resonant at the same temperature, and not even a combination of three different OPO temperatures can enforce simultaneous resonance of these wavelengths.

Since the harmonic pump and the fundamental wavelength have different $\mathrm{d}n/\mathrm{d}T$, their resonance frequencies undergo different shifts when the laser frequency is changed. As the laser is locked to the SHG cavity, this is achieved by small adjustments of the SHG crystal's edge temperature, such that the fundamental and harmonic frequencies can be shifted towards each other without severely impacting on the conversion efficiency. In this way, 400 nm and 800 nm can be brought to mutual resonance for arbitrary OPO temperatures.

When the SHG temperature for double resonance is found, for stable operation of the OPO the resonance must be approached by reducing the crystal temperature (as discussed in section 3.7.1). Since the linewidth of the 400 nm light is much broader than the 800 nm light, the blue light becomes resonant first and the narrow linewidth at 800 nm becomes resonant only at slightly lower temperatures. Since part of the 400 nm pump light is absorbed in the cavity and contributes to the temperature budget, it is important that the resonance is not lost, since otherwise, the resonance and heating breaks down. Usually, several attempts were required to find a stable point of operation where the cavity was resonant for both wavelengths, while also being sufficiently far away from the point where the resonance of the pump beam collapses.

Once a double resonance is realized, it must be tested that the phase-matching condition is satisfied in the OPO for the given combination of wavelengths and temperatures. Figure 4.7 shows the power of the control beam in transmission of the OPO when the phase-matching condition is satisfied and the phase of the pump beam is ramped by the piezo actuator in front of the cavity. The parametric process leads to a phase-dependent exchange of energy between both beams and, consequently, a periodic amplification/deamplification of the photodiode signal when the phase is ramped. For high parametric gain, the deamplification reduces the transmitted 800 nm power to almost zero, even though the cavity is resonant with both wavelengths all the time. In figure 4.7, the phase was increased from $5.1 - 5.6$ s and decreased from $5.6 - 6.1$ s. The asymmetry with respect to the ramp direction originates from the fact that, when more 400 nm light is present in the OPO and gets absorbed, the heating induces an additional phase shift due to the temperature-dependent refractive index $\mathrm{d}n/\mathrm{d}T$. This phase shift is independent of the ramp direction and accelerates the rising ramp while counteracting the effect of the falling ramp.

The transmitted power at zero gain can be calculated from $P_{\max} = P_0 e^{2r}$ and $P_{\min} = P_0 e^{-2r}$ as $P_0 = \sqrt{P_{\max} \cdot P_{\min}}$. Figure 4.7 was normalized to this value. It was not possible to determine P_0 experimentally, since a blocking of the pump beam would also change the resonance condition of the cavity for the 800 nm control beam. A gain parameter of $r = 0.66$ can be deduced from the measurement, corresponding to a logarithmic (de)amplification by 5.7 dB. This parameter is directly linked to the levels of squeezing and anti-squeezing that can be achieved under the given conditions, since they are generated from the same parametric process: when the control beam is blocked, the parametric process (de)amplifies the vacuum noises at 800 nm by the same factor.

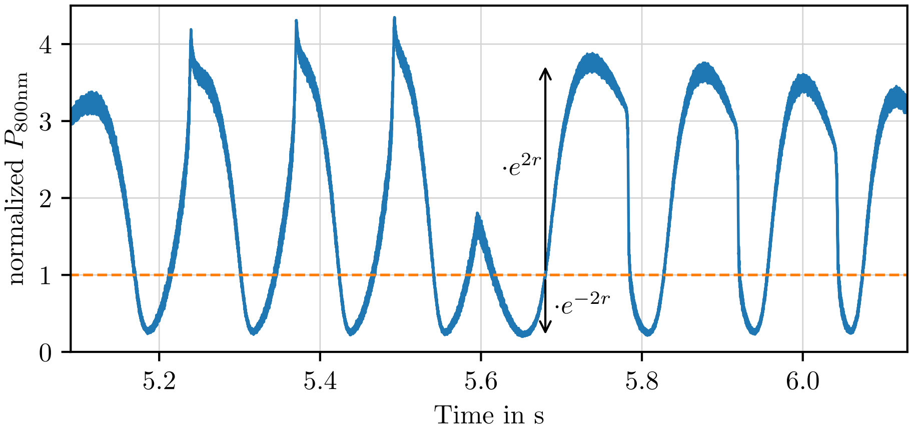

Figure 4.7.: Classical parametric gain as found when reaching double resonance. The transmitted 800 nm control beam gets periodically (de)amplified when the phase between pump and control beam is ramped. The relative phase increases from 5.1 − 5.6 s and decreases from 5.6 − 6.1 s. The varying 400 nm intracavity power leads to an additional contribution dn/T to the phase shift, that causes the asymmetry between rising and falling ramp. The power is normalized to the theoretically expected transmitted power in the absence of conversion. The maxima and minima correspond to $r \approx 0.66$.

From the procedure described above, it becomes apparent that finding the correct operating conditions in this system is also a matter of luck: If double resonance was established on a resonance for which the crystal temperature is too far off the phase-matching condition, this resonance will only allow to achieve very moderate levels of parametric gain. Unfortunately, a systematic approach to achieve double resonance with the correct combination of resonances, while also satisfying the phase-matching condition, could not be found. However, once a double-resonant configuration with high classical parametric gain is realized, the control beam can be blocked and the flip mirror in the diagnostics section can be removed. Since classical amplitudes at 800 nm are now no longer incident on the OPO, the vacuum state at 800 nm is modulated to a squeezed state, that can be monitored by the homodyne detector.

4.6. Squeezing measurement

Figure 4.8 shows the highest squeezing level obtained in the experiment. It was recorded at a pump power of 16 mW at a sideband frequency of 500 kHz with a local oscillator power of 2 mW; for this frequency and power, a linear response of the homodyne detector had been verified in section 4.4.2. Dark noise corrected, 4.03 dB of squeezing were achieved at an antisqueezing level of 7.98 dB. The phase ramp increases in the first second and decreases in the second half of the plot. One can see that, at the upper end of the ramp, both squeezing and antisqueezing values yield higher absolute values than at the lower end of the ramp.

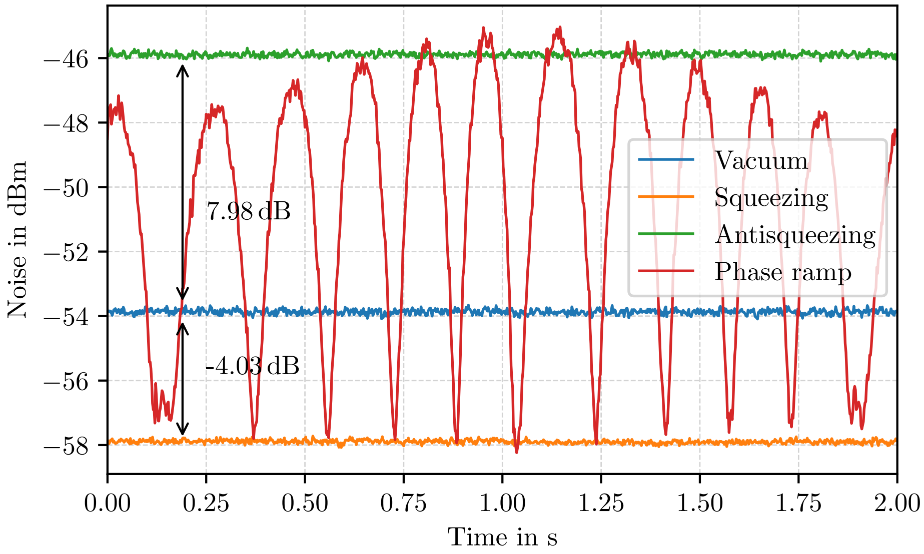

Figure 4.8.: Zero-span squeezing measurement at a sideband frequency of 500 kHz. For the red line, the homodyne readout phase ϑ was ramped (rising ramp from 0.14 − 1.03 s, falling ramp from 1.03 − 1.92 s. The displayed squeezed and antisqueezed noise levels belong to successive extrema, that is $\Delta\vartheta = \pi$. The measurement was recorded at a LO power of 2 mW with a resolution bandwidth of 100 kHz and a video bandwidth of 100 Hz.

This effect can be explained by a pointing introduced by the phase shifter, which reduces the spatial overlap between the pump light and the squeezing cavity mode at the lower end of the ramp. However, the results remain consistent in that the combination of squeezing and antisqueezing values can be well described by an OPO with reduced pump power.

The traces for squeezing and antisqueezing show the phase stability of the system, since they were not locked. The phase was adjusted by hand and stayed there for more than the displayed measurement time. To reach this phase stability, the laser table is covered with a housing that prevents phase noise due to air fluctuations. The traces for squeezing and antisqueezing belong to two neighboring minima/maxima, which suggests that they do not belong to the center of the plot, but rather to the parametric gain that is realized between 1.25 s and 1.35 s.

In the lossless case and in the absence of phase noise, one would expect to have the same amount of squeezing and antisqueezing. It can be seen from figure 4.8 that this is clearly not the case in the studied setup. From the squeezing and antisqueezing levels, the losses can be estimated by eq. (2.68). For the average values from figure 4.8, the calculated losses are 31.8 %. Other squeezing measurements with lower or higher parametric gain (and consequently varying squeezing and antisqueezing levels) all yielded loss estimations in the range 32 − 40 %. Even for infinite initial squeezing, these losses would limit the detectable squeezing to no more than 4.04 − 4.97 dB.

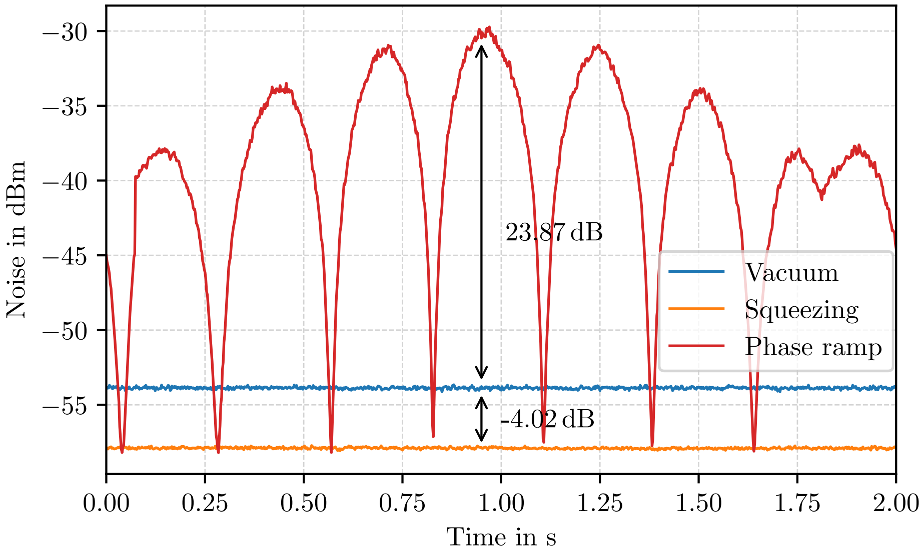

Figure 4.9.: Zero-span squeezing measurement at a sideband frequency of 500 kHz similar to figure 4.8 with more than 23 dB of antisqueezing (dark-noise corrected). Rising phase from 0.08 − 0.94 s and falling phase from 0.94 − 1.8 s. The measurement was recorded at a LO power of 2 mW with a resolution bandwidth of 100 kHz and a video bandwidth of 100 Hz.

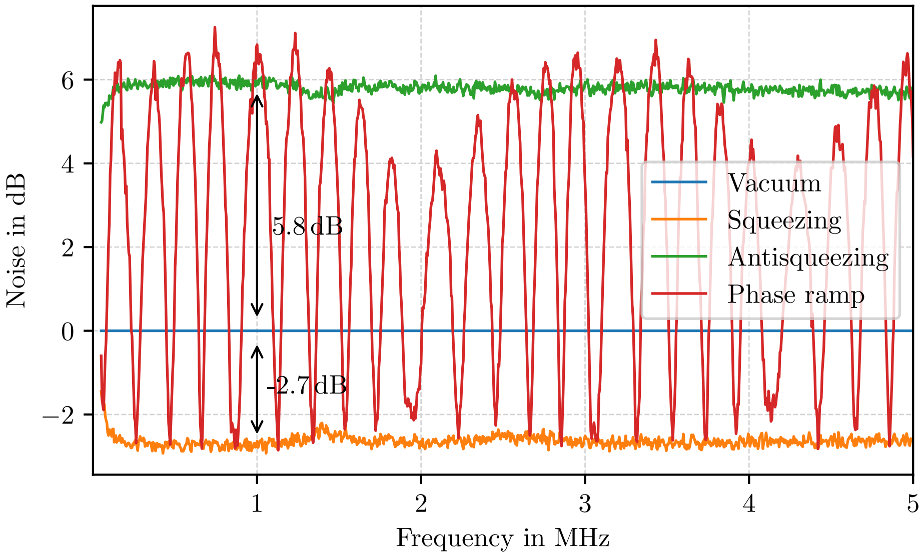

Figure 4.10.: Squeezing spectrum for sideband frequencies from 50 kHz to 5 MHz, normalized to the vacuum noise level (not dark-noise corrected). For the red trace, the homodyne readout phase ϑ was ramped simultaneously to the sideband frequency sweep. The measurement was recorded at a LO power of 171 µW with a resolution bandwidth of 100 kHz and a video bandwidth of 100 Hz.

Figure 4.9 demonstrates that closer to the OPO threshold, the antisqueezing ranges between 15 − 23 dB (again due to a pointing of the pump beam and consequently varying effective pump power), while the squeezing level remains constant around 4 dB; this is due to the fact that, in a loss-limited OPO, the antisqueezing level increases strongly when the pump power approaches the OPO threshold, while the squeezing level does not. From the measured squeezing and antisqueezing levels, 39.5 % losses can be inferred from eq. (2.68). These increased losses may originate from increased intracavity losses (since the measurement from figure 4.9 was performed after the measurement in figure 4.8) or from minimal amounts of phase noise, that also gains impact at higher squeezing levels. The magnitude of phase noise could not be quantified, since this is usually obtained from a fit versus different pump powers; however, an independent tuning of this variable is not possible in an absorptive monolithic OPO without changing also the resonance condition of the cavity.

In figure 4.10, the noise spectrum was recorded at sideband frequencies ranging from 50 kHz to 5 MHz at a local oscillator power of 171 µW. For the red trace, the phase ramp was applied during the sideband frequency sweep; the pointing effect due to the phase ramp leads to a decreased parametric gain around 2 MHz and 4.2 MHz. Since the acquired sideband frequency range lies well within the linewidth of the OPO, the constant squeezing/antisqueezing levels are in agreement with the theoretical expectations.

4.7. Loss analysis

4.7.1. Detection (in)efficiencies

To understand the origin of the optical losses, each possible loss source was studied separately. The total detection efficiency is the product

$$\eta = \eta_{\mathrm{MM}}^2 \cdot \eta_{\mathrm{QE}} \cdot \eta_{\mathrm{trans}} \cdot \eta_{\mathrm{esc}}, \tag{4.3}$$

where $\eta_{\mathrm{MM}} = 0.97$ is the mode-matching efficiency from eq. (4.2), $\eta_{\mathrm{QE}} = 0.97$ is the quantum efficiency of the photodiodes used in the homodyne detector from section 4.4.1, η_{trans} is the transport efficiency between the OPO and the homodyne detector, and η_{esc} is the escape efficiency of the OPO. The path between squeezer and photodiodes leads over four mirrors (highly reflective for 800 nm), through two lenses (anti-reflex coated for 800 nm) and through the coating of the 50:50 beam splitter. Due to the high quality of the coatings and super-polished mirror surfaces, the transport efficiency is assumed to be around $\eta_{\mathrm{trans}} \geq 0.98$. The escape efficiency $\eta_{\mathrm{esc}} = \frac{T}{T+L}$ depends on the power transmissivity of the coupling mirror $T = 0.05$ and all other intracavity losses per round trip L (i.e., transmission through the highly reflective mirror end mirror of the OPO and absorption inside the crystal). The transmission through the end mirror is specified to be $< 0.05\,\%$. For the absorption losses in

Component	efficiency η
mode matching OPO–LO	97 %
Quantum efficiency of PDs	97 %
Transport efficiency	98 %
Escape efficiency (non-degraded)	$\geq$ 98.4 %
Total (non-degraded)	$\geq$ 88.0 %

Table 4.2.: Estimation of overall detection efficiency for a non-degraded crystal

PPKTP, different values have been reported for 795 nm (see section 3.1) – among them an absorption coefficient as low as 0.013 %/cm [Ste+13], corresponding to intracavity absorption of 0.03 % and consequently total intracavity losses $L = 0.0008$. This should allow for an escape efficiency $\eta_{\text{esc}} \geq 98.4\,\%$. All together, this yields a product of $\eta \geq 88.0\,\%$, which means that at most 12.0 % of losses can be explained by these detection inefficiencies. This yields a significant discrepancy from the 30 − 40 % losses inferred from the squeezing measurements.

Most of the loss sources are not expected to change significantly over time. The quantum efficiency may decrease slightly over time due to oxidation after the windows have been removed; however, with previous photodiodes, a degradation of 1 − 2 % was observed after several weeks of experiments. The PDs were changed few days before the squeezing measurements, and thus a possible degeneration cannot account for the additional losses. Lenses and mirrors were checked for dust particles, but no loss sources could be identified; in fact, greasy films or dust particles would also distort the beam shape and would not allow a mode matching of 97 %. This leaves two possible explanations: The mode-matching efficiency η_{MM} may decrease in the presence of the 400 nm pump light and an accompanying thermal lens inside the cavity. Alternatively, increased intracavity losses at the squeezing wavelength 800 nm could reduce the escape efficiency η_{esc} below the assumed value.

4.7.2. Thermal lensing hypothesis

Due to the relatively strong absorption of 400 nm light, it is a reasonable hypothesis that thermal lensing effects decrease the mode matching between the OPO and the local oscillator. Since η_{MM} enters squared in the detection efficiency, already moderate thermal lensing effects could lead to a significant increase of the losses. A thermal lens would change the focal position of the squeezed light and thereby decrease the mode overlap between OPO and local oscillator, since this was optimized with only the 800 nm light in the cavity. To account for the losses, the mode matching efficiency would have to reduce to the order of

$$\eta^*_{\text{MM}} = \sqrt{\frac{\eta}{\eta_{\text{QE}} \cdot \eta_{\text{trans}} \cdot \eta_{\text{esc}}}} = 83\,\%, \tag{4.4}$$

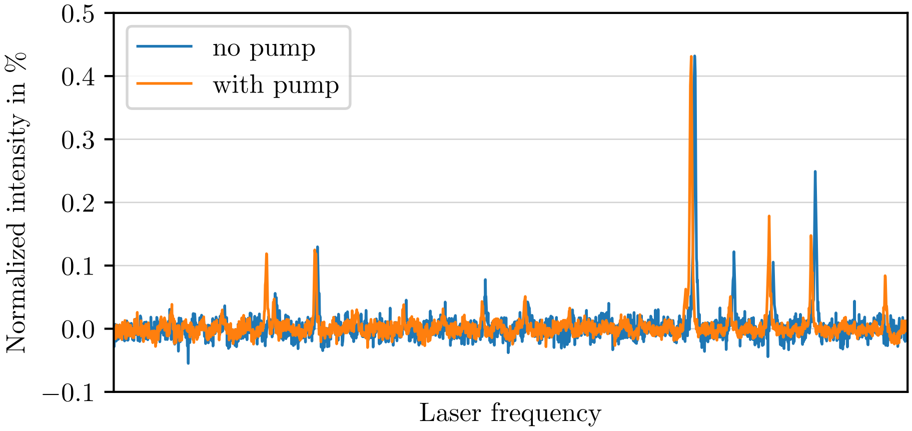

Figure 4.11.: Mode matching from OPO to the diagnostic mode cleaner (DMC) in the absence of pump light and with 16 mW pump power incident on the OPO. The data shows one FSR excluding both TEM_{00} resonances on the edges. The intensity is normed to the peak intensity of TEM_{00}. The mode matching changes from 98.6 % without pump light (blue) to 98.7 % in the presence of 400 nm pump light in the cavity.

with $\eta \approx 0.65$ (according to 35 % overall losses) and the other efficiencies according to table 4.2. Due to the significance of the predicted deviation of the mode matching in the presence of the pump light, this hypothesis can conveniently be tested in the experiment.

The mode matching from the OPO to the DMC was measured with and without the 400 nm pump light present in the cavity; the measurement was performed at an input power of 16 mW, as used in the squeezing measurement. The OPO temperature was detuned from the phase-matching temperature to avoid parametric amplification and phase-dependent output powers. The DMC cavity was ramped. As for the squeezing measurements, the laser was locked to the SHG cavity and double resonance of the OPO was achieved according to the procedure described in section 4.5. Since in this configuration, power fluctuations of the transmitted 800 nm light are possible due to slight drifts of the OPO's resonance frequency, the signal behind the DMC was normalized to the power that is transmitted through the OPO and recorded on the photodiode in the diagnostic section. Due to the broad linewidth at 400 nm, the pump light intensity was not susceptible to drifts of the OPO's resonance frequency. After a double resonance was found, the 400 nm light was blocked and the mode matching was recorded with the control beam at 800 nm alone. After this, the pump light was unblocked, the cavity was brought to double-resonance, and the spectrum on the ramped DMC was recorded again.

The results are shown in figure 4.11. The plotted signals are corrected for some DMC-phase dependent offset voltage that supposedly originates from electronic influence of the small photodiode signal by the high voltage driving the DMC's piezo actuator right next to it;

to normalize this offset to zero, a rolling median of the neighboring 100 data points was subtracted from the data. It must be noted that the same qualitative information can be read off without the correction; however, for a reliable calculation of the mode matching and a direct comparison of both traces, it turns out handy when the baseline does not deviate too much from 0.

The intensity of the resonance peaks in figure 4.11 are normalized to the peak intensity of the TEM_{00} mode. The mode-matching efficiencies are calculated according to eq. (4.1). This procedure yields a mode-matching efficiency of 98.6 % without pump light and 98.7 % in the presence of pump light; consequently no significant change in mode matching could be detected. The biggest higher order mode (with 0.43 % of the TEM_{00} mode) remains unchanged and only some of the even smaller higher order modes modes change in magnitude. This effect is orders of magnitude too small to explain the reduced squeezing levels and rules out the thermal lensing hypothesis.

4.7.3. Increased intracavity losses

Hence, only the escape efficiency $\eta_{\mathrm{esc}} = \frac{T}{T+L}$ remains as a candidate to explain the squeezing losses. The mirror transmissivity $T = 0.05$ is fixed, but from the gray tracking observed in the SHG crystal (see section 3.9.2), it seems reasonable that the 400 nm pump light may introduce additional optical losses also at 800 nm. Due to the high reflectivity of the coupling mirror, already a small absorption coefficient α suffices to significantly decrease the escape efficiency, as shown in table 4.3. The table neglects the transmission through the highly reflective mirror and calculates the round trip losses from the absorption coefficient α as $L = 1 - e^{-\alpha l}$ with the round trip length $l = 2 \cdot 1.156\,\mathrm{cm}$. Furthermore, the corresponding cavity linewidths were fitted in the interferometer simulation software FINESSE [BF14]. Table 4.3 also lists the corresponding escape efficiencies η_{esc}, the overall losses $1 - \eta_{\mathrm{tot}}$ (calculated according to eq. (4.3) with all other efficiencies according to table 4.2), and in the last column the theoretically maximal achievable squeezing level in a system subject to the calculated overall losses. From the squeezing measurement in figure 4.8, overall losses of $1 - \eta_{\mathrm{tot}} \approx 32\,\%$ were inferred (see section 4.6); according to table 4.3, these overall losses correspond to $\alpha \approx 0.7\,\%/\mathrm{cm}$. The increased intracavity losses should then lead to a linewidth broadening to 74.8 MHz. This is again a prediction that can well be tested experimentally.

4.7.4. Linewidth measurements

For the evaluations in section 3.7 and 3.8, a linear relationship between the voltage of the piezo actuator and resulting laser frequency was assumed; the calibration factor was obtained from averaging the piezo voltage differences between neighboring TEM_{00} resonances on the ramp and relating this to the known FSR of 7.034 MHz. The actual nonlinear response of

$\alpha_{800\mathrm{nm}}$ in $\frac{\%}{\mathrm{cm}}$	L in %	γ in MHz	$\eta_{\mathrm{esc}} = \frac{T}{T+L}$	$1 - \eta_{\mathrm{tot}}$ in %	Max. Sqz. in dB
0.05	0.12	57.9	0.977	12.6	8.71
0.10	0.23	59.2	0.956	14.5	8.14
0.15	0.35	60.5	0.935	16.4	7.65
0.20	0.46	61.8	0.916	18.1	7.23
0.25	0.58	63.1	0.897	19.8	6.86
0.30	0.69	64.4	0.879	21.4	6.54
0.35	0.81	65.7	0.861	23.0	6.24
0.40	0.92	67.0	0.845	24.5	5.98
0.45	1.04	68.3	0.829	25.9	5.74
0.50	1.15	69.6	0.813	27.3	5.53
0.55	1.26	70.9	0.798	28.6	5.33
0.60	1.38	72.2	0.784	29.9	5.15
0.65	1.49	73.5	0.770	31.1	4.98
0.70	1.61	74.8	0.757	32.3	4.82
0.75	1.72	76.1	0.744	33.4	4.67
0.80	1.83	77.3	0.732	34.5	4.53
0.85	1.95	78.6	0.720	35.6	4.41
0.90	2.06	79.9	0.708	36.6	4.28
0.95	2.17	81.2	0.697	37.6	4.17
1.00	2.29	82.5	0.686	38.6	4.06

Table 4.3.: Simulated intracavity losses L, cavity linewidth γ, escape efficiency η_{esc}, overall losses $1-\eta_{\mathrm{tot}}$ and achievable squeezing level versus absorption coefficient $\alpha_{800\mathrm{nm}}$. The coupling mirror transmissivity is $T = 5\%$. The total losses $1-\eta_{\mathrm{tot}}$ are calculated from equation eq. (4.3) with $\eta_{\mathrm{MM}} = \eta_{\mathrm{QE}} = 0.97$ and $\eta_{\mathrm{trans}} = 0.98$. The round trip losses L are calculated by $L = 1 - e^{-\alpha l}$ with the round trip length $l = 2.3\,\mathrm{cm}$. The theoretically achievable squeezing levels are calculated from the overall losses $1 - \eta_{\mathrm{tot}}$ and eq. (2.67).

the piezo actuator yielded a systematic error of 5 − 8 % that was acceptable to qualitatively describe the behavior of the system. However, for a quantitative linewidth measurement, these errors are no longer acceptable and impede reliable results.

Figure 4.12 shows a ramp of the piezo actuator covering more than three FSRs and, thus, four cavity resonances. The repetition rate was 25 Hz. Hysteresis effects are clearly visible: independent of rising or falling ramp, the frequency offset per applied voltage is higher at the beginning of the ramp and decreases towards the end of the ramp, as can be seen from the unequal spacing of the cavity resonances. This effect also leads to the observation that the same cavity resonance does not appear at the same piezo voltage on rising and falling ramp. The magnitude of the hysteresis effect depends on the frequency range that is covered by the ramp. Therefore, for a more precise evaluation of the linewidth, it was necessary to assign individual calibration factors between piezo voltage and laser frequency to each resonance.

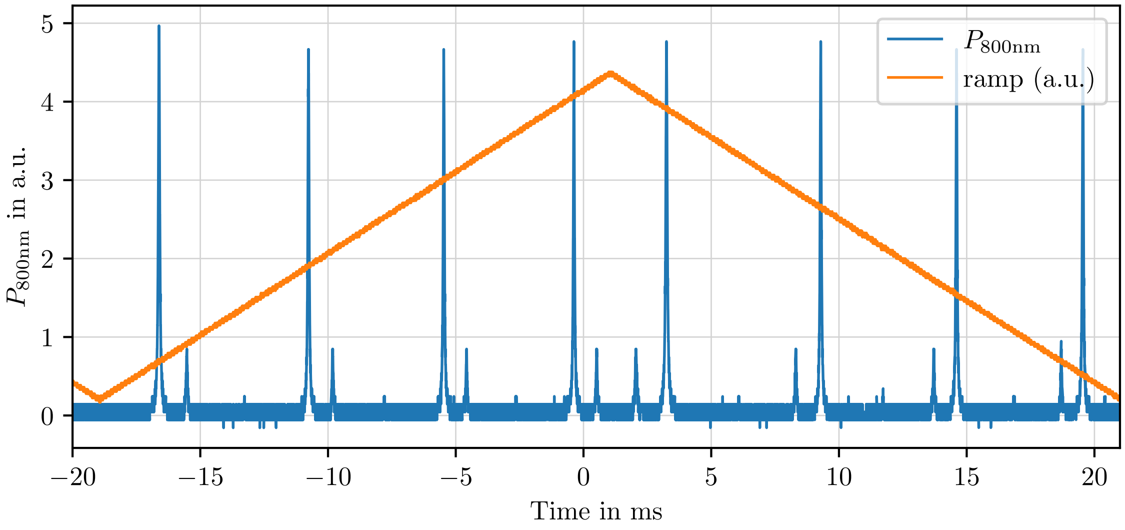

Figure 4.12.: Exemplary trace for the OPO linewidth measurement. The measurement clearly shows the nonlinearity between piezo voltage (orange) and laser frequency: at the beginning of the ramp, the cavity resonances are separated further than at the end of the ramp. To account for this nonlinearity, the two resonances in the center of the ramp were fitted against time and converted to frequency by applying individual calibration factors for each resonance that were obtained from the average of both adjacent FSRs.

To obtain the linewidth of the OPO from figure 4.12, each of the resonances was fitted with a Lorentzian versus the acquisition time. For each two successive TEM_{00} resonances, the distance in time domain was evaluated, and with the known FSR of 7.034 MHz, a local calibration factor was assigned for each FSR. For the resonances in the center of the ramp, an average calibration factor was calculated from both neighboring FSRs. Calibrating the results from the fits in time domain with the individual calibration factors yielded very good agreement between the linewidths on different positions on the ramp and between the linewidths on rising and falling ramp. Four ramp cycles like the one presented in figure 4.12 were recorded, such that in total 16 resonances in the center of the ramp could be evaluated, yielding an average linewidth $\gamma = (74.24 \pm 0.59)\,\text{MHz}$. The given error is the statistical error, which outnumbers the errors of the fits, ranging on the order of few kHz. According to table 4.3, these linewidths correspond to $\alpha_{800\text{nm}} \approx 0.7\,\%/\text{cm}$ and (together with all other quantified loss sources) to overall optical losses of $\approx 32.3\,\%$. This is in excellent agreement with the loss estimation from the squeezing measurement in figure 4.8.

The measurement presented above was performed four weeks after the squeezing measurement and one day after the thermal lensing test presented in section 4.7.2. To quantify the recovery of the intracavity losses, the crystal was not illuminated after the linewidth measurement for 12.5 months; afterwards (and still in the absence of pump light), a similar measurement and evaluation was performed on eight resonances of one ramp cycle, of which the four linewidths in the center of the ramps were fitted and averaged to (68.77 ± 0.37) MHz. According to table 4.3, this corresponds to a reduction of $\alpha_{800\mathrm{nm}}$ by 34 % to ≈ 0.46 %/cm and consequently a reduction of the overall losses down to 26.2 % within one year without illumination and storage at room temperature.

4.7.5. Comparison with other experiments

The estimated intracavity losses from the squeezing measurements seem plausible when comparing with other gray-tracking studies: Boulanger *et al.* saturated the absorption losses in a KTP crystal with 532 nm light of different polarization and recorded the reduced transmissivity over the whole visible spectrum. Their measurement shows that a saturation of the color centers reduces the transmissivity of the 8 mm long crystal at 800 nm by 1 − 2 % compared to the non-irradiated transmissivity [Bou+99]. These losses are on the order of the absorption losses inferred from the limited squeezing levels in the measurement from figure 4.8 and the corresponding linewidth measurements.

The loss levels are also in a plausible range when comparing with Han *et al.*, who measured the absorption for a single trip through a 15 mm long PPKTP crystal to increase from 0.4 % to 1.0 % after illumination with 84 mW of 397.5 nm cw-light for only 60 seconds [Han+16]. Supposedly, after this short time, the saturation was not yet reached. Due to a broader waist size and no external cavity for the 400 nm pump light, the intensity in their experiment was approximately equal to the pump light intensity in the squeezing measurement.

All in all, it can be concluded that the squeezing and linewidth measurements yield a coherent picture: the detectable squeezing level is limited by increased intracavity losses at 800 nm due to gray tracking by the 400 nm pump beam. This limitation has also been reported by other squeezing experiments operating at 795 nm [Hon+08; Han+16].

5. Outlook

As discussed in the preceding chapter, the intracavity losses in the OPO could be identified as the main limiting factor for the achievable squeezing level. This chapter discusses adjustments in the experimental parameters and improvements in the squeezer design that could allow to overcome the current limitations and increase overall operability.

5.1. Optimized cavity parameters

In the current design, only a small increase of the intracavity round trip losses L directly leads to a significantly reduced escape efficiency $\eta_{\mathrm{esc}} = \frac{T}{T+L}$ (see table 4.3 and section 4.7.3). With PPKTP as nonlinear crystal material, an increase of the intracavity losses due the pump light is inevitable when the OPO is pumped with 400 nm light. In this case, η_{esc} can be increased by increasing the transmissivity T of the coupling mirror. Figure 5.1 shows the escape efficiency η_{esc} and the corresponding reachable squeezing level for varying intracavity losses. For the squeezing level estimations, the detection efficiencies from table 4.2 were considered, except from the mode-matching efficiency η_{MM}, which was increased to 99 %, since it faces no technical limitations and, with some effort, can realistically be brought to this level.

The results from figure 5.1 suggest that, in the presence of UV induced intracavity losses of $L \approx 1.5\,\%$ (as determined by the squeezing measurement in figure 4.8), an increased coupling mirror transmissivity of $T = 20\,\%$ would increase the escape efficiency, such that 7.75 dB of squeezing could be detected after considering all other loss channels; more than 11.5 dB of squeezing would leave the OPO in this case. Even for higher intracavity losses of 3 %, it should be possible to measure up to 6.5 dB of squeezing, compared to at maximum 3.5 dB for $T = 5\,\%$, as in the current design. Other experiments aiming at squeezing around 795 nm typically use coupling mirror reflectivities of 7 − 11.5 % [App+07; Hét+07; Tan+06a; Zuo+22; Han+16], with the tendency that a higher transmissivity leads to a higher realized squeezing level.

Although higher transmissivities of the coupling mirror would improve the achievable external squeezing, even for $T = 20\,\%$ and $L = 1.5\,\%$, the escape efficiency would still be the dominant loss source with $\eta_{\mathrm{esc}} = 93\,\%$. It must be taken into account that a reduction of the reflectivity also decreases the effective interaction length of the vacuum field with the pump

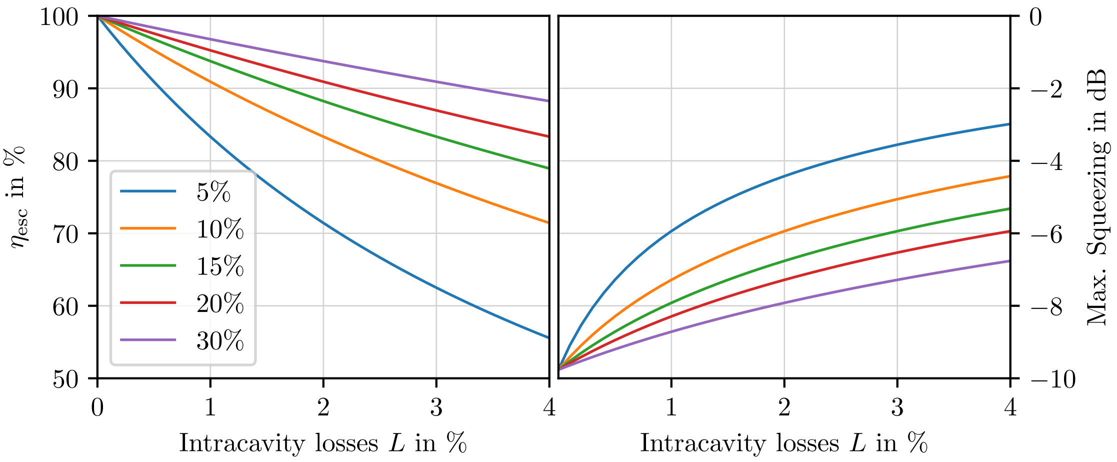

Figure 5.1.: Escape efficiency η_{esc} (left) and estimated maximal squeezing level (right) versus the intracavity losses L for varying coupling mirror transmissivity T. The blue line with $T = 5\,\%$ corresponds to the current experimental design.

light, which means that higher pump powers would be required to operate the OPO at its threshold. However, the squeezing measurements in figures 4.8 and 4.9 illustrate that at the current loss levels of the system, an increase of the pump power toward the OPO threshold mainly increases the antisqueezing level and does not significantly increase the squeezing level; therefore, it is perhaps not even necessary to operate at the OPO threshold to measure improved squeezing levels.

If one wants to operate at the OPO threshold anyway, increasing T from 5 % to 10 % requires to double the pump power (from 16 mW to 32 mW). These powers are still within reach for a fresh SHG crystal, as can be seen from figure 3.10. A further reduction to $T = 20\,\%$ would require to increase the input power to more than 64 mW, which exceeds the maximum power that was measured in the transmission port of the SHG cavity in this setup. To yield higher pump power in one beam, it would in principle be possible to overlap the 400 nm light from both output ports with the help of a polarizing beam splitter and a $\lambda/2$-waveplate; however, having only one output port of the SHG cavity and coating the other end mirror highly reflective for 400 nm seems more practically from an experimental point of view, at the cost that the counter-propagating 400 nm beams have to be properly matched to each other and that the light travels on average longer distances inside the absorptive nonlinear medium. Such a device was studied by Yang *et al.* and compared to a bow-tie ring cavity design with only one propagation direction, where all generated second harmonic light exits the cavity through the same port [Yan+15]. In the direct comparison, the bow-tie design allowed for higher output powers and conversion efficiencies compared to a linear cavity. In a similar bow-tie design, Wang *et al.* generated up to 140 mW of 400 nm light from 250 mW of 800 nm pump light [Wan+17]; the required pump powers can be easily supplied by the Toptica TA pro laser used in the current experiment. Thus, with the appropriate SHG cavity design, it should, in principle, be possible to operate the OPO close to its threshold to achieve maximal possible squeezing also at significantly reduced coupling mirror reflectivity.

5.2. Alternative crystal materials

The other factor impacting on the escape efficiency are the intracavity losses. Since gray tracking recovers significantly faster when the crystal is heated above 80 °C, where thermal phonons are able to break the activated color centers [WPL04], it seems worth considering whether an operation of the OPO above this temperature would prevent an increase in absorption in the first place. However, measurements by Tjörnhammar *et al.* on PPKTP and some of its isomorphs (Rb:KTiOPO$_4$, RbTiOPO$_4$, KTiOAsO$_4$ and RbTiOAsO$_4$) show that, while the crystal temperature significantly accelerates the recovery after illumination, it does not reduce the absorption during illumination [Tjö+15]. Furthermore, while the other isomorphs may recover much faster than KTP and have lower residual absorption, the absorption coefficients during illumination with 398 nm seem to range on a similar level for all tested samples. However, the study shows that, under repeated exposure, KTP accumulates absorption much more than the other studied materials [Tjö+15]. It therefore seems worth considering whether one of these isomorphs can prevent the forming of accumulated, long-lasting grey tracking, while at the same time maintaining the high optical nonlinearity of KTP.

Hirohashi *et al.* measured BLIIRA in various ferroelectrics designed for improved photorefractive resistance, especially in the blue-green wavelength region, including MgO-doped congruent and stoichiometric LiNbO$_3$ (MgO:CLN and MgO:SLN) [Hir+07]. According to their results, MgO:SLN has lower initial absorption in the infrared wavelength region compared to PPKTP and is less susceptible to BLIIRA compared to the other tested samples. Furthermore, at least for picosecond pulses with peak intensities of $2-8\,\mathrm{GW/cm^2}$, the BLIIRA losses seem to saturate at around 0.04 %/cm, which is much lower than in KTP. MgO:SLN can be quasi-phasematched and exhibits a very strong nonlinearity of $|d_{33}(852\,\mathrm{nm})| = 28.4\,\mathrm{pm/V}$ [Nik05], which would reduce the OPO threshold and consequently also the required pump power compared to KTP. A transparency window down to 300 nm [Nik05] makes MgO:SLN an interesting candidate to reduce the pump light induced losses at 800 nm. In contrast to KTP, LiNbO$_3$ is susceptible to photorefractive damage already at low input powers. With the MgO-doping, the damage threshold has been increased by four orders of magnitude compared to the undoped material [Nik05]; for cw illumination at 532 nm, it is on the order of $2\,\mathrm{MW/cm^2}$ [Nik05]. Although this exceeds the estimated intensity in the OPO by three orders of magnitude, the damage threshold strongly depends on the wavelength, and further quantitative research would be necessary to verify the applicability of MgO:SLN as a nonlinear crystal material for the OPO.

5.3. Decoupling degrees of freedom

As discussed in section 3.2.6, the monolithic design is a system with highly coupled degrees of freedom (e.g., cavity resonance frequency and phase-matching temperature), which can only be actuated on slow, thermal timescales. Furthermore, unavoidable feedback effects, such as the heating and thermal expansion of the cavity when it becomes resonant with the 400 nm light, make it impossible to operate the experiment under well-defined conditions, and top of fringe locking is not possible. This prevents a stable and reproducible operation of the SHG cavity and the OPO.

For stable operation, a decoupling of these degrees of freedom and the ability to adjust the cavity length instantaneously would be beneficial. This can be realized by two means: First, by avoiding double resonance of the OPO and making it single pass for the 400 nm pump light, its resonance condition for 800 nm can be tuned without changing the pump power of the OPO; subsequently, uncontrolled feedback effects are avoided. Second, semi-monolithic, bow-tie or any other non-monolithic cavity design with at least one piezo-actuated mirror allow fast adjustments of the cavity length and resonance frequency; this decouples the resonance frequency from the phase-matching temperature. The ability to lock the squeezed light source to a specific external frequency (e.g., an atomic resonance or the resonance frequencies of other optical cavities) would, furthermore, greatly enhance its applicability in other experiments.

Most other experiments aiming at squeezed states of light around 800 nm do already use single resonant bow-tie cavities [Tan+06b; Hét+07; App+07; Han+16] both for SHG and OPO; these consist of four mirrors and an anti-reflex coated nonlinear crystal in the focus of the cavity mode. In this setup, a good mode overlap between pump and OPO is achieved by first operating the cavity as a double-resonant cavity to match all incoming beams to the fundamental and harmonic cavity modes separately. Afterwards, the coupling mirrors are replaced with mirrors that are anti-reflex coated for the harmonic 400 nm light. This alignment procedure allows to overlap the pump beam with the OPO mode, while maintaining the full flexibility to tune phase-matching temperature and cavity resonance frequency independently and reducing thermal feedback effects. Since there are two propagation directions in a bow-tie ring cavity, a counter-propagating coherent control beam at the squeezing wavelength can be used to lock the OPO without interfering with the generated squeezed vacuum states.

Lastly, a cavity design where the mirror surfaces are not coated directly onto the crystal allows significantly longer operation times for each nonlinear crystal: while in the monolithic design, the geometry of the crystal and its radii of curvature define exactly one cavity mode on which the crystal can be operated, non-monolithic designs allow to change to a different crystal region once the initial beam path starts to degrade. With the correct alignment and plane anti-reflex coated end facets, such a shift could even be performed without changing the cavity mode; this would allow extended continuous operation compared to any monolithic design.

5.4. Conclusion

All in all, in this thesis, a squeezed light source in the configuration with both a monolithic SHG cavity and a monolithic OPO has been thoroughly characterized. On a fresh crystal, conversion efficiencies of up to 58 % were reached in the SHG process. It was found that, in the presence of significant absorption and heating of the crystal, the monolithic design faces unavoidable feedback effects on the resonance frequency, that challenge the operability. Nevertheless, for the SHG cavity, methods could be developed that allowed to probe quantities that can be straightforwardly measured in a non-monolithic system but require more sophisticated approaches for monolithic cavities. In this way, the gain profile and its shift with temperature in frequency space was characterized. The monolithic design defines exactly one well-defined cavity mode along which degradation of the crystal and recovery through annealing could be studied.

With over 16 mW in transmission of the SHG cavity, sufficient 400 nm light could be generated to reach the threshold of the monolithic OPO. Up to 4 dB of squeezing could be detected in this setup, which is, to date, the highest reported squeezing value from a monolithic OPO at 800 nm. With use of PPKTP as nonlinear medium, unavoidable gray-tracking losses reduced the escape efficiency of the OPO and set a fundamental limit to the achievable squeezing level. The suggestions proposed earlier in this chapter provide ideas of different scope for improving the performance and operability of the system – from a change of the single limiting parameter in the monolithic cavity, to using alternative crystal materials that may be less susceptible to grey tracking, to adopting alternative designs. Especially the decoupling between crystal temperature and resonance frequency makes the bow-tie design a promising candidate for a squeezed light source around 800 nm, that aims at increasing the measurement sensitivity in quantum optics experiments and to study the fundamental interactions between squeezed states of light and matter.

Appendix

A. Homodyne detection

In balanced homodyne detection, weak signals are amplified with the help of a local oscillator, whose classical and quantum noises cancel in the detection process. The first part of this appendix will derive this property for arbitrary splitting ratio at the beam splitter. The second part discusses the handling of unequal detection efficiencies in both arms of the detector. This study was performed to ensure that counteracting detection inefficiencies by adjustment of the beam splitter's splitting ratio maintains the signal of interest in the detector's output signal.

Lossless balanced homodyne detection

A homodyne detector has two input ports, one for the signal $S(t)$ and one for the local oscillator $L(t)$. Both quantities are subject to noises in the amplitude and phase quadratures, which are denoted by the small letters. The capital letters denote classical light fields. Without loss of generality, the signal field can be taken as reference to have only a classical contribution S in the amplitude quadrature. The classical quadratures of the local oscillator then depend on the relative phase ϕ between local oscillator and signal path. With this convention, the amplitudes (including their noises) in the signal and local oscillator path read [Kor20]

$$S(t) = (S + s^c(t))\cos(\omega_0 t) + s^s(t)\sin(\omega_0 t) \tag{A.1}$$

$$L(t) = (L_0\cos\phi + l^c(t))\cos(\omega_0 t) + (L_0\sin\phi + l^s(t))\sin(\omega_0 t) \tag{A.2}$$

These signals are overlapped on a beam splitter. Assuming a lossless beam splitter with power transmissivity T, the output amplitudes are calculated from the beam splitter matrix

$$\begin{pmatrix}\mathrm{out}_1\\ \mathrm{out}_2\end{pmatrix} = \begin{pmatrix} t & r \\ -r & t\end{pmatrix}\begin{pmatrix}L(t)\\ S(t)\end{pmatrix} \tag{A.3}$$

with $t = \sqrt{T}$ and $r = \sqrt{1-T}$. The power in both output ports is obtained by absolute squaring and time-averaging the beam splitter's output amplitudes $\mathrm{out}_{1,2}$. Assuming 100 %

detection efficiency, both photo currents are proportional to the incident power with the same responsivity g (in A/W). The resulting photo currents read

$$\begin{aligned} i_1 &= g \cdot \overline{|rS(t)+tL(t)|^2} && \text{(A.4)}\\ \text{and}\quad i_2 &= g \cdot \overline{|tS(t)-rL(t)|^2}. && \text{(A.5)} \end{aligned}$$

The responsivity g would appear in every line of the calculation to match the units, but without adding additional physical insight. For clarity and without loss of generality, the following calculation will therefore set $g = 1$. Since r, t, $S(t)$ and $L(t)$ are real quantities, the absolute square can be replaced by an ordinary square and the time average can be taken separately from each of the summands:

$$\begin{aligned} i_1 &= \overline{|rS(t)+tL(t)|^2} = r^2\overline{S^2(t)} + t^2\overline{L^2(t)} + 2rt\overline{S(t)L(t)} && \text{(A.6)}\\ \text{and}\quad i_2 &= \overline{|tS(t)-rL(t)|^2} = t^2\overline{S^2(t)} + r^2\overline{L^2(t)} - 2rt\overline{S(t)L(t)}. && \text{(A.7)} \end{aligned}$$

For further evaluation, it turns out handy to calculate $\overline{|S^2(t)|^2}$, $\overline{|L^2(t)|^2}$ and $\overline{S(t)L(t)}$ separately from eq. (A.1) and eq. (A.2). Thus,

$$\begin{aligned} \overline{S^2(t)} &= \overline{\big((S+s^c(t))\cos(\omega_0 t) + s^s(t)\sin(\omega_0 t)\big)^2}\\ &= \overline{(S+s^c(t))^2\cos^2(\omega_0 t) + s^{s2}(t)\sin^2(\omega_0 t) + (S+s^c(t))s^s(t)\cos(\omega_0 t)\sin(\omega_0 t)}\\ &= (S+s^c(t))^2\underbrace{\overline{\cos^2(\omega_0 t)}}_{=\frac{1}{2}} + s^{s2}(t)\underbrace{\overline{\sin^2(\omega_0 t)}}_{=\frac{1}{2}} + (S+s^c(t))s^s(t)\underbrace{\overline{\cos(\omega_0 t)\sin(\omega_0 t)}}_{=0} \qquad \text{(A.8)}\\ &= \frac{1}{2}\Big((S+s^c(t))^2 + s^{s2}(t)\Big)\\ &\approx \frac{1}{2}S^2 + Ss^c(t), \end{aligned}$$

where it was assumed that the noise terms $s^c(t)$, $l^c(t)$, $s^s(t)$ and $l^s(t)$ change slowly with respect to the laser frequency ω_0 and the time average was taken only over the terms containing $\omega_0 t$:

$$\begin{aligned} \frac{1}{2\pi}\int_0^{2\pi}\cos^2(\omega_0 t)d\omega_0 t &= \frac{1}{2\pi}\int_0^{2\pi}\sin^2(\omega_0 t)d\omega_0 t = \frac{1}{2} && \text{(A.9)}\\ \frac{1}{2\pi}\int_0^{2\pi}\cos(\omega_0 t)\sin(\omega_0 t)d\omega_0 t &= \frac{1}{2\pi}\int_0^{2\pi}\frac{1}{2}\sin(2\omega_0 t)d\omega_0 t = 0 && \text{(A.10)} \end{aligned}$$

Additionally, in the last step of eq. (A.8), the terms containing the product of two noise terms were neglected, since they are small compared to any classically amplified noise term.

Similarly,

$$\begin{aligned}
\overline{|L(t)|^2} &= \overline{\big((L_0\cos\phi + l^c(t))\cos(\omega_0 t) + (L_0\sin\phi + l^s(t))\sin(\omega_0 t)\big)} \\
&= \overline{(L_0\cos\phi + l^c(t))^2\cos^2(\omega_0 t) + (L_0\sin\phi + l^s(t))^2\sin^2(\omega_0 t)} \\
&\quad \overline{+2(L_0\cos\phi + l^c(t))(L_0\sin\phi + l^s(t))\cos(\omega_0 t)\sin(\omega_0 t)} \\
&= (L_0\cos\phi + l^c(t))^2\overline{\cos^2(\omega_0 t)} + (L_0\sin\phi + l^s(t))^2\overline{\sin^2(\omega_0 t)} \\
&\quad + 2(L_0\cos\phi + l^c(t))(L_0\sin\phi + l^s(t))\overline{\cos(\omega_0 t)\sin(\omega_0 t)} \\
&= \frac{1}{2}\Big((L_0\cos\phi + l^c(t))^2 + (L_0\sin\phi + l^s(t))^2\Big) \\
&= \frac{1}{2}\Big((L_0 + 2L_0(l^c(t)\cos\phi + l^s(t)\sin\phi) + l^{c2}(t)^2 + l^{s2}(t)\Big) \\
&\approx \frac{1}{2}L_0^2 + L_0(l^c(t)\cos\phi + l^s(t)\sin\phi)
\end{aligned} \tag{A.11}$$

and the cross term

$$\begin{aligned}
\overline{S(t)L(t)} &= \overline{(S + s^c(t))\cos(\omega_0 t) + s^s(t)\sin(\omega_0 t)((L_0\cos\phi + l^c(t))\cos(\omega_0 t) +} \\
&\qquad \overline{(L_0\sin\phi + l^s(t))\sin(\omega_0 t)} \\
&= (S + s^c(t))(L_0\cos\phi + l^c(t))\overline{\cos^2(\omega_0 t)} + s^s(t)(L_0\sin\phi + l^s(t))\overline{\sin^2(\omega_0 t)} \\
&\quad + \Big((S + s^c(t))(L_0\sin\phi + l^s(t)) + s^s(t)(L_0\cos\phi + l^c(t))\overline{\cos(\omega_0 t)\sin(\omega_0 t)} \\
&= \frac{1}{2}\Big(SL_0\cos\phi + Sl^c(t) + s^c(t)L_0\cos\phi + s^c(t)l^c(t) + s^s(t)L_0\sin\phi + s^s(t)l^s(t)\Big) \\
&\approx \frac{1}{2}\Big(S(L_0\cos\phi + l^c(t)) + L_0(s^c(t)\cos\phi + s^s(t)\sin\phi)\Big)
\end{aligned} \tag{A.12}$$

can be calculated.

The actual output signal of the homodyne detector is the difference between both photo currents i_1 and i_2 from eq. (A.6) and eq. (A.7). With eq. (A.8), eq. (A.11) and eq. (A.12), the homodyne signal becomes

$$\begin{aligned}
i_1 - i_2 &= r^2\overline{S^2(t)} + t^2\overline{L^2(t)} + 2rt\overline{S(t)L(t)} - \Big(t^2\overline{S^2(t)} + r^2\overline{L^2(t)} - 2rt\overline{S(t)L(t)}\Big) \\
&= (t^2 - r^2)\Big(\overline{L^2(t)} - \overline{S^2(t)}\Big) + 4rt\overline{S(t)L(t)} \\
&= (t^2 - r^2)\Big(\frac{1}{2}L_0^2 + L_0(l^c(t)\cos\phi + l^s(t)\sin\phi) - \Big(\frac{1}{2}S^2 + Ss^c(t)\Big)\Big) \\
&\quad + 4rt\frac{1}{2}\Big(S(L_0\cos\phi + l^c(t)) + L_0(s^c(t)\cos\phi + s^s(t)\sin\phi)\Big) \\
&= (t^2 - r^2)\Big(\frac{L_0^2}{2} - \frac{-S^2}{2} + L_0\big(l^c(t)\cos\phi + l^s(t)\sin\phi\big) - Ss^c(t)\Big) \\
&\quad + 2rt\Big(L_0\big(s^c(t)\cos\phi + s^s(t)\sin\phi\big) + SL_0\cos\phi + Sl^c(t)\Big)
\end{aligned} \tag{A.13}$$

In the absence of a classical signal (i.e., $S = 0$), this term reduces to

$$i_1 - i_2 = \left(t^2 - r^2\right)\Big(\underbrace{\frac{L_0^2}{2}}_{\text{offset}} + L_0 \underbrace{\left(l^c(t)\cos\phi + l^s(t)\sin\phi\right)}_{\text{amplified laser noise}}\Big) + 2rtL_0 \underbrace{\left(s^c(t)\cos\phi + s^s(t)\sin\phi\right)}_{\text{amplified signal noises}} \tag{A.14}$$

For $t = r = \sqrt{1/2}$, the first term vanishes, and one ends up with the well known formula for balanced homodyne detection:

$$i_1 - i_2 = L_0\Big(s^c(t)\cos\phi + s^s(t)\sin\phi\Big) \tag{A.15}$$

In this case, both noise terms of the signal $s^c(t)$ and $s^s(t)$ can be amplified by the amplitude of the local oscillator L_0 by choosing the appropriate phase ϕ between signal and local oscillator. Classical and quantum noises from the local oscillator port are canceled and do not disturb the signal.

If $t \neq r$, the first term of eq. (A.14) introduces a phase-independent offset to the homodyne signal. Furthermore, in this case, also the classical laser noise $l^c(t)$ is amplified by the local oscillator amplitude and added to the homodyne signal, which would disturb the measurement of $s^s(t)$ and $s^c(t)$. However, by adjustment of the beam splitter's splitting ratio (usually by fine-tuning the angle of incidence), the DC-offset can be reduced to zero; it is then assured that the resulting signal is free of any classical laser noise.

Homodyne detection at non-equal detection efficiency

When one assumes that the used photo diodes have different detection efficiencies η_1 and η_2 (for example, through different quantum efficiencies, absorption losses, ...), a 50:50 splitting would lead to an offset of the signal (since equal powers in both beams would be converted to different currents). If the splitting ratio is adjusted to $t \neq r$ to make the DC offset vanish, then the signal will also be unevenly split, sending more power of the signal beam to the photodiode with the higher detection efficiency. It seems worth studying whether the detector's output signal is, in this case, still proportional to the quadratures of the signal path or whether such an asymmetry in the detection inefficiency would prevent the experimenter from measuring the desired quantity.

The detection efficiencies $\eta_{1,2}$ act as a proportionality factor between the currents $i_{1,2}$ that would be detected at 100% quantum efficiency and the current $i^*_{1,2}$ that is actually detected in the presence of detection inefficiencies. In this case, the homodyne signal is given by

$$i^*_1 - i^*_2 = \eta_1 i_1 - \eta_2 i_2. \tag{A.16}$$

So, analogue to eq. (A.13), one can calculate

$$\begin{aligned}
i_1^* - i_2^* &= \eta_1 i_1 - \eta_2 i_2 \\
&= \eta_1 \left(r^2 \overline{S^2(t)} + t^2 \overline{L^2(t)} + 2rt\overline{S(t)L(t)} \right) - \eta_2 \left(t^2 \overline{S^2(t)} + r^2 \overline{L^2(t)} - 2rt\overline{S(t)L(t)} \right) \\
&= (\eta_1 r^2 - \eta_2 t^2)\overline{S^2(t)} + (\eta_1 t^2 - \eta_2 r^2)\overline{L^2(t)} + (\eta_1 + \eta_2)2rt\overline{S(t)L(t)} \\
&= (\eta_1 r^2 - \eta_2 t^2) \left(\frac{1}{2}S^2 + S s^c(t) \right) + (\eta_1 t^2 - \eta_2 r^2) \left(\frac{1}{2}L_0^2 + L_0(l^c(t)\cos\phi + l^s(t)\sin\phi) \right) \\
&\quad + (\eta_1 + \eta_2)2rt\Big(S(L_0\cos\phi + l^c(t)) + L_0(s^c(t)\cos\phi + s^s(t)\sin\phi) \Big) \\
&\overset{S=0}{=} (\eta_1 t^2 - \eta_2 r^2)\Big(\frac{1}{2}L_0^2 + L_0(l^c(t)\cos\phi + l^s(t)\sin\phi) \Big) \\
&\quad + (\eta_1 + \eta_2)2rt\Big(L_0(s^c(t)\cos\phi + s^s(t)\sin\phi) \Big),
\end{aligned} \tag{A.17}$$

where in the last line the fact was used that only noise terms enter the homodyne in the signal port, and $S = 0$. The last line in eq. (A.17) looks similar to eq. (A.14): there is a term that amplifies the signal noises $s^c(t)$ and $s^s(t)$ with the classical local oscillator amplitude L_0, depending on the relative phase ϕ between signal and local oscillator beam; this is the quantity of interest. The other bracket contains both an offset term and the amplified noises $l^c(t)$ and $l^s(t)$ of the local oscillator. However, the whole bracket vanishes when $\eta_1 t^2 - \eta_2 r^2 = 0$; this condition can be verified in the experiment by making the offset vanish. Thus, it is possible to compensate detection inefficiencies by adjustments of the splitting ratio without introducing classical laser noise from the local oscillator or inadvertently measuring a different quantity than $s^c(t)$ or $s^s(t)$.

References

[AAK04] D. Akamatsu, K. Akiba, and M. Kozuma. “Electromagnetically Induced Transparency with Squeezed Vacuum”. *Phys. Rev. Lett.* **92** (20 2004), 203602. DOI: `10.1103/PhysRevLett.92.203602`.

[Aas+13] J. Aasi et al. “Enhanced sensitivity of the LIGO gravitational wave detector by using squeezed states of light”. *Nature Photonics* **7** (2013), 613. DOI: `10.1038/nphoton.2013.177`.

[Aka+07] D. Akamatsu, Y. Yokoi, M. Arikawa, S. Nagatsuka, T. Tanimura, A. Furusawa, and M. Kozuma. “Ultraslow Propagation of Squeezed Vacuum Pulses with Electromagnetically Induced Transparency”. *Phys. Rev. Lett.* **99** (15 2007), 153602. DOI: `10.1103/PhysRevLett.99.153602`.

[AMG10] I. H. Agha, G. Messin, and P. Grangier. “Generation of pulsed and continuous-wave squeezed light with 87Rb vapor”. *Opt. Express* **18** (2010), 4198–4205. DOI: `10.1364/OE.18.004198`.

[And+20] R. B. de Andrade, H. Kerdoncuff, K. Berg-Sørensen, T. Gehring, M. Lassen, and U. L. Andersen. “Quantum-enhanced continuous-wave stimulated Raman scattering spectroscopy”. *Optica* **7** (2020), 470–475. DOI: `10.1364/OPTICA.386584`.

[And+92] B. Andreev, V. Maslov, B. Mikhailov, S. Pak, O. Shaunin, and I. Shcherbakov. “Experimental study of the laser-induced absorption effect and the nature of color centers in potassium titanyl phosphate crystal”. *Proceedings of SPIE - The International Society for Optical Engineering* (1992), 280–289. DOI: `10.1117/12.131778`.

[App+07] J. Appel, D. Hoffman, E. Figueroa, and A. I. Lvovsky. “Electronic noise in optical homodyne tomography”. *Physical Review A - Atomic, Molecular, and Optical Physics* **75** (2007), 1–4. DOI: `10.1103/PhysRevA.75.035802`.

[App+08] J. Appel, E. Figueroa, D. Korystov, M. Lobino, and A. I. Lvovsky. “Quantum memory for squeezed light”. *Physical Review Letters* **100** (2008), 1–4. DOI: `10.1103/PhysRevLett.100.093602`.

[Bai+20] L. Bai, X. Wen, Y. Yang, J. He, and J. Wang. “Laser intensity noise suppression for preparing audio-frequency squeezed vacuum state of light”. *Applied Sciences (Switzerland)* **10** (2020). DOI: `10.3390/app10041415`.

[Bai+21] L. Bai, X. Wen, Y. Yang, L. Zhang, J. He, Y. Wang, and J. Wang. "Quantum-enhanced rubidium atomic magnetometer based on Faraday rotation via 795 nm stokes operator squeezed light". *Journal of Optics* **23** (2021), 085202. DOI: `10.1088/2040-8986/ac1b7c`.

[Bai+22] L. Bai, L. Zhang, Y. Yang, R. Chang, Y. Qin, J. He, X. Wen, and J. Wang. "Enhancement of spin noise spectroscopy of rubidium atomic ensemble by using the polarization squeezed light". *Optics Express* **30** (2022), 1925. DOI: `10.1364/oe.448084`.

[BF14] D. D. Brown and A. Freise. *Finesse.* The software and source code is available at `http://www.gwoptics.org/finesse`. Finesse is licensed under the GPL3 license: `https://www.gnu.org/licenses/gpl-3.0.html`. 2014. DOI: `10.5281/zenodo.821363`.

[BGS25] A. Bocchini, U. Gerstmann, and W. G. Schmidt. "Microscopic origin of gray tracks in $\mathrm{KTiOPO_4}$". *Phys. Rev. B* **111** (10 2025), 104103. DOI: `10.1103/PhysRevB.111.104103`.

[Boc+20] A. Bocchini, C. Eigner, C. Silberhorn, W. G. Schmidt, and U. Gerstmann. "Understanding gray track formation in KTP: Ti3+ centers studied from first principles". *Physical Review Materials* **4** (2020), 1–7. DOI: `10.1103/PhysRevMaterials.4.124402`.

[Bou+94] B. Boulanger, M. M. Fejer, R. Blachman, and P. F. Bordui. "Study of KTiOPO4 gray-tracking at 1064, 532, and 355 nm". *Applied Physics Letters* **65** (1994), 2401–2403. DOI: `10.1063/1.112688`.

[Bou+99] B. Boulanger, I. Rousseau, J. P. Fève, M. Maglione, B. Ménaert, and G. Marnier. "Optical Studies of Laser-Induced Gray-Tracking in KTP". *IEEE Journal of Quantum Electronics* **35** (1999), 281–286. DOI: `10.1109/3.748831`.

[Boy08] R. W. Boyd. *Nonlinear Optics, Third Edition.* 3rd. USA: Academic Press, Inc., 2008.

[Cas+21] C. Casacio, L. Madsen, A. Terrasson, M. Waleed, K. Barnscheidt, B. Hage, M. Taylor, and W. Bowen. "Quantum-enhanced nonlinear microscopy". *Nature* **594** (2021), 201–206. DOI: `10.1038/s41586-021-03528-w`.

[Cav81] C. M. Caves. "Quantum-mechanical noise in an interferometer". *Phys. Rev. D* **23** (8 1981), 1693–1708. DOI: `10.1103/PhysRevD.23.1693`.

[CLG87] M. J. Collett, R. Loudon, and C. W. Gardiner. "Quantum theory of optical homodyne and heterodyne detection". *Journal of Modern Optics* **34** (1987), 881–902. DOI: `10.1080/09500348714550811`.

[DP04] A. Dantan and M. Pinard. "Quantum-state transfer between fields and atoms in electromagnetically induced transparency". *Phys. Rev. A* **69** (4 2004), 043810. DOI: `10.1103/PhysRevA.69.043810`.

[Dri+86] T. A. Driscoll, H. J. Hoffman, R. E. Stone, and P. E. Perkins. “Efficient second-harmonic generation in KTP crystals”. *J. Opt. Soc. Am. B* **3** (1986), 683–686. DOI: `10.1364/JOSAB.3.000683`.

[EA03] S. Emanueli and A. Arie. “Temperature-dependent dispersion equations for KTiOPO4 and KTiOAsO4”. *Appl. Opt.* **42** (2003), 6661–6665. DOI: `10.1364/AO.42.006661`.

[Ein17] A. Einstein. “Zur Quantentheorie der Strahlung”. *Physikalische Zeitschrift* **18** (1917), 121–128.

[Fej+92] M. M. Fejer, D. H. Jundt, R. L. Byer, and G. A. Magel. “Quasi-Phase-Matched Second Harmonic Generation: Tuning and Tolerances”. *IEEE Journal of Quantum Electronics* **28** (1992), 2631–2654. DOI: `10.1109/3.161322`.

[Fèv+97] J. Fève, B. Boulanger, G. Marnier, and H. Albrecht. “Repetition rate dependence of gray-tracking in KTiOPO4 during second-harmonic generation at 532 nm”. *Applied Physics Letters* **70** (1997), 277–279. DOI: `10.1063/1.118391`.

[FL00] M. Fleischhauer and M. D. Lukin. “Dark-State Polaritons in Electromagnetically Induced Transparency”. *Phys. Rev. Lett.* **84** (22 2000), 5094–5097. DOI: `10.1103/PhysRevLett.84.5094`.

[FL02] M. Fleischhauer and M. D. Lukin. “Quantum memory for photons: Dark-state polaritons”. *Phys. Rev. A* **65** (2 2002), 022314. DOI: `10.1103/PhysRevA.65.022314`.

[Fra] A. Franzen. *ComponentLibrary (a vector graphics library for illustrations of optics experiments).* available at https://www.gwoptics.org/ComponentLibrary/. The ComponentLibrary is licensed under the Creative Commons Attribution-NonCommercial 3.0 Unported License: https://creativecommons.org/licenses/by-nc/3.0/.

[Fra+99] K. Fradkin, A. Arie, A. Skliar, and G. Rosenman. “Tunable midinfrared source by difference frequency generation in bulk periodically poled KTiOPO4”. *Applied Physics Letters* **74** (1999), 914–916. DOI: `10.1063/1.123408`.

[Fur+01] Y. Furukawa, K. Kitamura, A. Alexandrovski, R. K. Route, M. M. Fejer, and G. Foulon. “Green-induced infrared absorption in MgO doped LiNbO3”. *Applied Physics Letters* **78** (2001), 1970–1972. DOI: `10.1063/1.1359137`.

[GK05] C. C. Gerry and P. L. Knight. *Introductory Quantum Optics.* New York: Cambridge University Press, 2005, p. 317.

[GKP01] D. Gottesman, A. Kitaev, and J. Preskill. “Encoding a qubit in an oscillator”. *Phys. Rev. A* **64** (1 2001), 012310. DOI: `10.1103/PhysRevA.64.012310`.

[Gla63] R. J. Glauber. “Coherent and Incoherent States of the Radiation Field”. *Phys. Rev.* **131** (6 1963), 2766–2788. DOI: `10.1103/PhysRev.131.2766`.

[Gro+13] H. Grote, K. Danzmann, K. L. Dooley, R. Schnabel, J. Slutsky, and H. Vahlbruch. “First Long-Term Application of Squeezed States of Light in a Gravitational-Wave Observatory”. *Phys. Rev. Lett.* **110** (18 2013), 181101. DOI: `10.1103/PhysRevLett.110.181101`.

[Han+16] Y. Han, X. Wen, J. He, B. Yang, Y. Wang, and J. Wang. “Improvement of vacuum squeezing resonant on the rubidium D1 line at 795 nm”. *Optics Express* **24** (2016), 2350. DOI: `10.1364/oe.24.002350`.

[Hét+07] G. Hétet, O. Glöckl, K. A. Pilypas, C. C. Harb, B. C. Buchler, H. A. Bachor, and P. K. Lam. “Squeezed light for bandwidth-limited atom optics experiments at the rubidium D1 line”. *Journal of Physics B: Atomic, Molecular and Optical Physics* **40** (2007), 221–226. DOI: `10.1088/0953-4075/40/1/020`.

[Hèt+08] G. Hètet, B. C. Buchler, O. Glöeckl, M. T. L. Hsu, A. M. Akulshin, H. A. Bachor, and P. K. Lam. “Delay of squeezing and entanglement using electromagnetically induced transparency in a vapour cell”. *Optics Express* **16** (2008), 7369. DOI: `10.1364/oe.16.007369`.

[Hir+07] J. Hirohashi, V. Pasiskevicius, S. Wang, and F. Laurell. “Picosecond blue-light-induced infrared absorption in single-domain and periodically poled ferroelectrics”. *Journal of Applied Physics* **101** (2007). DOI: `10.1063/1.2434007`.

[Hon+08] K. Honda, D. Akamatsu, M. Arikawa, Y. Yokoi, K. Akiba, S. Nagatsuka, T. Tanimura, A. Furusawa, and M. Kozuma. “Storage and retrieval of a squeezed vacuum”. *Physical Review Letters* **100** (2008), 4–7. DOI: `10.1103/PhysRevLett.100.093601`.

[Kli+16] J. Klinder, H. Keßler, C. Georges, J. Vargas, and A. Hemmerich. “Bose–Einstein condensates in an optical cavity with sub-recoil bandwidth”. *Applied Physics B: Lasers and Optics* **122** (2016), 1–15. DOI: `10.1007/s00340-016-6577-7`.

[KM19] S. Kim and A. M. Marino. “Atomic resonant single-mode squeezed light from four-wave mixing through feedforward”. *Optics Letters* **44** (2019), 4630. DOI: `10.1364/ol.44.004630`.

[Kor20] M. Korobko. “Taming the quantum noise - How quantum metrology can expand the reach of gravitational-wave observatories”. PhD thesis. Universität Hamburg, 2020.

[KT02] K. Kato and E. Takaoka. “Sellmeier and thermo-optic dispersion formulas for KTP”. *Appl. Opt.* **41** (2002), 5040–5044. DOI: `10.1364/AO.41.005040`.

[Las+10] N. Lastzka, J. Steinlechner, S. Steinlechner, and R. Schnabel. “Measuring small absorptions by exploiting photothermal self-phase modulation”. English. *Applied Optics* **49** (2010), 5391–5398. DOI: `10.1364/AO.49.005391`.

[Li+18] B.-B. Li, J. Bílek, U. B. Hoff, L. S. Madsen, S. Forstner, V. Prakash, C. Schäfermeier, T. Gehring, W. P. Bowen, and U. L. Andersen. "Quantum enhanced optomechanical magnetometry". *Optica* **5** (2018), 850–856. DOI: `10.1364/OPTICA.5.000850`.

[Li+22] T. Li, F. Li, X. Liu, V. V. Yakovlev, and G. S. Agarwal. "Quantum-enhanced stimulated Brillouin scattering spectroscopy and imaging". *Optica* **9** (2022), 959–964. DOI: `10.1364/OPTICA.467635`.

[Liu+18] K. Liu, C. Cai, J. Li, L. Ma, H. Sun, and J. Gao. "Squeezing-enhanced rotating-angle measurement beyond the quantum limit". *Applied Physics Letters* **113** (2018), 261103. DOI: `10.1063/1.5066028`.

[LK87] R. Loudon and P. Knight. "Squeezed Light". *Journal of Modern Optics* **34** (1987), 709–759. DOI: `10.1080/09500348714550721`.

[Loi+92] G. M. Loiacono, D. N. Loiacono, T. Mcgee, and M. Babb. "Laser damage formation in KTiOPO4 and KTiOAsO4 crystals: Grey tracks". *Journal of Applied Physics* **72** (1992), 2705–2712. DOI: `10.1063/1.351520`.

[Lou00] R. Loudon. *The Quantum Theory of Light.* 3rd ed. Oxford Science Publications, 2000.

[Lu71] E. Y. C. Lu. "New coherent states of the electromagnetic field". *Lettere al Nuovo Cimeto* **2** (1971), 1241–1244. DOI: `10.1007/BF02770161`.

[Lu72] E. Y. C. Lu. "Quantum Correlations in Two-Photon Amplification". *Lettere al Nuovo Cimeto* **3** (1972), 585–589. DOI: `10.1007/BF02762058`.

[LYF00] M. D. Lukin, S. F. Yelin, and M. Fleischhauer. "Entanglement of Atomic Ensembles by Trapping Correlated Photon States". *Phys. Rev. Lett.* **84** (18 2000), 4232–4235. DOI: `10.1103/PhysRevLett.84.4232`.

[Mai60] T. H. Maiman. "Stimulated Optical Radiation in Ruby". *Nature* **187** (1960), 493–494. DOI: `10.1038/187493a0`.

[Mik+09] E. E. Mikhailov, A. Lezama, T. W. Noel, and I. N. and. "Vacuum squeezing via polarization self-rotation and excess noise in hot Rb vapors". *Journal of Modern Optics* **56** (2009), 1985–1992. DOI: `10.1080/09500340903159503`.

[MN08] E. E. Mikhailov and I. Novikova. "Low-frequency vacuum squeezing via polarization self-rotation in Rb vapor". *Opt. Lett.* **33** (2008), 1213–1215. DOI: `10.1364/OL.33.001213`.

[MPK94] H. Mabuchi, E. S. Polzik, and H. J. Kimble. "Blue-light-induced infrared absorption in KNbO3". *Journal of the Optical Society of America B* **11** (1994), 2023. DOI: `10.1364/josab.11.002023`.

[Nak+02] M. Nakamura, S. Takekawa, K. Terabe, K. Kitamura, T. Usami, K. Nakamura, H. Ito, and Y. Furukawa. “Near-Stoichiometric LiTaO 3 for Bulk Quasi-Phase-Matched Devices”. *Ferroelectrics* **273** (2002), 199–204. DOI: `10.1080/00150190211790`.

[Nik05] D. N. Nikogosjan. *Nonlinear Optical Crystals: A Complete Survey.* Springer eBook Collection. Physics and Astronomy. Springer Science+Business Media, Inc, 2005.

[PCK92a] E. S. Polzik, J. Carri, and H. J. Kimble. “Atomic Spectroscopy with Squeezed Light for Sensitivity Beyond the Vacuum-State Limit”. *Applied Physics B* **55** (1992), 279–290.

[PCK92b] E. S. Polzik, J. Carri, and H. J. Kimble. “Spectroscopy with squeezed light”. *Phys. Rev. Lett.* **68** (20 1992), 3020–3023. DOI: `10.1103/PhysRevLett.68.3020`.

[PCK92c] E. S. Polzik, J. Carri, and H. J. Kimble. “Spectroscopy with squeezed light”. *Physical Review Letters* **68** (1992), 3020–3023. DOI: `10.1103/PhysRevLett.68.3020`.

[Roe89] M. G. Roelofs. “Identification of Ti3+ in potassium titanyl phosphate and its possible role in laser damage”. *Journal of Applied Physics* **65** (1989), 4976–4982. DOI: `10.1063/1.343170`.

[Sch17] R. Schnabel. “Squeezed states of light and their applications in laser interferometers”. *Physics Reports* **684** (2017). Squeezed states of light and their applications in laser interferometers, 1–51. DOI: `https://doi.org/10.1016/j.physrep.2017.04.001`.

[Sch19] M. Schröder. “Setup and Characterization of a Bright Light Source at 2128 nm”. MA thesis. Universität Hamburg, 2019.

[Slu+85] R. E. Slusher, L. W. Hollberg, B. Yurke, J. C. Mertz, and J. F. Valley. “Observation of Squeezed States Generated by Four-Wave Mixing in an Optical Cavity”. *Phys. Rev. Lett.* **55** (22 1985), 2409–2412. DOI: `10.1103/PhysRevLett.55.2409`.

[SSS19] R. Schnabel, A. Schönbeck, and S. Steinlechner. *Method and apparatus for frequency conversion and amplification of laser radiation by means of nonlinear media in optical resonators.* Patent EP3781986. 2019.

[Ste+12] J. Steinlechner, L. Jensen, C. Krüger, N. Lastzka, S. Steinlechner, and R. Schnabel. “Photothermal self-phase-modulation technique for absorption measurements on high-reflective coatings”. *Appl. Opt.* **51** (2012), 1156–1161. DOI: `10.1364/AO.51.001156`.

[Ste+13] J. Steinlechner, S. Ast, C. Krüger, A. P. Singh, T. Eberle, V. Händchen, and R. Schnabel. “Absorption measurements of periodically poled potassium titanyl phosphate (PPKTP) at 775 nm and 1550 nm”. *Sensors (Switzerland)* **13** (2013), 565–573. DOI: `10.3390/s130100565`.

[Sto70] D. Stoler. “Equivalence Classes of Minimum Uncertainty Packets”. *Phys. Rev. D* **1** (12 1970), 3217–3219. DOI: `10.1103/PhysRevD.1.3217`.

[Sto71] D. Stoler. “Equivalence Classes of Minimum-Uncertainty Packets. II”. *Phys. Rev. D* **4** (6 1971), 1925–1926. DOI: `10.1103/PhysRevD.4.1925`.

[Tan+06a] T. Tanimura, D. Akamatsu, Y. Yokoi, A. Furusawa, and M. Kozuma. “Generation of a squeezed vacuum resonant on a rubidium D1 line with periodically poled KTiOPO4”. *Optics Letters* **31** (2006), 2344. DOI: `10.1364/ol.31.002344`.

[Tan+06b] T. Tanimura, D. Akamatsu, Y. Yokoi, A. Furusawa, and M. Kozuma. “Generation of a squeezed vacuum resonant on a rubidium D1 line with periodically poled KTiOPO4”. *Optics Letters* **31** (2006), 2344. DOI: `10.1364/ol.31.002344`.

[Tay+13] M. A. Taylor, J. Janousek, V. Daria, J. Knittel, B. Hage, H. A. Bachor, and W. P. Bowen. “Biological measurement beyond the quantum limit”. *Nature Photonics* **7** (2013), 229–233. DOI: `10.1038/nphoton.2012.346`.

[The+11] The LIGO Scientific Collaboration et al. “A gravitational wave observatory operating beyond the quantum shot-noise limit”. English. *Nature physics* **7** (2011), 962–965. DOI: `10.1038/NPHYS2083`.

[Tjö+15] S. Tjörnhammar, V. Maestroni, A. Zukauskas, T. K. Uždavinys, C. Canalias, F. Laurell, and V. Pasiskevicius. “Infrared absorption in KTP isomorphs induced with blue picosecond pulses”. *Optical Materials Express* **5** (2015), 2951. DOI: `10.1364/ome.5.002951`.

[TL] A. Thüring and N. Lastzka. *JamMt: Just another mode matching tool.* available at https://www.sr.bham.ac.uk/dokuwiki/doku.php?id=geosim:jammt.

[Tor+22] A. Torii, K. Shibata, Y. Eto, and T. Hirano. “Improved waveguide-based ultraviolet light generation and pulsed squeezing at 795 nm”. *Optics Express* **30** (2022), 26120. DOI: `10.1364/oe.461507`.

[TR03] F. Torabi-Goudarzi and E. Riis. “Efficient cw high-power frequency doubling in periodically poled KTP”. *Optics Communications* **227** (2003), 389–403. DOI: `https://doi.org/10.1016/j.optcom.2003.09.056`.

[Tri+20] G. Triginer Garces, H. M. Chrzanowski, S. Daryanoosh, V. Thiel, A. L. Marchant, R. B. Patel, P. C. Humphreys, A. Datta, and I. A. Walmsley. “Quantum-enhanced stimulated emission detection for label-free microscopy”. *Applied Physics Letters* **117** (2020), 024002. DOI: `10.1063/5.0009681`.

[Tse+19] M. Tse et al. “Quantum-Enhanced Advanced LIGO Detectors in the Era of Gravitational-Wave Astronomy”. *Phys. Rev. Lett.* **123** (23 2019), 231107. DOI: `10.1103/PhysRevLett.123.231107`.

[Vah+16] H. Vahlbruch, M. Mehmet, K. Danzmann, and R. Schnabel. “Detection of 15 dB Squeezed States of Light and their Application for the Absolute Calibration of Photoelectric Quantum Efficiency”. *Phys. Rev. Lett.* **117** (11 2016), 110801. DOI: `10.1103/PhysRevLett.117.110801`.

[VBZ88] H. Vanherzeele, J. D. Bierlein, and F. C. Zumsteg. “Index of refraction measurements and parametric generation in hydrothermally grown KTiOPO4”. *Appl. Opt.* **27** (1988), 3314–3316. DOI: `10.1364/AO.27.003314`.

[Wan+17] Y. Wang, W. Yang, Z. Li, and Y. Zheng. “Determination of blue-light-induced infrared absorption based on mode-matching efficiency in an optical parametric oscillator”. *Scientific Reports* **7** (2017), 1–7. DOI: `10.1038/srep41405`.

[Wen+17] X. Wen, Y. Han, J. Liu, J. He, and J. Wang. “Polarization squeezing at the audio frequency band for the Rubidium D_1 line”. *Optics Express* **25** (2017), 20737. DOI: `10.1364/oe.25.020737`.

[WM08] D. Walls and G. J. Milburn. *Quantum Optics*. 2nd ed. Springer Berlin Heidelberg, 2008. DOI: `10.15713/ins.mmj.3`.

[Wol+10] F. Wolfgramm, A. Cerè, F. A. Beduini, A. Predojević, M. Koschorreck, and M. W. Mitchell. “Squeezed-light optical magnetometry”. *Physical Review Letters* **105** (2010), 1–4. DOI: `10.1103/PhysRevLett.105.053601`.

[WPL04] S. Wang, V. Pasiskevicius, and F. Laurell. “Dynamics of green light-induced infrared absorption in KTiOPO4 and periodically poled KTiOPO4”. *Journal of Applied Physics* **96** (2004), 2023–2028. DOI: `10.1063/1.1738528`.

[Wu+86] L.-A. Wu, H. J. Kimble, J. L. Hall, and H. Wu. “Generation of Squeezed States by Parametric Down Conversion”. *Phys. Rev. Lett.* **57** (20 1986), 2520–2523. DOI: `10.1103/PhysRevLett.57.2520`.

[Xu+22a] Z. Xu, K. Oguchi, Y. Taguchi, Y. Sano, Y. Miyawaki, D. Cheon, K. Katoh, and Y. Ozeki. “Stimulated Raman scattering spectroscopy with quantum-enhanced balanced detection”. *Opt. Express* **30** (2022), 18589–18598. DOI: `10.1364/OE.456653`.

[Xu+22b] Z. Xu, K. Oguchi, Y. Taguchi, S. Takahashi, Y. Sano, T. Mizuguchi, K. Katoh, and Y. Ozeki. “Quantum-enhanced stimulated Raman scattering microscopy in a high-power regime”. *Opt. Lett.* **47** (2022), 5829–5832. DOI: `10.1364/OL.473130`.

[Yan+15] W. Yang, Y. Wang, Y. Zheng, and H. Lu. “Comparative study of the frequency-doubling performance on ring and linear cavity at short wavelength region”. *Optics Express* **23** (2015), 19624. DOI: `10.1364/oe.23.019624`.

[Yue76] H. P. Yuen. “Two-photon coherent states of the radiation field”. *Phys. Rev. A* **13** (6 1976), 2226–2243. DOI: `10.1103/PhysRevA.13.2226`.

[Zha+11] Q. Zhang, G. Feng, J. Han, B. Li, Q. Zhu, and X. Xie. "High repetition rate laser pulse induced damage in KTP crystal: Gray-tracking and catastrophic damage". *Optik* **122** (2011), 1313–1318. DOI: `10.1016/j.ijleo.2010.06.051`.

[Zie+17] J. A. Zielińska, A. Zukauskas, C. Canalias, M. A. Noyan, and M. W. Mitchell. "Fully-resonant, tunable, monolithic frequency conversion as a coherent UVA source". *Opt. Express* **25** (2017), 1142–1150. DOI: `10.1364/OE.25.001142`.

[ZM17] J. A. Zielińska and M. W. Mitchell. "Self-tuning optical resonator". *Opt. Lett.* **42** (2017), 5298–5301. DOI: `10.1364/OL.42.005298`.

[ZM18] J. A. Zielińska and M. W. Mitchell. "Atom-resonant squeezed light from a tunable monolithic ppRKTP parametric amplifier". *Opt. Lett.* **43** (2018), 643–646. DOI: `10.1364/OL.43.000643`.

[Zuo+22] G. Zuo, Y. Zhang, J. Li, S. Zhu, Y. Guo, and T. Zhang. "Determination of weakly squeezed vacuum states through photon statistics measurement". *Physics Letters, Section A: General, Atomic and Solid State Physics* **439** (2022). DOI: `10.1016/j.physleta.2022.128133`.

Eidesstattliche Versicherung

Hiermit versichere ich an Eides statt, die vorliegende Dissertationsschrift selbst verfasst und keine anderen als die angegebenen Hilfsmittel und Quellen benutzt zu haben. Sofern im Zuge der Erstellung der vorliegenden Dissertationsschrift generative Künstliche Intelligenz (gKI) basierte elektronische Hilfsmittel verwendet wurden, versichere ich, dass meine eigene Leistung im Vordergrund stand und dass eine vollständige Dokumentation aller verwendeten Hilfsmittel gemäß der Guten wissenschaftlichen Praxis vorliegt. Ich trage die Verantwortung für eventuell durch die gKI generierte fehlerhafte oder verzerrte Inhalte, fehlerhafte Referenzen, Verstöße gegen das Datenschutz- und Urheberrecht oder Plagiate.

Hamburg, den 11. September 2025

Danksagung

Mein Dank gilt all denjenigen, die mit Rat, Tat und anderen Formen von Unterstützung dazu beigetragen haben, dass ich das Projekt Doktorarbeit erfolgreich abschließen konnte. Zunächst einmal danke ich den Mitgliedern meiner Prüfungskommission: Prof. Dr. Roman Schnabel für die Möglichkeit, die Experimente in seiner Arbeitsgruppe durchzuführen und für das Gutachten zur Arbeit; Dr. Mikhail Korobko für das spontane Einspringen für das zweite Gutachten und für das Teilen seines scheinbar unerschöpflichen Wissensschatzes in den Jahren davor; Prof. Dr. Daniela Pfannkuche sowohl für den Prüfungsvorsitz als auch für ihre Unterstützung und Beratung; Prof. Dr. Arwen Pearson, Dr. Christoph Becker und dem sehr spontan eingesprungenen Prof. Dr. Peter Schauss für ihre Bereitschaft, in der Prüfungskommission mitzuwirken.

Einen besonders wichtigen Beitrag zu dieser Arbeit haben meine Freunde, Labor- und Bürokollegen geleistet: Mit ihren Hands-on-Erfahrungen und Ideen waren sie mir wertvolle Sparringpartner, um voneinander zu lernen, gemeinsam Lösungen für experimentelle Probleme zu finden und das untersuchte System besser zu verstehen. Besonders danken möchte ich dafür an dieser Stelle meinem „Postdoc“ Julian Gurs (der sich vor allem in den ersten Jahren sehr mit ins Experiment hineingedacht hat), Dr. Max Hachmann (mit seiner Expertise zum Lasersystem sowie zur digitalen Temperatursteuerung und automatischen Datenaufnahme) und Dr. Christian Darsow-Fromm (mein Service-Desk für IT, Datenauswertung und Interpretation der Ergebnisse), der überdies diese Arbeit korrekturgelesen hat. Bei letzteren beiden freut mich besonders, dass diese Unterstützung allein auf freundschaftlicher Basis und über Arbeitsgruppengrenzen hinweg geschah.

Sophie Verclas, Dr. Malte Hagemann und Dr. Benedict Tohermes danke ich für spannende Diskussionen und die angenehme Atmosphäre im Büro. Dr. Jan Südbeck und Dr. Axel Schönbeck danke ich dafür, dass ich auf die elektronischen und konstruktiven Vorarbeiten für das monolithische Design zurückgreifen durfte.

Zum Schluss möchte ich noch meinen Freunden, Weggefährten und meiner Familie ganz herzlich auch für alle nicht-fachliche Unterstützung danken und mich dafür entschuldigen, wie viel Raum die Doktorarbeit in den vergangenen Jahren eingenommen hat. Vielen Dank für eure immer offenen Ohren, euer Verständnis, eure Unterstützung, und natürlich auch fürs Mitfiebern und Mitfeiern!